



MICROMETEOROLOGY GROUP
University of Bayreuth

Novel insights into the dynamics of cold-air drainage and pooling on a gentle slope from fiber-optic distributed temperature sensing

Master Thesis in Geoecology

Lena Pfister



supervised by

Prof. Dr. Christoph THOMAS

February 2, 2016



MICROMETEOROLOGY GROUP
University of Bayreuth

Novel insights into the dynamics of cold-air drainage and pooling on a gentle slope from fiber-optic distributed temperature sensing

Master Thesis in Geoecology

Lena Pfister



supervised by

Prof. Dr. Christoph THOMAS

February 2, 2016

Details Author:

Lena Pfister (B.Sc. Geoecology, University of Bayreuth)

matriculation number: 1195930

E-Mail: lena.pfister@gmx.de

Auditors

Prof. Dr. Christoph Thomas (Micrometeorology Group, University of Bayreuth)

Prof. Dr. Chad Higgins (Biological and Ecological Engineering, Oregon State University)

Cover picture:

Visualization of blockage of cold-air flow over a lake by releasing machine-generated fog in combination with a laser. Photo taken on 20th of April at 10:20 PM. (Photograph: Prof. Dr. Christoph Thomas)

Abstract

Urban climate can benefit from cold-air drainage as it may help alleviate the urban heat island. In contrast, stable cold-air pools can damage plants especially in rural areas. In this study, we examined the dynamics of cold-air drainage and pooling in a peri-urban setting over a period of 47 days along a 170 m long slope with an inclination of 1.3° located in the Ecological Botany Gardens of the University of Bayreuth. Air and soil temperatures were measured using distributed temperature sensing of an 2-dimensional fiber-optic array at six heights (-2 cm to 100 cm) along the slope sampling every 1 min and every 1 m. Ancillary measurements of winds, turbulence intensity and momentum exchange were collected using two ultrasonic anemometers installed at 0.1 m and 17 m height at the center of the transect. We hypothesized that cold-air drainage, here defined as a gravity-driven density flow near the bottom originating from local radiative cooling of the surface, is decoupled from non-local flows and can thus be predicted from the local topography.

The nocturnal data were stratified by classes of longwave radiation balance, wind speed, and wind direction at 0.1 m agl. The four most abundant classes were tested further for decoupling of wind velocities and directions between 17 and 0.1 m. We further computed the vertical and horizontal temperature perturbations of the fiber-optic array as evaluation for these cases, as well as subject the temperature data to a multiresolution decomposition to investigate the spatial two-point correlation coefficient along the transect. Finally, the cold pool intensity was calculated.

The results revealed none of the four most abundant classes followed classical textbook knowledge of locally produced cold-air drainage. Instead, we found that the near-surface flow was strongly forced by two possibly competing non-local flow modes. The first mode caused weak ($< 0.4 \text{ ms}^{-1}$) near-surface winds directed perpendicular to the local slope and showed strong vertical decoupling of wind velocities and directions. The vertical and horizontal perturbation of the temperature as well as the cold-pool intensity was high and the two-point correlation coefficient decorrelated fast with increasing distance. In contrast, for the second mode the wind was aligned with the local slope and the wind velocities and directions agreed vertically. However, momentum exchange was much enhanced leading to intense shear-generated mixing and almost vanishing temperature perturbations, higher spatial coherence indicated by a slower spatial decorrelations, and a cold-pool intensity of close to zero. In conclusion, the first mode was interpreted as a relatively weak non-local valley-scale cold-air drainage modulating the close to stationary cold-air pool filling the shallow depression the Botanical Gardens are located in. Here, the deeper cold-air drainage causes only weak local movements at the surface as both layers are largely decoupled. The second mode is possibly caused by a recirculation of a stronger valley-scale flow with sufficient synoptic forcing. Our

findings challenge the common practice to predict cold-air dynamics solely based on micro-topographic analysis.

Zusammenfassung

Städtische Klimate können von Kaltluftabflüssen profitieren, da diese städtische Hitzeinseln abschwächen können. Hingegen können stabile Kaltluftseen besonders in ländlichen Gegenden Pflanzen beschädigen. In dieser Studie werden die Dynamiken des Kaltluftabflusses sowie Kaltluftseebildung über einem 170 m langen Hang mit 1.3° Steigung, gelegen im Ökologisch Botanischen Garten der Universität Bayreuth, für eine Messperiode von 47 Tagen untersucht. Luft- und Bodentemperaturen wurden mittels Distributed Temperature Sensing einer 2-dimensionalen Glasfaserharfe in sechs Höhen (-2 cm bis 100 cm) gemessen. Die räumliche und zeitliche Auflösung betrug 1m und 1 min. Gleichzeitig wurden Wind-, Turbulenzintensitäts- und Impulsaustauschmessungen durchgeführt. Hierfür wurden zwei Ultraschallanemometer in 0.1 m und 17 m Höhe in der Mitte des Transektes installiert. Kaltluftabfluss ist hier definiert als gravitationsbedingter, bodennaher Dichtefluss, der durch die lokale Abkühlung der Oberfläche aufgrund langwelliger Ausstrahlung entsteht. Wir stellten somit die Hypothese auf, dass Kaltluftabfluss von nicht-lokalen Flüssen entkoppelt ist und somit durch die lokale Topographie bestimmt werden kann.

Die nächtlichen Daten wurden in Klassen eingeteilt aufgrund langwelliger Ausstrahlungsbilanz, Windgeschwindigkeit und -richtung in 0.1 m Höhe über Grund. Die vier häufigsten Klassen wurden auf Entkopplung der Windgeschwindigkeiten und -richtungen zwischen 17 und 0.1 m getestet. Desweiteren wurden zur Auswertung dieser Klassen die vertikale und horizontale Temperaturperturbation der Glasfaserharfe berechnet, sowie die Temperaturdaten einer Multiskalendekomposition unterzogen, um den räumlichen Zweipunktkorrelationskoeffizienten entlang des Transektes zu untersuchen. Zudem wurde die Kaltluftseeintensität bestimmt.

Die Ergebnisse zeigten, dass keine der vier häufigsten Nachtklassen dem klassischen Lehrbuchwissen des lokal entstehenden Kaltluftabflusses folgten. Im Gegenteil, wir fanden heraus, dass der bodennahe Fluss stark von zwei konkurrierenden nicht-lokalen Flussmodi angetrieben wurde. Der erste Modus verursachte schwache ($< 0.4 \text{ ms}^{-1}$) oberflächennahe Winde, die senkrecht zum Hang gerichtet waren, und wies starke vertikale Entkopplung der Windgeschwindigkeiten und -richtungen auf. Die vertikale und horizontale Temperaturperturbation als auch die Kaltluftseeintensität wiesen hohe Werte auf und der Zweipunktkorrelationskoeffizient dekorrelierte schnell mit zunehmendem Abstand. Der zweite Modus hingegen wies Winde entlang des lokalen Hanges auf und die Windgeschwindigkeiten und -richtungen hatten einen vertikalen Zusammenhang. Jedoch war der Impulsaustausch erhöht und führte dadurch zu intensiven Verwirbelungen und fast verschwindenden Temperaturperturbationen. Desweiteren deutete die räumlich langsamere Dekorrelation auf höhere räumliche Kohärenz hin und es konnte kein Kaltluftsee nachgewiesen werden. Als Schlussfolgerung wird der erste Modus als relativ schwacher nicht-lokaler Kaltluftabfluss auf Tal-Skala interpretiert, der den

stationären Kaltluftsee innerhalb der flachen Senke des Botanischen Gartens modulierte. Dort verursachte ein tiefer gelegener Kaltluftabfluss geringfügige lokale Bewegungen nahe der Oberfläche, denn beide Schichten waren deutlich entkoppelt. Der zweite Modus war wahrscheinlich durch eine Rezirkulation eines stärkeren Talwindes mit ausreichenden synoptischen Antrieben entstanden. Unsere Ergebnisse stellen die herkömmliche Praxis der Vorhersage der Kaltluftdynamik allein basierend auf Analyse der Mikro-Topographie in Frage.

Contents

Abstract	I
Zusammenfassung	III
1 Introduction	1
2 Deployment and data acquisition	5
2.1 Site description	5
2.2 Distributed Temperature Sensing	5
2.3 Deployment of CADEX	8
2.3.1 Transect setup	8
2.3.2 Columns setup	8
2.4 Flow and Flux measurements	9
2.5 Quality control	11
2.5.1 Methods for flow and flux measurements	12
2.5.2 Summary of flagged data from flow and flux measurements	13
2.5.3 Methods for DTS-measurements	13
2.5.4 Summary of flagged data from DTS-measurements	14
3 Analysis of CADEX	15
3.1 Validation of DTS-measurements	15
3.2 Classification in Night-Classes	15
3.2.1 Investigation of vertical decoupling	17
3.2.2 Spatial temperature distribution	19
3.3 Case Studies	22
3.3.1 Multiresolution decomposition (MRD)	22
4 Results	25
4.1 Validation of DTS-measurements	25
4.2 Investigation of vertical decoupling	26
4.2.1 Vertical correlation of wind velocities and directions	26
4.2.2 Correlation between wind velocities and momentum exchange	28
4.2.3 Prevailing wind directions in 17 m	29
4.3 Spatial temperature distribution	30
4.3.1 Horizontal and vertical perturbation of temperature	30
4.3.2 Determination of cold-air pools	33
4.3.3 Terrain classification for frost risk	33
4.4 Case studies	34
4.4.1 Physical description	34
4.4.2 MRD: Spatial coherence of temperature development	35
4.4.3 Fog Experiment	41
5 Discussion	45
5.1 Validation of DTS-measurements	45

5.2	Investigation of vertical decoupling	46
5.2.1	Vertical correlation of wind velocities and directions	46
5.2.2	Correlation between wind velocities and momentum exchange	48
5.2.3	Prevailing wind directions in 17 m	49
5.3	Spatial temperature distribution	50
5.3.1	Horizontal and vertical perturbation of temperature	50
5.3.2	Determination of cold-air pools	53
5.3.3	Terrain classification for frost risk	53
5.4	Case studies	54
5.4.1	Physical description	54
5.4.2	MRD: Spatial coherence of temperature development	56
5.4.3	Fog Experiment	57
5.5	Summary	58
6	Conclusion	61
	Acknowledgements	63
	Bibliography	63
A	Additional Tables	69
B	Additional Figures	77
C	Digital Medium	85
	Declaration of Authorship	87

List of Figures

2.1	Draft of field site with all measurement devices and the different domains . . .	6
2.2	Diagram of Rayleigh, Raman, and Brillouin return scattering intensity after Selker et al. (2006)	7
2.3	Draft of the setup of CADEX	9
2.4	Columns in the field	10
2.5	Installation of Station B	10
2.6	Detailed view of upside-down installation of Station B	11
2.7	Installation of Station D	12
3.1	Draft cold-air formation, drainage and pooling on the local slope during cloudless, calm nights	15
3.2	Temporal distribution of the four night-classes	17
3.3	Draft of vertical relations between Station EBG (17 m) and Station B (0.1 m)	18
3.4	Two idealized limits of cold-air pools according to Mahrt (personal communication)	21
4.1	Temperature measurements in 5 cm height with two different devices	25
4.2	Standard deviation of the glass fiber temperature (σ_{Tf}), of wind velocity in 0.1 m height ($\sigma_{u_{0.1m}}$) and of the wind direction change in 0.1 m height ($\sigma_{\Delta\varphi_{0.1m}}$) within an averaging period of 10 minutes	26
4.3	Correlation between vertical wind direction shear in 17 m and 0.1 m (φ_{shear}) and wind velocity in 0.1 m ($u_{0.1 m}$) for all four night-classes	27
4.4	Coplot of Night-Class ENE 1	28
4.5	Correlation between wind velocities in 0.1 m and 17 m ($u_{0.1 m}$ and $u_{17 m}$) and between wind and friction velocity in 0.1 m ($u_{0.1 m}^*$) for all four night-classes	29
4.6	Wind direction and velocity in 17 m height ($\varphi_{17 m}$ and $u_{17 m}$) for each Night-Class with wind direction ENE in 0.1 m height	30
4.7	Mean horizontal perturbation of temperature	31
4.8	Mean vertical perturbation of temperature	32
4.9	Terrain classification for frost risk	34
4.10	Physical description of Case Study 1 by fiber temperature in 20 cm along the slope (Tf), wind velocities ($u_{17 m}$ and $u_{0.1 m}$) and directions ($\varphi_{17 m}$ and $\varphi_{0.1 m}$)	36
4.11	Physical description of Case Study 2 by fiber temperature in 20 cm along the slope (Tf), wind velocities ($u_{17 m}$ and $u_{0.1 m}$) and directions ($\varphi_{17 m}$ and $\varphi_{0.1 m}$)	37
4.12	Physical description of Case Study 3 by fiber temperature in 20 cm along the slope (Tf), wind velocities ($u_{17 m}$ and $u_{0.1 m}$) and directions ($\varphi_{17 m}$ and $\varphi_{0.1 m}$)	38
4.13	Physical description of Case Study 4 by fiber temperature in 20 cm along the slope (Tf), wind velocities ($u_{17 m}$ and $u_{0.1 m}$) and directions ($\varphi_{17 m}$ and $\varphi_{0.1 m}$)	39
4.14	MRD: Spatial coherence of temperature development in 5 cm along the transect.	40
4.15	Fog Experiment: Direction shear	41
4.16	Fog Experiment: Upslope flow	42
4.17	Fog Experiment: Blockage of cold-air flow above the lake	42

5.1	Summary of wind velocities and directions for both valley-scale flow modes and regional topographic overview	60
B.1	Proportions of the columns	77
B.2	Composition of the glass fiber	77
B.3	Wind rose of the ultrasonic at the transect in 0.1 m height	78
B.4	Coplot of Night-Class W	78
B.5	Coplot of Night-Class ENE 2	79
B.6	Correlation between wind velocities in 17 m and 0.1 m height ($u_{17\ m}$ and $u_{0.1\ m}$) for Night-Class ENE 3	79
B.7	Prevailing wind direction in 17 m for all night-classes with wind direction W .	80
B.8	Draft cold-air formation and drainage on the local slope during cloudless windy nights	80
B.9	Self-designed plow for inserting the fiber into the ground	80
B.10	Self-designed blocks	81
B.11	Self-designed poles	81
B.12	Pulleys and pulley-holder	82
B.13	Calibration baths	82
B.14	Construction of the columns	83
B.15	Aerial image of the field site	83

List of Tables

2.1	Quantity of hard flagged data	13
A.1	Transfer matrix of CADEX	69
A.2	Quantity of categories	70
A.3	Output BmmFlux-software	70
A.4	Quantity of spikes	72
A.5	Quantity of dropouts	74

List of Abbreviations and Symbols

CADEX	Cold-air drainage and pooling experiment	
DTS	Distributed Temperature Sensing	
EBG	Ecological Botanical Gardens	
MRD	Multiresolution decomposition	
SMA	Simple moving average	
CPI	Cold-air pool intensity	[K]
DNT	Day and night indicator calculated from zenith angles	[-]
I_{net}	longwave radiation balance	[Wm ⁻²]
N	Number of measurements	[-]
L_{\uparrow}	upwelling longwave radiation	[Wm ⁻²]
L_{\downarrow}	downwelling longwave radiation	[Wm ⁻²]
$P_{frost\ risk}$	Frost risk percentage	[-]
R_{ij}	Spatial two-point correlation coefficient	[-]
T_f	Temperature of the glass fiber	[°C]
$u_{0.1\ m}$	Wind velocity in 0.1 m	[ms ⁻¹]
$u_{17\ m}$	Wind velocity in 17 m	[ms ⁻¹]
$u^*_{0.1\ m}$	friction velocity in 0.1 m	[ms ⁻¹]
$\varphi_{0.1\ m}$	Wind direction in 0.1 m	[°]
$\varphi_{17\ m}$	Wind direction in 17 m	[°]
φ_{shear}	Wind direction shear between 0.1 m and 17 m	[°]
σ_{Tf}	Standard deviation of T_f	[K]
$\sigma_{u_{0.1\ m}}$	Standard deviation of $u_{0.1\ m}$	[ms ⁻¹]
$\sigma_{\Delta\varphi_{0.1\ m}}$	Standard deviation of $\varphi_{0.1\ m}$	[°]
τ_R	Kendall's rank correlation coefficient	[-]
θ^*	Perturbation of temperature	[K]
θ^*_{horiz}	Horizontal temperature perturbation	[K]
θ^*_{verti}	Horizontal temperature perturbation	[K]
θ^*_{top}	Horizontal temperature perturbation on top of the slope	[K]
$\mu_{\theta^*_{horiz}}$	Mean horizontal temperature perturbation	[K]
$\mu_{\theta^*_{verti}}$	Mean vertical temperature perturbation	[K]
Γ_d	Dry adiabatic temperature gradient	[Kkm ⁻¹]

1. Introduction

Open hilltops, forested slopes and other inclined surfaces are source areas for the formation and drainage of cold-air (Foken, 2008). Additionally, radiative cooling and light ambient winds are the key factors for the formation of cold-air (e.g. Barr and Orgill 1989, Soler et al. 2002, Foken 2008, Rakovec et al. 2015, Geiss and Mahrt 2015). Radiative cooling is most effective in nights with clear skies. Geiger et al. (1995) evaluated and Foken et al. (1999) confirmed, that during cloudy nights the temperature gradient in the lowest 2 m is only 0.3 Km^{-1} , whereas a temperature gradient of 1.5 Km^{-1} is expected for clear skies. The resulting cold-air drainage on a slope or within a valley is highly related to topography (e.g. Haiden and Whiteman 2005, Mahrt et al. 2013). Further, Barr and Orgill (1989) reported distinct smaller cold-air drainage depths within a valley for cloudy nights, as clouds alleviate radiative cooling. Besides, cold-air drainage and pooling are interrupted or eliminated by shear induced turbulent entrainment of weak to strong ambient winds originating from a higher scale (e.g. Gustavsson et al. 1998, Mahrt et al. 2001, Soler et al. 2002, Zhong et al. 2003, Sun et al. 2007, Rakovec et al. 2015, Geiss and Mahrt 2015). The terrain forced flow of cold-air is especially important in mountainous regions, where the drainage of cold-air can highly accelerate down a slope. In valley locations this drainage build up a cold-air pool during night, which sometimes can not be retrenched during day and is vertically decoupled from the upper atmosphere (Whiteman, 2000). This accumulation of cold air, i.e. cold-air pooling, in depressions or valleys may lead to frost and harm the present vegetation. The severity of frost damage to a seedling can be very high, depending on species, and thus the possibility of frost damage has an impact on biodiversity (Blennow and Lindkvist, 2000). Cold-air pooling is also a huge hazard for crop failure in rural agricultural systems (e.g. Anstey et al. 1959). Against this hazard, frost warning systems are established for mountainous areas (Chung et al., 2006). Beside these physical and biological aspects, the drainage of cold-air has strong effects on urban climate alleviating the urban heat island (e.g. Kuttler et al. 1996). The magnitude of urban heat islands can be reduced by about 40 % (Nkemdirim, 1980). Moreover, Gross (1987) concluded from simulations, that forested slopes are more effective in ventilating a city than slopes covered with short vegetation. But cold-air drainage and especially pooling may also have negative aspects in rather gentle terrain. A cold-air pool in a depression or valley can lower the temperatures under the dew point resulting in fog formation, which can cause traffic hazards, or can trap contaminants and other gases causing health hazards (e.g. Foken 2008, Silcox et al. 2012). Besides, Mahrt et al. (2001) found large imbalances in nocturnal surface energy and carbon dioxide budgets of eddy correlation measurements. They proposed, that cold-air drainage may explain this, because eddy correlation measurements at standard levels (3-10 m) do not capture this flux. This was verified by Goulden et al. (2006) by measuring CO_2 -densities at 12 heights with 5 measurements in the lowest 3 m. They concluded, that the CO_2 -loss computed by eddy covariance was caused by horizontal outflow of CO_2 within cold-air drainage and not

by CO₂-uptake of the vegetation, what was also verified by Sun et al. (2007). Therefore, criteria associated with vertical temperature gradients may prove better than above-canopy friction velocities for screening nocturnal eddy covariance observations to eliminate periods that underestimate CO₂ flux. Accordingly, cold-air drainage and pooling are processes of interest in different application areas.

Besides, the analysis of cold-air drainage and pooling on different spatial scales, pioneered the way to numerical prediction models. For example, a three-dimensional fog forecasting in complex terrain could be developed (Müller et al., 2010). Further, the studies of Liu and Bromwich 1997 and Burns and Chemel 2015 tested two numerical prediction models for katabatic flows and cold-air pooling, respectively. The results showed, that the numerical simulations were not completely in conformity with observations. In both cases, the assimilation of those models to the local topography was not adequate. Mahrt et al. (2013) emphasized, that site characteristics have a much larger role with increasing stability, because even nearby topography can induce propagating modes and turbulence. Therefore, especially numerical weather prediction models are further increased in spatial resolution and the assimilation of surface data becomes more widespread (Bodine et al., 2009). Nevertheless, Rakovec et al. (2015) revealed, that the predictions of this models are not applicable for calm nights with clear skies. Accordingly, strategies have to be found to improve the assimilation of those.

A new tool with a higher temporal and spatial resolution than commonly used point measurements is the Distributed Temperature Sensing (DTS). DTS provides a broad application field in combination with a high temporal and spatial resolution of temperature (Selker et al., 2006). Precise temperature measurements (0.01 °C) with a glass fiber below and above water surfaces as well as within the ground or snow is possible. The highest resolutions are a fraction of 1 min and 1 m, depending on used measurement device. However, for a spatial vertical higher resolution, the glass fiber can be wound around a cylinder. Therefore, measurements on a spatial scale of 0.003 to 30 000 m can be achieved. Keller et al. (2011) approved the DTS-technique suitable for atmospheric temperature profile measurements. Further, Zeeman et al. (2015) revealed, that nocturnal transient temperature structures under weak wind conditions can be better observed by DTS than by the traditional point observations. As approved by another study of Thomas et al. (2012), the fiber-optic DTS-technique of this study was adequate to resolve individual sub-metre sized turbulent and non-turbulent structures within seconds. These measurements can also be used for eddy-covariance computation of sensible heat flux with adequate results. Further, transient cold-air pool dynamics can be evaluated with this technique. Therefore, we chose the DTS-technique for investigations in cold-air drainage and pooling in our experiment.

The majority of experimental sites found in the literature are located in complex terrain (e.g. Clements et al. 2003, Banta et al. 2004, Darby et al. 2006, Silcox et al. 2012, Lareau et al. 2013). However, much of the Earth's surface is characterized by gentle, less organized terrain (Meybeck et al., 2001). Further, even small variations from a planar slope of a valley can significantly alter the drainage flow (Haiden and Whiteman, 2005). Therefore, a gentle terrain was chosen as experimental site. The transect was 170 m long and located in the Ecological Botanical Gardens (EBG) of the University of Bayreuth. The site consisted of

a slope with an inclination of 1.3° and an adjacent shallow lake in the depression in this peri-urban setting. The lake was from North to South 100 m long and ≈ 31 m wide. In 1999 Foken et al. (1999) have already measured nocturnal minimum temperatures at four different locations on the same slope with a temporal resolution of 15 min. The results showed a horizontal temperature gradient with the highest temperatures on top of the hill and the lowest at the bottom of the slope. They concluded, that the cold-air drainage prevented the top of the slope from cooling, as this outflow of cold air was compensated by warmer air from above. However, this horizontal advection of cold air enhanced the temperature decrease at the bottom of the slope by cold-air pooling. We wanted to verify these cold-air dynamics with the DTS-technique providing temperature measurement with a very high spatial and temporal resolution of 1 min and 1 m. Therefore, a 2-dimensional fiber-optic array at six heights (-2 cm to 100 cm) was installed along this slope and above the lake. Ancillary, measurements of winds, turbulence intensity and momentum exchange were collected using two ultrasonic anemometers installed at 0.1 m and 17 m height at the center of the transect. The measurements were carried out from 13th of March until 29th of April. The dataset was classified into night-classes by three factors: The longwave radiation balance, the wind velocity and direction near the ground. The longwave radiation balance revealed the conditions for cold-air formation, whereas the other two factor showed the near bottom flow direction and strength. The resulting night-classes from this inductive analysis were tested for vertical decoupling by investigations of the correlation of wind velocities and directions. Besides, the horizontal and vertical temperature perturbation as well as the cold-air pool intensity (CPI) were compared between the night-classes. For an ecological assessment, the slope was classified by frost risk. Furthermore, for case studies a multiresolution decomposition of the temperature signal (MRD) was implemented on different time scales. Finally, the spatial two-point correlation coefficient was computed for these time scales.

In literature cold-air drainage is defined as a near-bottom flow, which originates from the local formation of cold air and is decoupled from non-local flows above (e.g. Mahrt et al. 2001, Soler et al. 2002). Apart from that, topography plays an important role even in gentle terrain (e.g. Haiden and Whiteman 2005, Mahrt et al. 2013). Moreover, it is well known, that water bodies influence the microclimate of ambient areas (Minder et al., 2015) by enhancing the ambient air temperature due to a higher surface heat flux above the lake (Schertzer et al., 2003). DTS measurements can provide new insights into cold-air drainage and pooling, as commonly only point measurements are evaluated. Therefore we want to test the following hypotheses:

- (i) Cold-air drainage and pooling can be predicted by the local topography.
- (ii) The experimental setup and inductive analysis are sufficient to identify a night-class of cold-air drainage and pooling.
- (iii) The shallow lake can not inhibit cold-air drainage and pooling, as the cold-air flow rate exceeds the effects of conduction and convection.

2. Deployment and data acquisition

2.1 Site description

The study site was located in the Ecological Botanical Gardens (EBG) of the university of Bayreuth (Fig. 2.1). The transect was set up from the top of a hill (Point A) to the other side of a lake (Point D). It was 170 m long with a height difference of 4.3 m resulting in an inclination of about 1.3°. Basis for the domains of the transect were the different ground covers along the transect as suggested by Mahrt et al. (2009). Starting at Point A, the first 41 m were mainly covered by solitary standing trees or shrubs (Open Stand). This domain also included a small stream (width ≈ 0.60 m) in a distance of 3.2 m to Point A. The ground cover of the next 103 m of the transect were an open meadow and were sectioned into Upper (72 m) and Lower Meadow (31 m). The Lower Meadow merged into the lake, which was 26 m wide (Lake).

The temperature measurements along the transect were investigated by distributed temperature sensing (DTS) and conducted with an 2-dimensional fiber-optic array with six heights (-2 cm to 100 cm) as well as two additional columns with a higher spatial resolution at Point B and D. One coherent glass fiber was used for installation of this measurement array. At Point B a tower for meteorologic long-term measurements (Station EBG) was installed for measurements of radiation, humidity, air and soil temperatures, wind velocity and direction. Additionally, two 3-D ultrasonic anemometer were installed. The first was mounted upside-down in 0.10 m height near Point B. An open-path hygrometer was installed together with the second 3-D ultrasonic anemometer 2 m above the lake at Point D. The cold-air drainage and pooling experiment (CADEX) started on the 13th of March 2015 at 01:20 PM and lasted until the 29th of April 2015 at 10:15 AM.

2.2 Distributed Temperature Sensing

Air temperatures were measured using a Oryx (Model Oryx DTS RS232 x2, Sensornet, Hertfordshire, UK) for distributed temperature sensing. Two channels were used in single-ended mode. A 50/125 Multimode glass fiber (FBR00259 DRAKA 50/125 BIF OM2, AFL, Mönchengladbach, Germany) was chosen due to its low transmissibility and low attenuation after splicing. The glass fiber cable consisted of a white outer sleeve ($\varnothing 900 \mu\text{m}$) for protection against heating by shortwave radiation (Fig. B.2). Below, a textile fiber was situated against tearing as well as a cladding ($\varnothing 125 \mu\text{m}$) around the light transmitting glass fiber core ($\varnothing 50 \mu\text{m}$). The refraction index of the cladding and the glass fiber core was different, thus reflection of electromagnetic waves was effective. A laser pulse (wavelength: 975 nm; laser pulse length: 1 m) was sent bidirectional through the fiber-optic array. Thereby, each end of the fiber-optic array was connected to one channel. The temporal offset between both

channels was 30 s. Consequently, the measurement of Channel 1 is the reversed measurement of Channel 2. The reflected signal of the laser pulse was referenced to the intensity of light-bands caused by the inelastic Raman scattering (Fig. 2.2). The Anti-Stokes within the Raman spectrum shifted their intensity with temperature, while Stokes remained unaltered. Therefore the ratio of the magnitude of Stokes to Anti-Stokes was exponentially dependent on the ambient temperature:

$$T \propto \ln \left(\frac{I_{\text{Anti-Stokes}}}{I_{\text{Stokes}}} \right) \quad (2.1)$$

The returned signal intensity was integrated over 30 s for each direction. Thus the integrated measurements were a relative temperature signal for each 1-m-segment of the glass fiber. The DTS-unit stored these temperature measurements dependent on the distance from the laser pulse source as length along the fiber in meter (LAF).

The 1-dimensional temperature signal dependent on the LAF was transformed into a 2-dimensional coordinate system of the transect and the columns. Therefore, the temperature signal was mapped by cooling each start and end of a height in the transect or a column. Ice cooling units were used to create a temperature outlier in the measured temperature signal. Each position was noted as LAF for Channel 1 (Tab. A.1). This transfer-matrix was used in the post-processing to transform the temperature signal into a 2-dimensional coordinate system dependent on distance from Point A and the height above ground. The different heights of the columns were located by the proportion of the column and number of windings around it as well as the distance between windings.

The calibration of the relative temperature signal to absolute temperature was performed with two calibration baths, containing a platinum resistance thermometer (Pt100). One calibration bath was heated to a constant temperature of 20 °C, while the other was cooled down to ± 0 °C (Fig. B.13). The calibration was conducted continuously during the measurements.

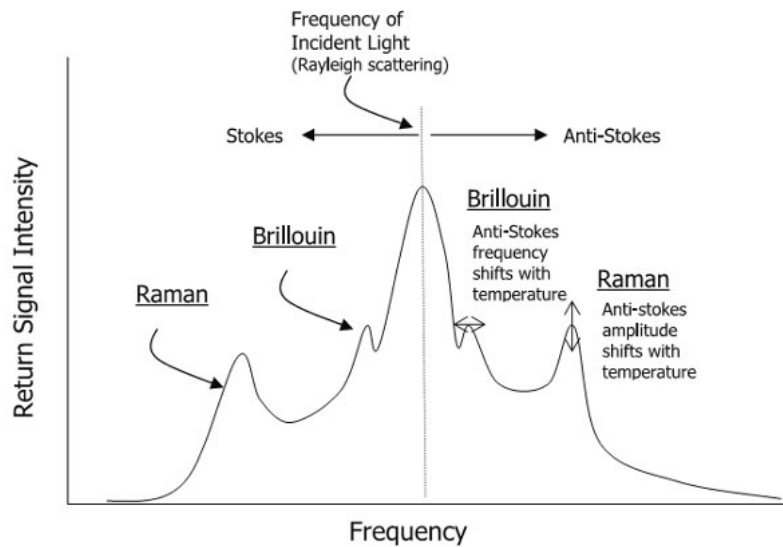


FIGURE 2.2: Diagram of Rayleigh, Raman, and Brillouin return scattering intensity below (Stokes) and above (Anti-Stokes) the frequency of the injected light (Selker et al., 2006).

The sampling theorem had to be considered for our measurements. This theorem defines the lowest physical resolution of measurements taken with a temporal resolution Δt by the Nyquist frequency f_N :

$$f_N = \frac{1}{2 \Delta t} \quad (2.2)$$

The temporal resolution of our DTS measurements was 30 s. Hence, f_N is 1 per 60 s (Eq. 2.2) and therefore, the physical resolution of our DTS measurement was 60 s.

Besides, temporal averaging was also necessary to achieve a better signal-to-noise ratio. The signal-to-noise ratio is inversely proportional to the LAF. But measurements were taken bidirectional, so the averaging of them provided a better signal-to-noise ratio. Accordingly, the temporal resolution is decreased to 60 s, however with a higher signal quality.

2.3 Deployment of CADEX

2.3.1 Transect setup

The 2-D fiber-optic array consisted of the six heights: -2 cm, 5 cm, 10 cm, 20 cm, 50 cm and 100 cm above ground (Fig. 2.3). Thus, DTS measurements were taken parallel to the ground. The fiber was inserted into the ground with a plow (Figure B.9). For above ground installation of the fiber, 1 m long poles were deployed every 12 m of the transect with special blocks (Fig. B.10) attached, to be able to hold the fiber in each height. Every pole was anchored with 2 nails in the ground and three anchoring cables (Fig. B.11). Pulleys and pulley-holder (Fig. B.12) strengthened the fiber at Point A and Point D. Further information is provided in field report of CADEX (Pfister et al., 2015).

2.3.2 Columns setup

The spatial resolution for the DTS-measurements was 1 m at the transect. An increase in vertical resolution was reached at Point B and D by extending the transect with two columns as suggested by Selker et al. (2006). Hence, the glass fiber was wound around the columns with a circumference of 1 m. Therefore, one winding represented one measurement of the DTS-technique. The columns were constructed out of white reinforcement fabric, which was stuck on transparent rings with circumference of 1 m (Fig. B.14 I and Fig. B.14 II). Column B and Column D were 3 m and 5 m high with one ring every meter (Fig. 2.4). Column D also measured water temperatures until a depth of 30 cm. Each column was wound from the top to the bottom. The glass fiber was stuck by 4 points of hot glue per winding (Fig. B.14 III). The distance between the windings was 1 cm in the lowest meter and 5 cm (Fig. B.1 I and Fig. B.1 II).

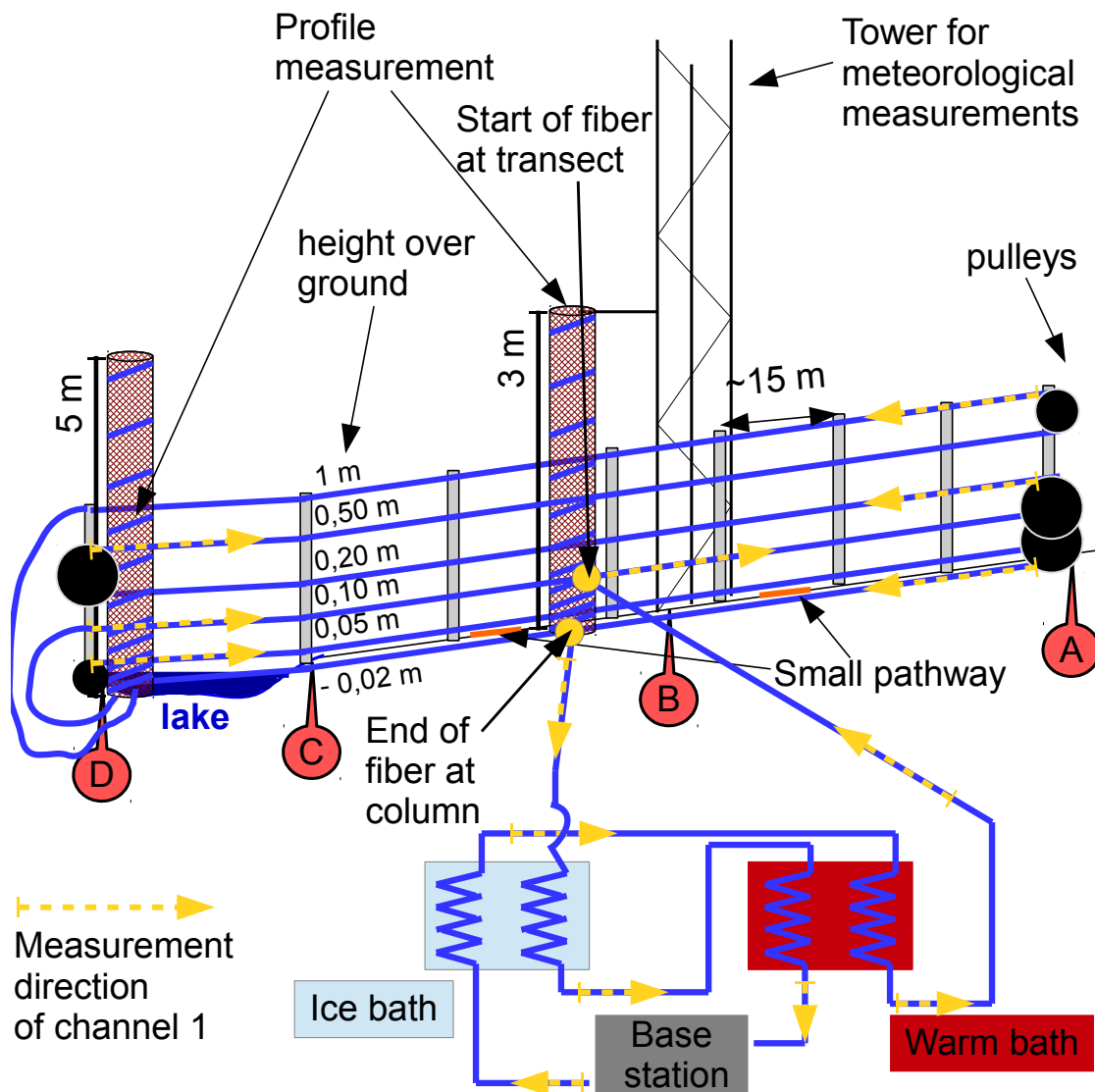


FIGURE 2.3: Draft of the setup of CADEX with 2-D fiber-optic array, both columns, calibration baths and the base station. Yellow arrows: measurement direction of Channel 1.

2.4 Flow and Flux measurements

For the flow and flux measurements two ultrasonic anemometers (Model CSAT3, Campbell Sci., Logan, UT, USA) were installed near Point B and at Point D. Near point B the first ultrasonic anemometer was installed upside-down in 10 cm above ground (Station B). The other one was mounted 2 m above the lake in combination with an open-path hygrometer (Model LI 7500, Serial Nr. 75H-0270, LI-COR, Lincoln, NE, USA) for turbulent flux measurements (Station D). All data were taken by two data loggers (Model CR3000, Campbell Sci., Logan, UT, USA) at 20 Hz. Additionally the data of the meteorologic tower of the EBG in 17 m height with a temporal resolution of 10 minutes was used for analysis (Station EBG). The declination in March and April ($\approx 3^\circ$) were taken into account in the analysis, but the angles in this section are given relatively to magnetic North.

Station B had to be exchanged, because rain water was able to drain into the tubes of the



(I) Column at the lake



(II) Column at the tower

FIGURE 2.4: Columns in the field



(I) Initial installation



(II) Final installation

FIGURE 2.5: Ultrasonic anemometer at the transect (Station B) before and after the water damage

ultrasonic anemometer and caused damage to the electronics on the 3rd April at 11:57 PM. Therefore, the ultrasonic anemometer and its electronic box were exchanged on 9th April 2015 (Fig. 2.5) and data between 3rd and 9th April was excluded from analysis. The angle to magnetic north and height above ground before and after the installation of the new ultrasonic anemometer did not change. The height above ground was 10 cm and the angle α_N between the -w-component of the ultrasonic anemometer and magnetic north was 328° (Figure 2.6).

At Station B the orientation and measurement of the three wind components (u,v and w) of

the ultrasonic anemometer completely changed due to the upside-down installation. The u-v-plane was vertical and the commonly used vertical wind component (w) was horizontal. Accordingly, the u-component of Station B measured vertical winds, while the v-component was transformed to the katabatic component to measure winds downhill and the w-component measured cross slope west-winds (Fig. 2.6). Thus, the commonly u-component changed to w-component, the commonly v-component to the negative v-component and the commonly w-component to the u-component for the computation of fluxes by the bmmflux-software as described in (Thomas et al., 2009). Accordingly, the change of the wind-components do not have to be considered for analysis. Besides, a list of all parameters computed by this software, is given in Table A.3.

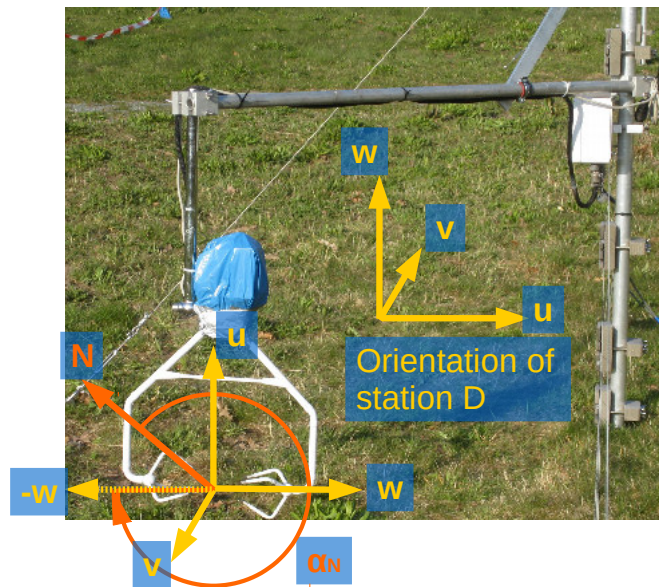


FIGURE 2.6: Upside-down installation of the Station B with the three measuring directions u , v and w (yellow arrows). Upper right corner: Common installation (e.g. Station D). α_N (orange): angle between magnetic North and the device.

On 17th March from 2:30 PM until 15:50 PM the mountings of the ultrasonic anemometer in combination with the open-path hygrometer at Station D were extended for better measurements of the fluxes above the lake (Fig. 2.7). The changes in orientation were considered in the computation of fluxes.

2.5 Quality control

Quality control for the flow and flux measurements included plausibility checks as well as tests for and removal of spikes, skewness and kurtosis. Whereas the measurements of the DTS were cleared from spikes, dropouts and artifacts.

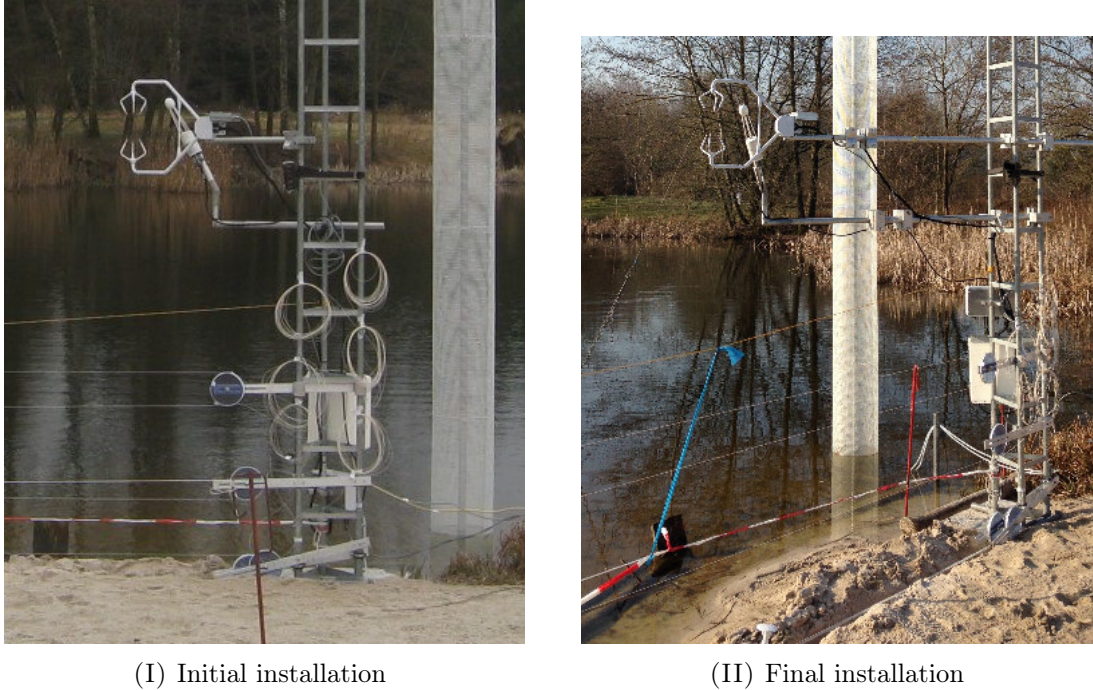


FIGURE 2.7: Installation of the ultrasonic anemometer and open-path hygrometer for flux measurements above the lake (Station D) before and after the extension of the mountings

2.5.1 Methods for flow and flux measurements

For computation of different fluxes the *bmmflux*-software, (Thomas et al., 2009) in MATLAB verion 8.4.0.150421 (R2014b) was used. This software set the plausibility limit for raw signal of wind components to $\pm 30 \text{ m s}^{-1}$ and for the sonic temperature signal to $-30 \text{ }^{\circ}\text{C}$ – 50°C . Afterwards despiking and calculation of skewness and kurtosis were applied according to Vickers and Mahrt (1997) within this software. For despiking of the time series a temporal sliding window of 300 s and an initial threshold value of 6.5 times the window’s standard deviation (σ_{window}) was used. Each spike was replaced using linear interpolation. If more than three consecutive data points in this time series were determined a spike, they were not removed. After removal and interpolation of spikes within this window, it shifted to the next measuring point of the time series and started despiking again, until it reached the end of the time series. The whole procedure was repeated five times until no spikes were detected. Besides, the skewness and kurtosis was calculated. For this purpose the data was linearly detrended and the higher moment statistics were computed (Vickers and Mahrt, 1997). The range for skewness was $[-2; 2]$ and $[1; 8]$ for kurtosis. Values of skewness or kurtosis outside the corresponding range were hard flagged and represented excursions from the mean that were beyond normal physical expectations. After computation of the flux by the software the hard flagged values and dependent fluxes were removed and linear interpolated by the surrounding 5 values in each direction.

TABLE 2.1: Quantity and percentage of full data set of hard flagged data of the measured variables not conforming to the skewness and kurtosis criterion. u, v, w, T: three wind components and the temperature measured by the ultrasonic anemometers, before and after 3D-rotation at both locations; H₂O: concentrations measured by open-path hygrometer at the lake

	Skewness				Kurtosis			
	Transect		Lake		Transect		Lake	
	N [-]	P [%]	N [-]	P [%]	N [-]	P [%]	N [-]	P [%]
u (unrotated)	27	0.4	21	0.3	118	1.7	78	1.5
v (unrotated)	24	0.4	20	0.3	98	1.5	57	0.8
w (unrotated)	30	0.4	44	0.7	460	6.8	265	3.9
u (rotated)	21	0.3	18	0.3	105	1.6	47	0.7
v (rotated)	23	0.3	23	0.3	115	1.7	71	1.1
w (rotated)	32	0.5	34	0.5	363	5.4	241	3.6
T	73	1.1	150	2.2	97	1.4	256	3.8
H ₂ O	-	-	395	5.9	-	-	593	8.8

2.5.2 Summary of flagged data from flow and flux measurements

About 65 000 raw data points of Station B were outside plausibility limits or assigned a spike, which is $\approx 0.9 \text{ ‰}$ of the raw data, while Station D at the lake reached a value of 3.1 ‰ resulting from 252 000 flagged raw data points. The water vapor concentrations measured by the open-path hygrometer at the lake had about 2.8 million flagged data, which is about 34.3 ‰ of the raw data. For the measurement of the three wind components (before and after 3D-rotation), the temperature and the H₂O concentration skewness and kurtosis was analyzed, flagged and interpolated (Tab. 2.1). For all values dependent on these factors the same procedure was implemented.

2.5.3 Methods for DTS-measurements

Plausibility check was performed and despiking was applied as described above, however with a sliding window of 2 hours, because of the much lower DTS measurement frequency of $\frac{1}{30}$ Hz compared to 20 Hz of the flux measurements, and a range of ± 6 times σ_{window} . In addition to spikes, dropouts were removed. Dropouts appeared for the heights 5 cm and 10 cm above the lake of the 2-D fiber-optic array, in case of touching the water surface. The dropouts were detected separately for these two heights. For this purpose a simple moving average (SMA) was applied to the time series of each measurement point above the lake. A SMA of 31st order (n=31) was used, which means that the SMA of one point in a time series (x(t) with x being the measured temperature) is the average of the temporal surrounding 15 data points in each direction (Equation 2.3 and 2.4). In this equations τ is used to mathematically center the SMA of a point in a time series in the temporal averaging range, which is $t \pm \tau$. After that the time series of one reference point was chosen. From this reference point all other time series of measuring points above the lake were subtracted. As they were measured simultaneously and a SMA was applied to each of them the difference should be small. If this difference was smaller than -1.4 K, it is determined as a dropout and

removed from the time series. The threshold value of -1.4 K was chosen, because the water temperature during night was noticeably higher than the air temperature, accordingly the difference between the reference point in the air and a measuring point, which hung in the water, must be negative.

$$x_{SMA}^n(t - \tau) = \frac{1}{n} \sum_{i=0}^n x(t - i) \quad (2.3)$$

$$\tau = \frac{n - 1}{2} \quad (2.4)$$

Supplementary to this quality control, artifacts from the setup of the glass fiber were considered. The artifacts were caused by the contact of the glass fiber with the rings holding the reinforcement fabric and the reinforcement fabric itself. Due to different heat capacity and bigger surface to volume ratios the glass fiber was additionally cooled down or heated up. As the glass fiber was wound around the rings, conduction took place and caused an error for up to 8 measurement points for one ring in the column. At the lake the temperature difference of one ring was up to 2.5 K colder than mean of ten surrounding measurements. At the transect this temperature difference was up to -2.9 K. The position of the rings were known from setup and the transfer matrix and the artifacts accordingly removed and linear interpolated by 10 surrounding measurement points. The measuring error caused by the reinforcement fabric during day was modeled to be up to + 0.9 K for one meter of glass fiber, with a supposed thermal conductivity of $0.1 \text{ W K}^{-1} \text{ m}^{-1}$ of the reinforcement fabric (Sigmund (2015), unpublished). Since this value is modeled and the thermal conductivity of the reinforcement fabric was unknown, this artifact could not be removed. Instead, the measurements of the columns were compared to the corresponding measurements of the transect.

2.5.4 Summary of flagged data from DTS-measurements

All measurements were within the plausibility limits. Spike detection revealed a total number of about 6900 spikes in the transect, while at column D about 2000 spikes and at column B about 1400 spikes were detected. These quantities were under 0.1 ‰ of all measurements taken at each station. Detailed number of spikes and percentage of full data set in per mill for each day is shown in Table A.4. Finally a quantity of about 260 000 dropouts was found for the height 5 cm above the lake of the transect, representing 11.4 ‰ of all measurements taken at this height. The quantity and percentage of dropouts for the height 10 cm above ground was comparatively small ($\approx 16\,000$ dropouts, 0.7 ‰). Detailed number of dropouts and percentage of full data set in per mill for each height for each day is shown in Table A.5.

3. Analysis of CADEX

3.1 Validation of DTS-measurements

All analysis and visualization was done by using R version 3.1.2 (R Core Team, 2014). The DTS-measurements were evaluated by comparing with the measurements of a platinum resistance thermometer (Pt100, Electrotherm, Geraberg, Germany). The Pt100 was mounted in 5 cm height at Point B and compared with the nearest point of the 2-D fiber-optic array in the same height. Furthermore, the measurements of Column B and Column D were checked for artifacts of the reinforcement fabric by comparing with the nearest temperature measurements of the 2-D fiber-optic array.

Resolution of inductive analysis was determined to 10-minutes averages as data from the meteorologic measurement tower was only available for this averaging period. To recap the variance of measurements within this averaging period, the standard deviation σ for the wind velocity and wind direction in 0.1 m height ($u_{0.1 m}$ and $\varphi_{0.1 m}$) as well as DTS-measurements (Tf) was computed. Therefore $u_{0.1 m}$ and $\varphi_{0.1 m}$ were averaged over 30 s by the bmmflux-software, consistent with the temporal resolution of DTS-measurements, and then the standard deviation within 10 minutes was calculated. A different approach to calculate the standard deviation of $\varphi_{0.1 m}$ was chosen, as the standard process is not applicable for wind directions. Hence, $\sigma_{\Delta\varphi_{0.1 m}}$ is the 10-min-average of the difference between consecutive 30-s- $\varphi_{0.1 m}$ measurements ($\Delta\varphi_{0.1 m}$).

3.2 Classification in Night-Classes

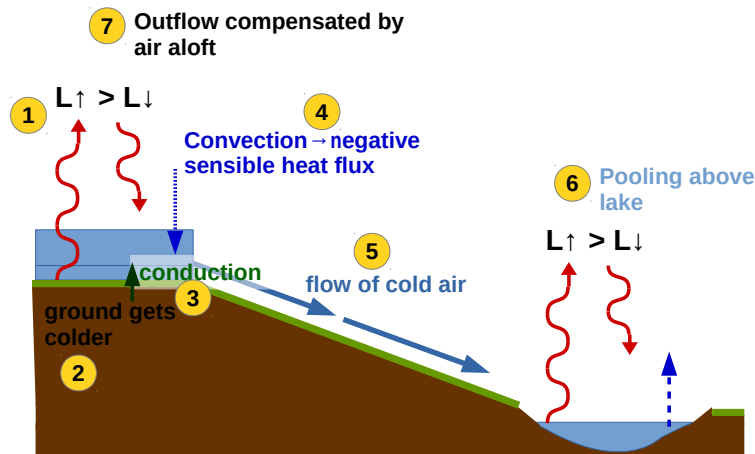


FIGURE 3.1: Draft of cold-air formation, drainage and pooling on the local slope during cloudless, calm nights. $L\uparrow/L\downarrow$: up-/downwelling longwave radiation

The formation of cold air was possible in calm nights with clear skies (e.g. Foken 2008, Mahrt et al. 2014b, Burns and Chemel 2015). In these nights, the balance of longwave radiation (I_{net}) was positive, due to more upwelling than downwelling longwave radiation ($L\uparrow > L\downarrow$). If there were clouds, I_{net} would have been much smaller due to absorption and re-emission of $L\uparrow$. During such conditions, the cold-air layer in valleys can be reduced by 75% (Barr and Orgill, 1989) and temperature gradients near the ground are much smaller (Geiger et al., 1995). But as we measured on a spatial much smaller scale, clouds lead probably to the erosion of cold-air drainage. During cloudless calm nights, the ground of the whole slope got colder, because of a high I_{net} . Therefore, the air with direct contact to the ground cooled down through conduction. Accordingly, a thin cold-air layer developed, which could grow with time through convection, resulting in a negative sensible heat flux directed downward to the ground. The inclination of the slope induced a gravity driven terrain following flow of the cold air with a high density, i.e. cold-air drainage. At the end of the slope, cold-air pooling above the lake could theoretically take place. The cold-air outflow was compensated by warmer air from above, closing the cycle of cold-air formation, drainage and pooling (Fig. 3.1). If it was not calm, the process of cooling was interrupted by turbulence entrainment of moderate to strong winds (e.g. Barr and Orgill 1989, Soler et al. 2002, Mahrt et al. 2014a, Geiss and Mahrt 2015). Therefore, conduction and especially convection were less effective and cold-air drainage was not possible (Fig. B.8).

The conditions for cold-air formation and drainage can be described by I_{net} , $u_{0.1 m}$ and $\varphi_{0.1 m}$ during night. The prevailing $\varphi_{0.1 m}$ and distribution of $u_{0.1 m}$ were analyzed by wind roses of Station B in combination with wind velocity classes by the package 'openair' in R (Carslaw and Ropkins, 2012). From these results, an inductive analysis on basis of the following factors with several sub-factors was conducted:

- day and night indicator, calculated from zenith angles (DNT):
Day, Night and Transition
- wind direction of the ultrasonic anemometer in 0.10 m height ($\varphi_{0.1 m}$):
W (255°-285°), ENE (45°-75°) and SSW (195°-225°)
- balance between the up- and downwelling longwave radiation (I_{net}):
< 10 W m⁻², 10-80 W m⁻² and >80 W m⁻²
- wind velocity of the ultrasonic anemometer in 0.10 m height ($u_{0.1 m}$):
0-1 m s⁻¹, 1-2 m s⁻¹, 2-3 m s⁻¹ and > 3 m s⁻¹

DNT determined sunrise and sunset based on zenith angles, accordingly night data could be chosen and analyzed. The analysis of wind roses of Station B in 0.1 m height revealed the three main wind directions W, ENE and SSW (Fig. B.3). Especially the wind direction of ENE was important, as it indicated cold-air drainage down the slope. Further, a big range for I_{net} from 10 W m⁻² to 80 W m⁻² was chosen to capture even small I_{net} , occurring before sunrise. During this period, cold-air formation and drainage could still take place, if the surface was cooled down enough to maintain these processes. And finally, the four $u_{0.1 m}$ -classes were chosen to classify the strength of flow. The combination of all factors and their sub-factors resulted in 108 categories, for which the 10-min averaged data was tested.

The first four most appearing night-classes were chosen for inductive analysis from the 31 found categories (Tab. A.2):

- Night-Class W : $\varphi_{0.1 m} W$, $I_{net} = 10-80 \text{ Wm}^{-2}$ and $u_{0.1 m} = 0-1 \text{ ms}^{-1}$
- Night-Class ENE 1: $\varphi_{0.1 m} \text{ ENE}$, $I_{net} = 10-80 \text{ Wm}^{-2}$ and $u_{0.1 m} = 0-1 \text{ ms}^{-1}$
- Night-Class ENE 2: $\varphi_{0.1 m} \text{ ENE}$, $I_{net} < 10 \text{ Wm}^{-2}$ and $u_{0.1 m} = 0-1 \text{ ms}^{-1}$
- Night-Class ENE 3: $\varphi_{0.1 m} \text{ ENE}$, $I_{net} = 10-80 \text{ Wm}^{-2}$ and $u_{0.1 m} = 1-2 \text{ ms}^{-1}$

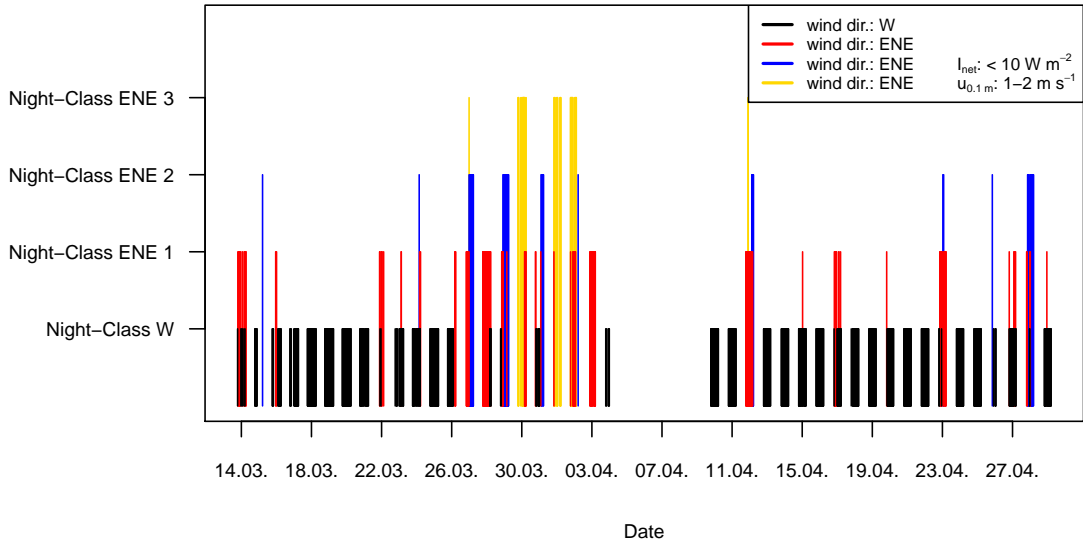


FIGURE 3.2: Temporal distribution of the four night-classes.

Cold-air drainage was expected for the physical properties of Night-Class ENE 1. Further, Night-Class ENE 2 and Night-Class W should be different, as Night-Class ENE 2 had adverse conditions for cold-air formation and Night-Class W had a near bottom flow directed perpendicular to the slope. Besides, Night-Class ENE 3 should be different as well, as this high values of $u_{0.1 m}$ were not expected for cold-air drainage. The slope was too small to accelerate the cold air to such high velocities. Accordingly, this night-class was probably vertically coupled. Besides, only mean flow and perturbations were computed in analysis, as the night-classes did not differentiate between different days. The temporal distribution of the four night-classes can be seen in Figure 3.2.

3.2.1 Investigation of vertical decoupling

The vertical coupling of processes can be revealed through analysis of correlations. Therefore, the four parameters $u_{0.1 m}$, $u_{17 m}$, the vertical wind direction shear φ_{shear} and the friction velocity in 0.1 m $u_{0.1 m}^*$ were set in relation to each other. The friction velocity $u_{0.1 m}^*$ takes the vertical wind velocity into account and is therefore a measure of the momentum

exchange:

$$u^* = \sqrt{u'w'^2 + v'w'^2} \quad (3.1)$$

If $u^*_{0.1 m}$ is enhanced, e.g. during vertical wind velocity and direction shear, the momentum exchange and therefore the turbulence entrainment increase.

The correlation and association between these four parameter can reveal three main idealized relation between processes in 0.1 m and 17 m: (i) vertical decoupling, (ii) vertical coupling with high φ_{shear} and (iii) vertical coupling with low φ_{shear} . (i) Vertical decoupling is expected during cold-air drainage and pooling defined as an independent process near the ground (e.g. Mahrt et al. 2001). Hence, no correlation between all four parameters exist (red arrows, Fig. 3.3). (ii) Vertical coupling with high φ_{shear} is expected for high $u_{17 m}$ inducing vertical wind velocity shear and consequently forcing a recirculation near the ground. Therefore, $u_{0.1 m}$ and $u^*_{0.1 m}$ are coupled with $u_{17 m}$. An enhanced $u_{17 m}$ increase $u_{0.1 m}$ and $u^*_{0.1 m}$, because of a higher recirculation and increased turbulence entrainment, respectively. Accordingly, $u_{0.1 m}$, $u_{17 m}$ and $u^*_{0.1 m}$ correlate. (iii) Vertical coupling with low φ_{shear} is expected for $u_{17 m}$ with enough synoptic forcing to develop the typical logarithmic wind profile. Then wind velocities have a high correlation in combination with low $u^*_{0.1 m}$ and φ_{shear} (green arrows, Fig. 3.3).

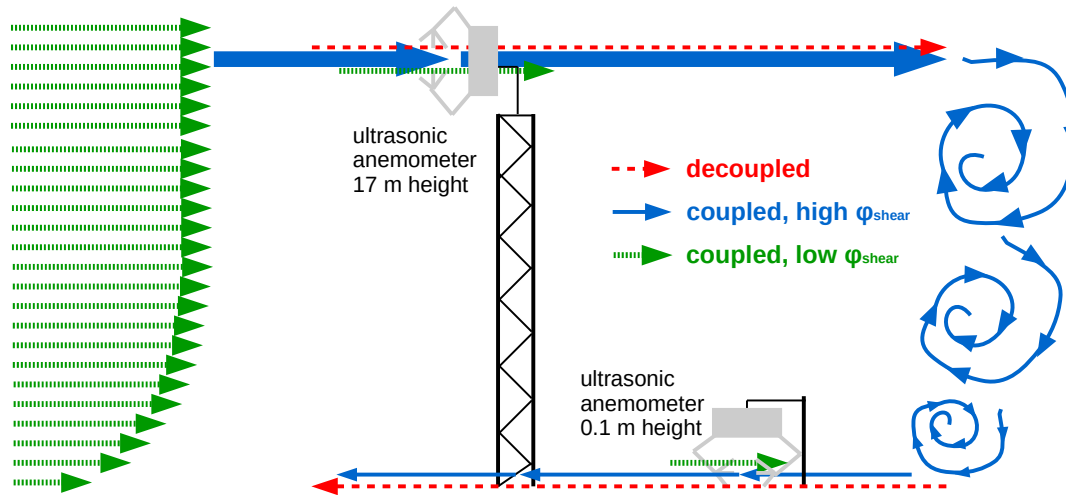


FIGURE 3.3: Draft of vertical relations between Station EBG (17 m) and Station B (0.1 m). Arrows show the wind direction. red: vertical decoupling; blue: vertical coupling with high wind direction shear (φ_{shear}); green: vertical coupling with low φ_{shear} .

To test the strength of correlation, Kendall's rank correlation coefficient τ_R between two variables was computed in R and tested for the null hypothesis, that there is no association between the variables under study (McLeod, 2011). The maximum tolerable probability α of the p-value is 5 %, i.e. the null hypothesis will be discarded with a significance of $1-\alpha$ (i.e. 95 %). Kendall's τ_R measures the strength of dependency between two variables, which do not have to be normally distributed, because τ_R is calculated by the number of concordant

and discordant pairs:

$$\tau_R = \frac{n_c - n_d}{\frac{1}{2}n(n-1)} \quad (3.2)$$

n_c : number of concordant pairs
 n_d : number of discordant pairs
 n : number of all pairs

A concordant pair are two simultaneously increasing or decreasing parameters, whereas a discordant pair are two diverging parameters.

The correlation and association between φ_{shear} and $u_{0.1 m}$ of Station B were evaluated and τ_R computed. Then, Coplots set the correlation between $u_{0.1 m}$ and $u_{17 m}$ in relation to different φ_{shear} -classes. Therefore, the data of $u_{0.1 m}$ and $u_{17 m}$ were subset by the quartile of φ_{shear} and a $u_{0.1 m}$ - $u_{17 m}$ -plot as well as a τ_R of both parameters compiled for each quartile. The quartile of φ_{shear} were visualized by horizontal bars on top of the Coplots, with the four $u_{17 m}$ - $u_{0.1 m}$ -subplots below. If φ_{shear} had an impact on the relation between $u_{17 m}$ and $u_{0.1 m}$, the subplots of the Coplots should differed. At least, a $u_{0.1 m}$ - $u_{17 m}$ -plot was combined with a $u_{0.1 m}$ - $u_{0.1 m}^*$ -plot with the data of all night-classes for evaluation of the momentum exchange.

After testing for vertical decoupling, the data was examined for prevailing wind directions. Therefore, the $\varphi_{17 m}$ - $u_{17 m}$ -plot of all night-classes with $\varphi_{0.1 m}$ W were evaluated and compared with the night-classes with $\varphi_{0.1 m}$ ENE.

3.2.2 Spatial temperature distribution

Spatial temperature differences were disentangled by the horizontal and vertical perturbation of temperature θ^* . Commonly the potential temperature θ instead of the absolute temperature T is used to take into account the warming or cooling of an air parcel, during the dry-adiabatic (i.e. without exchanging energy or moist with the environment) falling or rising to the 1000-hPa pressure level. For this purpose the dry adiabatic temperature gradient $\Gamma_d = 9.81 \text{ K km}^{-1}$ is applied. But as the maximum height difference from Point A to Point D was 4.3 m, the resulting temperature difference between those points was 0.04 K and neglected.

The perturbation θ_i^* of each Point i in the 2-D fiber-optic array was defined as the deviation from the spatial, i.e. horizontal or vertical, mean Tf-temperature. The horizontal perturbation was computed by calculating the spatial mean of Tf (μ_{horiz}) of one height and subtracting μ_{horiz} from each Point i of this height (Eq. 3.3). This was done for every height in the transect and for every time step. The same was done vertically (Eq. 3.4).

$$\text{horizontal} : \theta_{i, horiz}^* = \theta_i - \mu_{horiz} \quad (3.3)$$

$$\text{vertical} : \theta_{i, verti}^* = \theta_i - \mu_{verti} \quad (3.4)$$

The horizontal and vertical perturbation of each Point i was then averaged over time separately for each night-class. Accordingly, the horizontal and vertical mean perturbation ($\mu_{\theta_{horiz}^*}$ and $\mu_{\theta_{verti}^*}$) were compared between the night-classes. The averaging was necessary, because the night-classes did not differentiate between days. The computed data was plotted in R as a color filled Contour-Plot with the distance to Point A as abscissa, the height in the transect as ordinate and the depicted mean of θ^* visualized as contours and colors. A high range of θ^* revealed intense horizontal or vertical temperature differences. Additionally, the different domains along the transect as introduced in Section 2.1 could be compared.

To exclude cold-air pooling above the slope, the local slope was tested and classified for different types of cold-air pools. The types are classified in terms of the stratification and gradient of potential temperature along the slope (Mahrt and Heald, 2015). The stratification above the slope was evaluated by the cold-air pool intensity(CPI) and the gradient of potential temperature by the horizontal θ^* on top of the slope. Therefore, the type of cold-air pool could be described (Fig. 3.4, according to Mahrt (personal communication)). The CPI is defined as the potential temperature difference between top and bottom of slope:

$$\text{CPI} = \theta_{top} - \theta_{bottom} \quad (3.5)$$

For this purpose the dry adiabatic temperature gradient Γ_d was as well not applied and absolute temperatures used instead. If $\text{CPI} \gg 0$ and $\theta_{top}^* > 0$ on top of the slope, there was a huge temperature difference between the top and the bottom of the slope indicating a mature CP (top, Fig. 3.4). If $\text{CPI} \approx 0$ and $\theta_{top}^* \approx 0$ combined with high vertical temperature gradients, there was no horizontal temperature difference indicating overlaying regional CP inducing a thermal stratified terrain following flow (bottom, Fig. 3.4).

Top of slope was at 45 m distance from Point A and bottom of slope at distance 136 m, which were both above the meadow-domains. These two reference points were chosen, to be aware of influences on the cold-air formation by the different domains. The CPI and θ_{top}^* was then calculated for the height 20 cm of the transect. This height was chosen, as the two lower heights had contact with the ground and therefore some artifacts.

For an ecological assessment the probability for frost was investigated. Therefore, the frost risk percentage $P_{\text{frost risk}}$ as described in François et al. (1999) was used. In our study $P_{\text{frost risk}}$ was calculated for DTS-data with a threshold of 0°C . Therefore, for each measurement point of one height the total amount of $T_f < 0^\circ\text{C}$ was identified and divided by the quantity of taken measurements. This was done separately for each category and $P_{\text{frost risk}}$ plotted as Contour-Plot of the 2-D fiber-optic array.

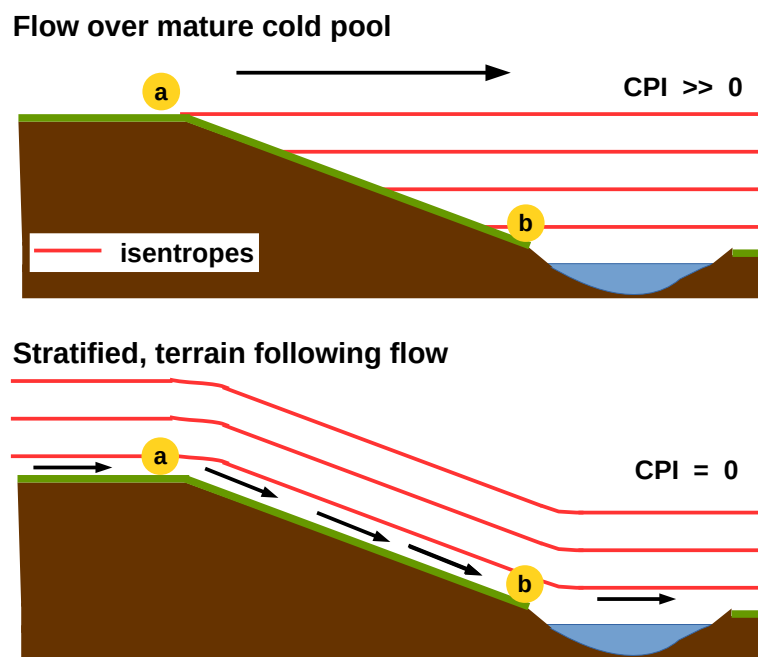


FIGURE 3.4: Two idealized limits of cold-air pools according to Mahrt (personal communication). CPI: cold pool intensity; red lines: isentropes; black arrows: flow direction; Point a and b: points for calculating CPI

3.3 Case Studies

After interpretation of the night-classes, four nights from 07:00 PM until 05:00 AM of the next day were chosen as case studies and analyzed with regard to vertical decoupling and spatial temperature distribution. Therefore, the wind velocities and directions were combined with a contour plot of the temperatures along the slope in 20 cm height. Besides, the multiresolution decomposition of the temperature signal was implemented and the spatial correlation computed (Section 3.3.1). The case studies were:

Case Study 1: 19.03. (Night-Class W)

Case Study 2: 27.03. (Night-Class ENE 1)

Case Study 3: 11.04. (Night-Class ENE 1-3)

Case Study 4: 16.04. (Night-Class ENE 1 and Night-Class W(variantly))

The case studies will be named with their number together with the most appearing night-class in brackets (e.g. Case Study 1 (Night-Class W)). For evaluation of spatial difference in temperature development the multiresolution decomposition (MRD) of temperature time series in 5 cm was applied for each case study and the spatial two-point correlation coefficient R_{ij} calculated (Section 3.3.1). This way the dependence of temperature development on different time scales was set into spatial relation. For visualization, R_{ij} was plotted against the separation distance between Point i and Point j for the different time scales. If R_{ij} of one time scale remained high for all separation distances, the temperature development during this time scale was spatially coherent (Thomas, 2011). Accordingly, a faster decrease of R_{ij} with increasing separation distance revealed spatially different processes involved in the temperature development.

On the 20th of April from 07:00 PM to 11:00 PM a fog experiment was conducted. Night-Class W was the most appearing night-class. The air movements during night could be examined by the flow of the synthetic fog, which was released by a fog machine (Antari, 21000 MK II, Musikhaus Thomann, Burgebrach, Germany) at two points. For the first half of the experiment the fog was released near Station B, while during the second half this was done at the bank of the lake near Station D. To make the fog visual, a vertical plane of light parallel to the transect was created by a laser (Stairville, DJ Lase 400-B Blue, Musikhaus Thomann, Burgebrach, Germany). Then several pictures and some picture series (10 pictures, 1 Hz) were taken with a reflex camera at different locations along the transect.

3.3.1 Multiresolution decomposition (MRD)

A multiresolution decomposition (MRD) is performed by averaging time series at different lengths, i.e. viewing data at different temporal resolution. Therefore, sub-records of dyadic width (2^n) were used as averaging lengths. Based on the difference between data at two different resolutions, the multiresolution cospectra can be developed. This approach provides a link to Reynolds averaging (Howell and Mahrt, 1997). As described in Thomas (2011) cold-air drainage flows are characterized as local and non-periodic submeso motions, for which the

multiresolution decomposition technique was found suitable (e.g. Mahrt 2008; Mahrt et al. 2009). This simplest possible wavelet basis set offers several advantages over other commonly applied spectral decomposition techniques such as the fast Fourier transform (FFT) as it does not assume any periodicity of the signal, the spectral peak corresponds to the dominant local event, it satisfies Reynolds averaging independently at all scales, and it has a finer resolution for smaller averaging lengths compared to the global FFT.

Data were divided into 64-min sub-records, each overlapping by 4 minutes to start every hour with decomposing. Each 64-min sub-record is decomposed into 2^{M-m} different averaging windows of 2^m data points with $m = M, \dots, 0$. Accordingly, M determines how many multiresolution modes (m) are performed. In this study, the 64-min sub-records consisted of 64 data points as the temporal resolution of the DTS-technique was one minute. Hence, the maximum number of data points in one window is $2^{m=M} = 64$ with $M = 6$. The corresponding temporal averaging intervals of one window or so called multiresolution time scales are $2^m = 64, 32, 16, 8, 4, 2, 1$ min. Accordingly $m = M$ refers to the record mean of the 64-min sub-record, while $m = 0$ describes the original signal. The temperature signal (Tf) obtained by the DTS-technique can be written as the sum of all m multiresolution modes for the p^{th} sub-record such that

$$\overline{\text{Tf}}(p) = \frac{1}{M} \sum_1^M \text{Tf}_m(p) \quad (3.6)$$

with $m = M, \dots, 0$

The MRD was performed on the case studies. After the temporal multiresolution decomposition a two-point correlation coefficient R_{ij} as a function of the separation distance between two points (d_{ij}) was evaluated. R_{ij} is defined as the spatial correlation coefficient for the different MRD-modes, i.e. the multiresolution time scales of the temperature signal Tf:

$$R_{ij}(d_{ij}) = \frac{\overline{\text{Tf}_i' \text{Tf}_j'}}{\sigma_{\text{Tf}_i} \sigma_{\text{Tf}_j}} \quad (3.7)$$

The primes denote the deviation from the temporal average over the multiresolution time scale.

The two-point correlation coefficient was performed for the data of the transect for each height separately. One measurement of the height was chosen as Reference Point i and separation distances (d_{ij}) computed. A negative d_{ij} indicated that the Point j lay uphill to the Reference Point i and for a positive d_{ij} the Point j lay downhill. The range of R_{ij} is $[0,1]$. A R_{ij} -value of zero means no correlation between the two points and a R_{ij} -value of 1 means highest correlation between both points.

4. Results

4.1 Validation of DTS-measurements

Measurements of the temperature sensor Pt100 (T_{Pt100}) were compared with the nearest DTS-measurements in 5 cm (T_f). The course of both measurements was similar, but especially during day the temperature peaks of T_{Pt100} at noon were much bigger (Fig. 4.1). This corresponded to the higher range of T_{Pt100} from $-7.7\text{ }^\circ\text{C}$ up to $35.2\text{ }^\circ\text{C}$ compared to the range of T_f ($-7.9\text{ }^\circ\text{C}$ – $26.2\text{ }^\circ\text{C}$). The median of the difference between both measurements ($\Delta T = T_{\text{Pt100}} - T_f$) showed that T_{Pt100} was about 1.1 K warmer than T_f during day and about 0.2 K warmer than T_f during night. However, the standard deviation of ΔT was high during day (3.9 K) and low during night (0.7 K).

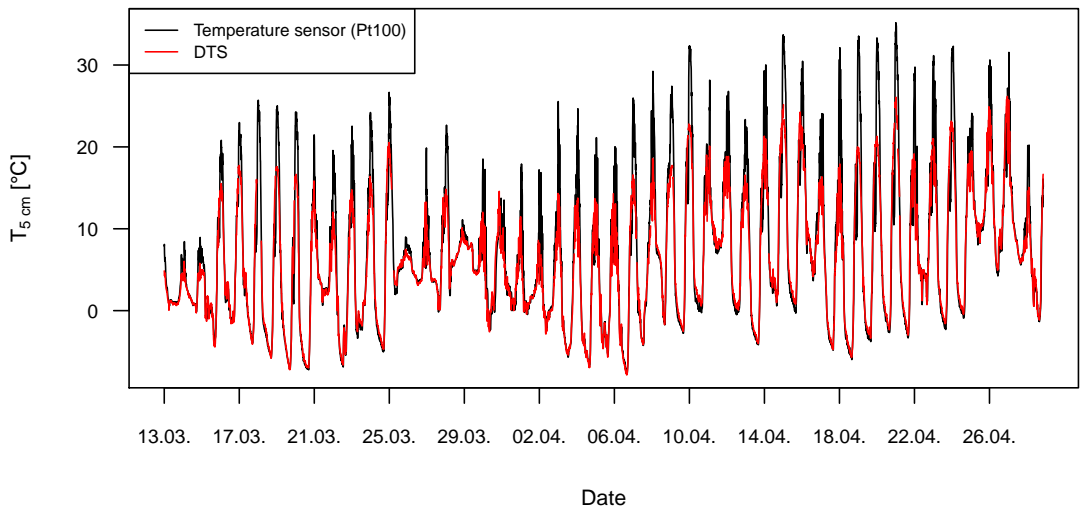


FIGURE 4.1: Temperature measurements in 5 cm height ($T_{5\text{ cm}}$) with two different devices. black: temperature sensor Pt100; red: DTS-technique.

The comparison between the DTS-measurements of the columns and of the corresponding 2-D fiber-optic array also revealed temperature differences ($\Delta T_f = T_{f_{\text{column}}} - T_{f_{\text{transect}}}$) from -5.7 K up to 4.0 K at Point B and from -6.2 K up to 4.9 K at Point D (Lake). The computed median of ΔT_f was 0.3 K and -0.1 K , respectively. Accordingly, the measurements of Column B were in the median 0.3 K higher than the measurements of the transect, while at the lake the measurements of Column D were slightly lower.

The standard deviation of T_f σ_{T_f} within an 10-min averaging interval ranged from 0 K to 3.8 K . The standard deviation during day was especially high with a median of 0.4 K with a maximum of 3.8 K and low during night with a median of 0.3 K with a maximum of 1.5 K (top, Fig. 4.2).

The standard deviation of the wind velocity $\sigma_{u_{0.1m}}$ within an averaging period of 10 minutes was between 0.01 m s^{-1} and 1.03 m s^{-1} with a median of 0.16 m s^{-1} for the full measurement

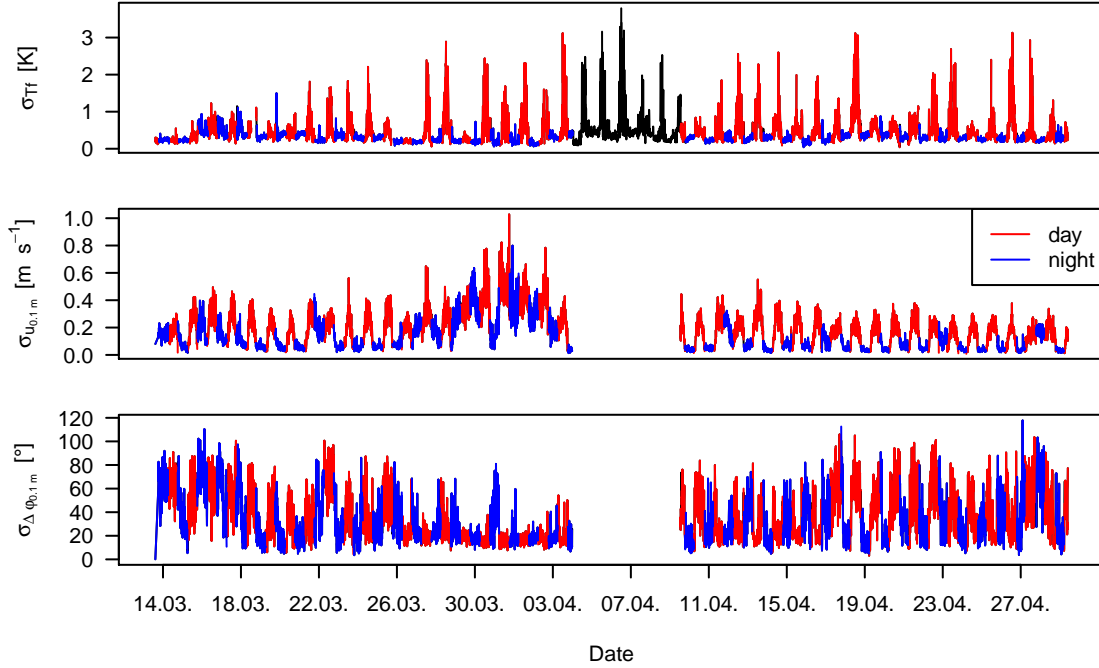


FIGURE 4.2: Standard deviation of the glass fiber temperature (σ_{Tf}), of wind velocity in 0.1 m height ($\sigma_{u_{0.1m}}$) and of the wind direction change in 0.1 m height ($\sigma_{\Delta\varphi_{0.1m}}$) within an averaging period of 10 minutes. red: during day; blue: during night; gap: malfunction of ultrasonic anemometer.

period for Station B (center, Fig. 4.2). During night $\sigma_{u_{0.1m}}$ was even lower with a median of 0.07 ms^{-1} , whereas the median of $\sigma_{u_{0.1m}}$ during day was 0.21 ms^{-1} .

The median of the standard deviation of the wind direction $\sigma_{\Delta\varphi_{0.1m}}$ was 28.3° , however with a range from 0.1° to 117.9° for the full measurement period (bottom, Fig. 4.2). Accordingly, $\sigma_{\Delta\varphi_{0.1m}}$ was high with a median of 33.4° at day and 24.8° at night.

4.2 Investigation of vertical decoupling

4.2.1 Vertical correlation of wind velocities and directions

The φ_{shear} - $u_{0.1m}$ -plot showed a high variance between the night-classes especially in the range and distribution of both parameters (Fig. 4.3). Night-Class W was the most appearing night-class with 1195 found measurements (Fig. 4.3 a). Even though the range of $u_{0.1m}$ was determined $< 1 \text{ ms}^{-1}$ for Night-Class W, all $u_{0.1m}$ were $< 0.4 \text{ ms}^{-1}$. Besides, φ_{shear} revealed values throughout the entire range, but most data points could be found around 110° . Further, the parameters had no associations, verified by a not significant τ_R close to zero.

For Night-Class ENE 1 the amount of measurements was only about a fifth of the amount for Night-Class W (Fig. 4.3 b). Further, Night-Class ENE 1 had $u_{0.1m}$ throughout the entire range and φ_{shear} had a smaller range from 50° to 180° . Besides, two main patches could be found. In the first patch, φ_{shear} ranged from 50° to 110° and $u_{0.1m}$ was $< 0.4 \text{ ms}^{-1}$. Whereas in the second patch φ_{shear} was $> 150^\circ$ and most values of $u_{0.1m}$ between 0.4 and 1.0 ms^{-1} .

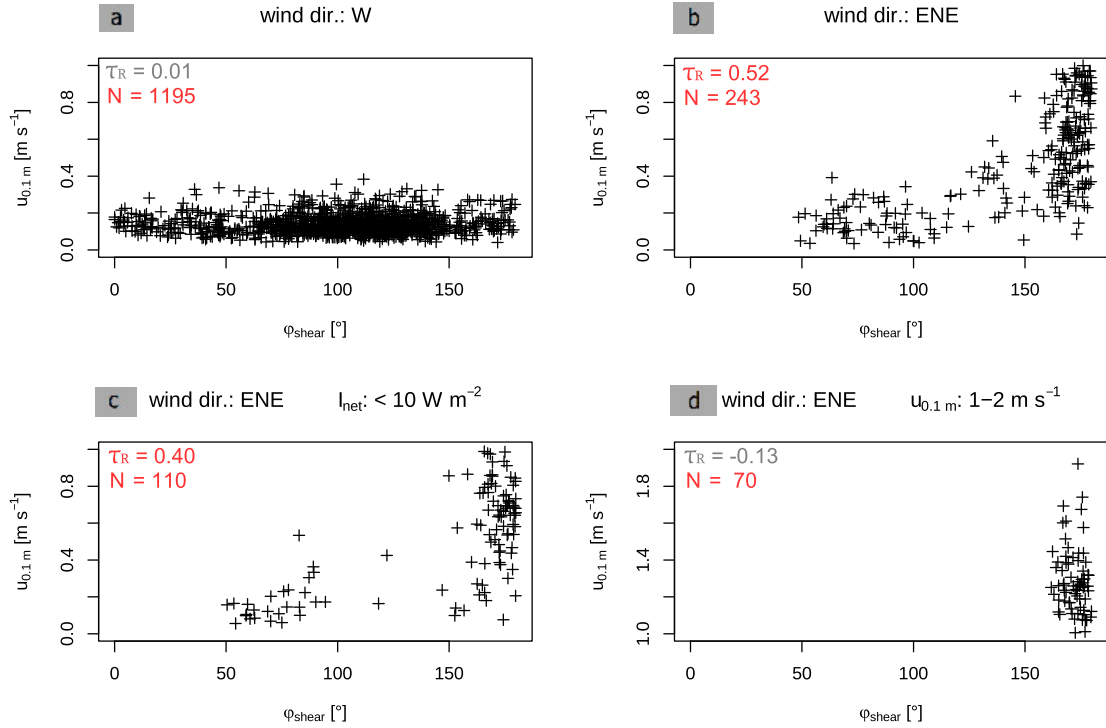


FIGURE 4.3: Correlation between vertical shear of wind direction in 17 m and 0.1 m (φ_{shear}) and wind velocity in 0.1 m ($u_{0.1 m}$) for all four night-classes. a: Night-Class W; b: Night-Class ENE 1; c: Night-Class ENE 2; d: Night-Class ENE 3; τ_R (red): correlation coefficient; τ_R (grey): insignificant τ_R ; 'N' (red): number of measurements.

Besides, the first patch only included about a quarter of all measurements. Accordingly, the transition from low to high values of $u_{0.1 m}$ simultaneously with increasing φ_{shear} showed a significant τ_R of 0.52, which was the highest correlation of all four night-classes.

Night-Class ENE 2 was almost identical to Night-Class ENE 1 (Fig. 4.3 c). Both had the same range and distribution of $u_{0.1 m}$ and φ_{shear} . However, the two patches were more separated and τ_R was smaller (0.40). Further, the number of measurements were even less. Finally, Night-Class ENE 3 had the highest $u_{0.1 m}$ and only φ_{shear} of $> 150^\circ$ (Fig. 4.3 d). In this small range of φ_{shear} , τ_R was insignificant and no association between parameters could be found.

The Coplot of Night-Class W revealed only small ($\tau_R < 0.14$) or no correlation between $u_{0.1 m}$ and $u_{17 m}$ (Fig. B.4). Further, $u_{17 m}$ was mainly $< 2 \text{ ms}^{-1}$ and $u_{0.1 m}$ was $< 0.4 \text{ ms}^{-1}$.

In contrast, Night-Class ENE 1 had high correlation coefficients τ_R (≥ 0.64) for all quartiles of φ_{shear} with exception of the smallest with a τ_R of 0.30 (Fig. 4.4). Accordingly, $u_{0.1 m}$ and $u_{17 m}$ correlated well for $\varphi_{shear} > 110^\circ$. But even for $\varphi_{shear} < 110^\circ$ a significant, small correlation could be found. Additionally, $u_{0.1 m}$ was $< 0.4 \text{ ms}^{-1}$ for $\varphi_{shear} < 110^\circ$. Besides, almost all $u_{17 m}$ were $> 1 \text{ ms}^{-1}$. Further, the range of the φ_{shear} -quartiles got distinctly smaller for higher values of φ_{shear} . The first and second quartile had a big range (50° - 110° and 110° - 165°), whereas the third and fourth quartile had much smaller ranges of 165° - 172° and 172° - 180° , respectively.

Night-Class ENE 2 was again almost identical to Night-Class ENE 1 with two exceptions

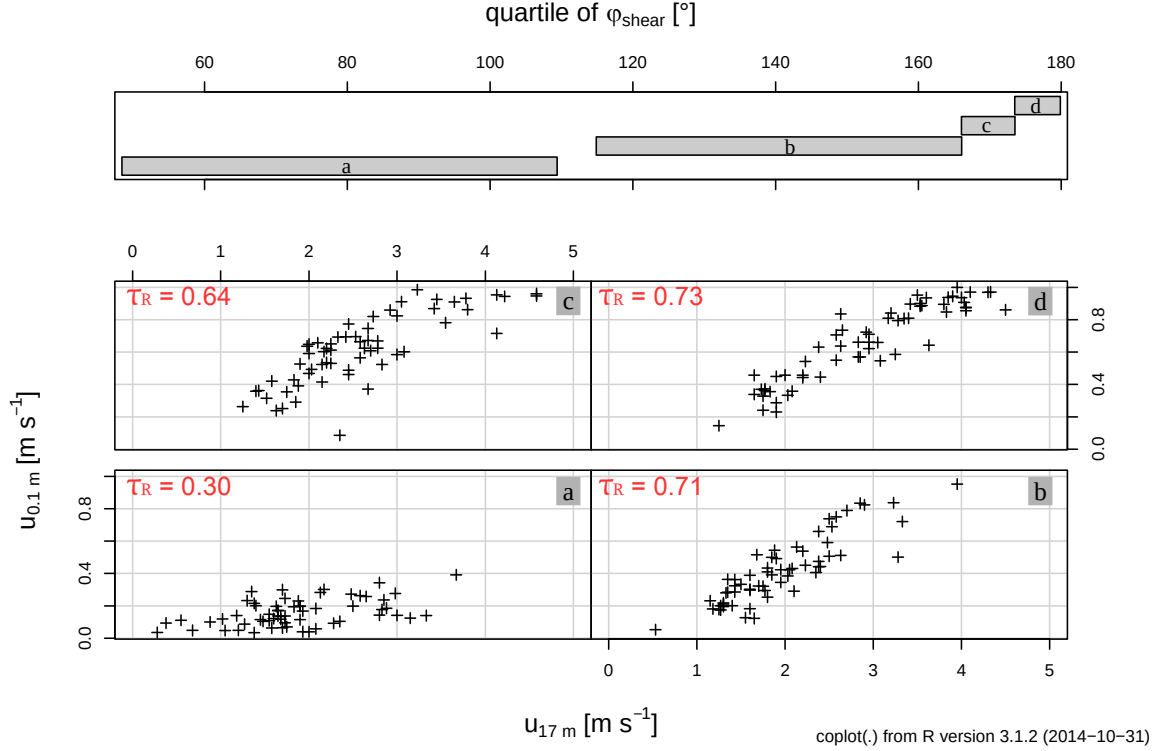


FIGURE 4.4: Coplot of Night-Class ENE 1: Scatter plot of wind velocities in 0.1 m and 17 m ($u_{0.1\text{ m}}$ and $u_{17\text{ m}}$) sectioned by quartile of vertical wind direction shear φ_{shear} . ' τ_R ' (red): correlation coefficient

(Fig. B.5). First, for smallest φ_{shear} -quartile (Subplot a) no significant correlation found. Second, the correlations of the other three φ_{shear} -quartiles revealed even slightly bigger τ_R (0.67-0.81) than Night-Class ENE 1.

The Coplot of Night-Class ENE 3 was not compiled, because the range of φ_{shear} was too small. Hence, the correlation of $u_{17\text{ m}}$ and $u_{0.1\text{ m}}$ was evaluated without classification. This analysis revealed a high correlation with a significant τ_R of 0.57 (Fig. B.6). Besides this, the range of $u_{17\text{ m}}$ was the highest of all categories ranging from 3.6 ms^{-1} to 8.2 ms^{-1} .

4.2.2 Correlation between wind velocities and momentum exchange

The $u_{0.1}$ - $u_{17\text{ m}}$ -plot was compared with a plot of $u_{0.1\text{ m}}$ and the friction velocity $u_{0.1\text{ m}}^*$ as a measure of momentum exchange for all night-classes (Fig. 4.5). For Night-Class W no correlation between the wind velocities as well as between $u_{0.1\text{ m}}$ and $u_{0.1\text{ m}}^*$ was found (yellow triangles, Fig. 4.5). Moreover, $u_{0.1\text{ m}}$ maintained $< 0.4\text{ ms}^{-1}$, even for high $u_{17\text{ m}}$ and $u_{0.1\text{ m}}^*$. In contrast, the correlation between $u_{0.1\text{ m}}$ and $u_{17\text{ m}}$ was high for the other three night-classes. Moreover, Night-Class ENE 3 revealed the same relation between $u_{0.1}$ and $u_{17\text{ m}}$ as Night-Class ENE 1 and 2, even though the range of both parameters was much higher. Besides, Night-Classes ENE 1-3 showed a linear dependency between the wind velocities as well as between $u_{0.1\text{ m}}$ and $u_{0.1\text{ m}}^*$, besides two exceptions. For Night-Class ENE 2 and Night-Class ENE 1 some $u_{0.1\text{ m}}$ were $< 0.4\text{ ms}^{-1}$, whereas $u_{17\text{ m}}$ and $u_{0.1\text{ m}}^*$ had both high values. Another exception was a strong correlation between $u_{0.1\text{ m}}$

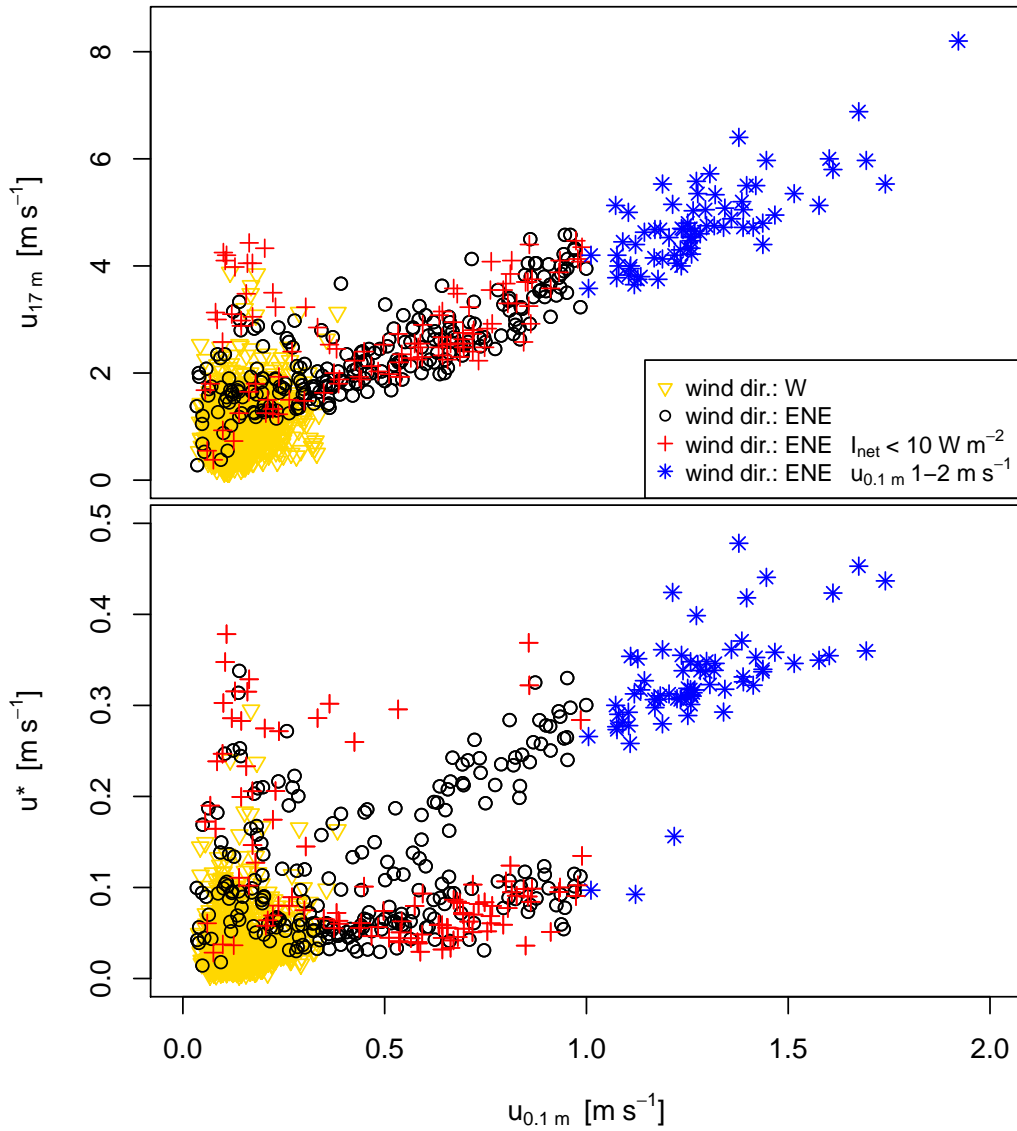


FIGURE 4.5: Correlation between wind velocities in 0.1 m and 17 m ($u_{0.1 m}$ and $u_{17 m}$) and between wind and friction velocity in 0.1 m ($u_{0.1 m}^*$) for all four night-classes. yellow triangles: Night-Class W; black circles: Night-Class ENE 1; red crosses: Night-Class ENE 2; blue stars: Night-Class ENE 3.

and $u_{17 m}$ in combination with $u_{0.1 m}^* < 0.1 \text{ ms}^{-1}$. In summary the combination of $u_{0.1 m}$, $u_{17 m}$ and $u_{0.1 m}^*$ revealed three cases: First, a linear dependency between all three values, second, some small $u_{0.1 m}$ in combination with high $u_{17 m}$ and $u_{0.1 m}^*$, and third, a linear dependency between $u_{0.1 m}$ and $u_{17 m}$ independent from $u_{0.1 m}^*$.

4.2.3 Prevailing wind directions in 17 m

Only two night-classes with $\varphi_{0.1 m} W$ were found. These night-classes showed wind directions along the full range of $\varphi_{17 m}$, but almost all $u_{17 m}$ were $< 2 \text{ ms}^{-1}$ and most points were

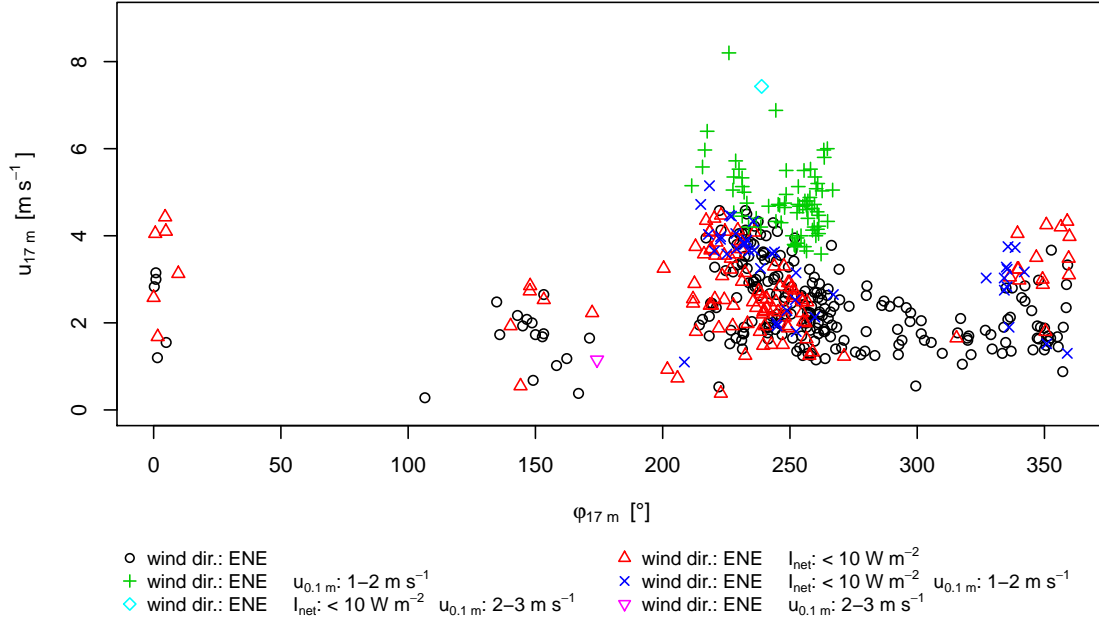


FIGURE 4.6: Wind direction and velocity in 17 m height ($\varphi_{17\text{ m}}$ and $u_{17\text{ m}}$) for each Night-Class with wind direction ENE in 0.1 m height. Night-classes denoted by different symbols and colors according to legend.

encountered with $\varphi_{17\text{ m}}$ from 130° to 180° , i.e. SSE and S (Fig. B.7). The median of $u_{17\text{ m}}$ was $1.0 \pm 0.5\text{ m s}^{-1}$. Accordingly, $u_{17\text{ m}}$ was small for both night-classes and did not vary much.

Seven different night-classes with $\varphi_{0.1\text{ m}}$ ENE were found. Most data points were encountered with $\varphi_{17\text{ m}}$ from 220° to 270° , i.e. WSW and W, corresponding to a high φ_{shear} of these night-classes. Moreover, Night-Class ENE 3 revealed only values within this interval of $\varphi_{17\text{ m}}$. Additionally, the highest $u_{17\text{ m}}$ were found there. Other values of φ_{shear} were rather small patches with $u_{17\text{ m}} < 4\text{ m s}^{-1}$. Besides, $u_{17\text{ m}}$ had a big range from $\approx 1\text{ m s}^{-1}$ to 8.5 m s^{-1} . The median of $u_{17\text{ m}}$ was $2.8 \pm 1.6\text{ m s}^{-1}$ in contrast to the night-classes with $\varphi_{0.1\text{ m}}$ W.

4.3 Spatial temperature distribution

4.3.1 Horizontal and vertical perturbation of temperature

In common, the mean horizontal perturbation of temperature $\mu_{\theta_{horiz}^*}$ was mainly different between Night-Class W and Night-Class ENE 1-3 (Fig. 4.7 a and b-d).

Night-Class W revealed the highest $\mu_{\theta_{horiz}^*}$ ranging from -3.2 K to 3.4 K (Fig. 4.7 a). Further, values of $\mu_{\theta_{horiz}^*}$ were horizontally most different and revealed the highest values in 5 cm height. The Open Stand revealed positive $\mu_{\theta_{horiz}^*}$ up to $> 1.0\text{ K}$. The Upper Meadow was two-parted with a warmer region ($\mu_{\theta_{horiz}^*}$ up to 1 K) from distance 41 m to 65 m near the domain Open Stand. The second part was a colder region with $\mu_{\theta_{horiz}^*}$ even $< -1.5\text{ K}$

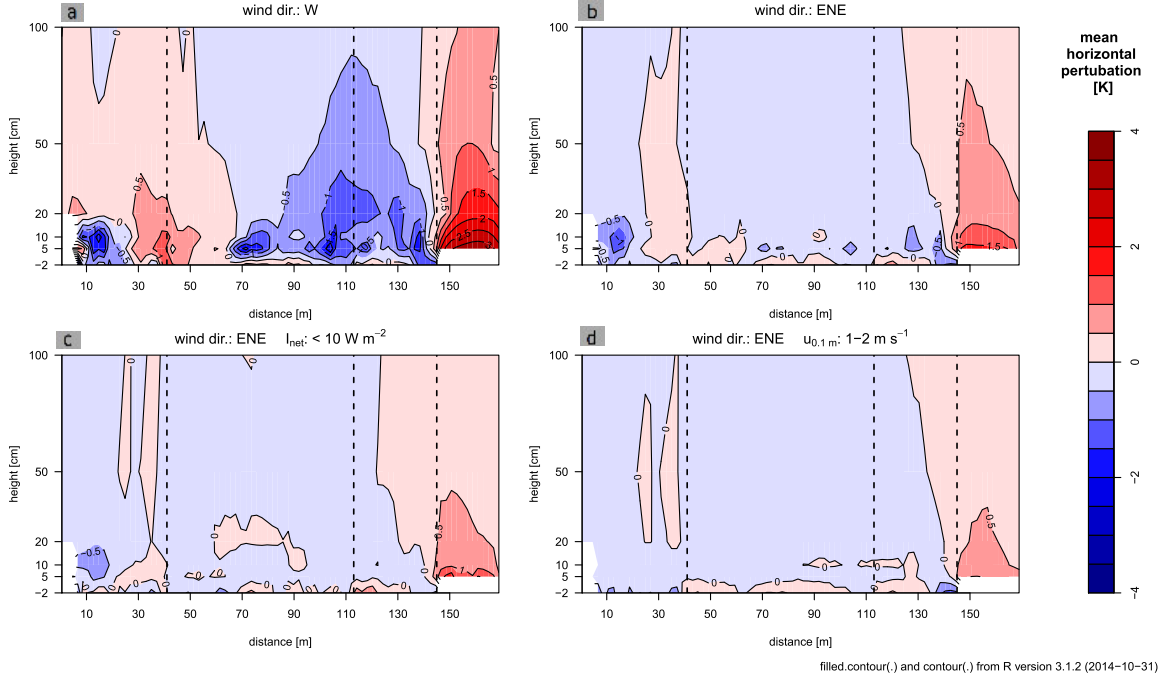


FIGURE 4.7: Mean horizontal perturbation of temperature $\mu_{\theta_{horiz}}^*$ of the fiber-optic array for all four night-class. a: Night-Class W; b: Night-Class ENE 1; c: Night-Class ENE 2; d: Night-Class ENE 3; dashed vertical lines: border of domains

at the lower end of this domain (distance 65 m to 113 m). The coldest region was the domain Lower Meadow with $\mu_{\theta_{horiz}}^* < -1.5$ K and even < 0 K for all heights. At the end of the Upper Meadow and above the Lower Meadow the $\mu_{\theta_{horiz}}^*$ kept low up to a height of 20 cm. At distance 140 m the cold region of the Lower Meadow got warmer in approach to the Lake. Further, the Lake was the warmest region with the maximum $\mu_{\theta_{horiz}}^*$ of 3.4 K. The strength of $\mu_{\theta_{horiz}}^*$ got vertically smaller with increasing height, but warmer and colder regions were nevertheless observed. Besides, the Open Stand also contained a small cold patch from distance 5 m to 30 m up to a height of 20 cm with $\mu_{\theta_{horiz}}^*$ up to < -1.5 K, in contrast to the predominant positive values of $\mu_{\theta_{horiz}}^*$.

Night-Class ENE 1 showed small $\mu_{\theta_{horiz}}^*$ ranging from -1.5 K to 1.7 K (Fig. 4.7 b). In addition, $\mu_{\theta_{horiz}}^*$ was vertically almost homogeneous. Nevertheless, the warmest region was found above the Lake ($\mu_{\theta_{horiz}}^* > 1.5$ K in 5 cm). The Open Stand was horizontally two-parted with $\mu_{\theta_{horiz}}^*$ from -0.5 K to 0.0 K until distance 20 m for all heights and the second half with $\mu_{\theta_{horiz}}^*$ 0.0-0.5 K for all heights. A small cold patch like for Night-Class W was visible with $\mu_{\theta_{horiz}}^*$ up to < -1.0 K. The Upper Meadow was horizontally and vertically almost the same with $\mu_{\theta_{horiz}}^*$ mainly 0.0 K to -0.5 K. This domain also showed some colder patches in 5 cm height with $\mu_{\theta_{horiz}}^* < -0.5$ K, but those were rather small. The Lower Meadow was likewise with the same $\mu_{\theta_{horiz}}^*$, but vertically different. From distance 140 m $\mu_{\theta_{horiz}}^*$ in 5 cm was < -0.5 K, while in 100 cm $\mu_{\theta_{horiz}}^* > 0.0$ K and this was already revealed for distance 125 m. Moreover, the same $\mu_{\theta_{horiz}}^*$ -values could be found above the Lake. Accordingly, the warm patch above the Lake reached into the Lower Meadow. This was more intense in 100 cm than in 5 cm. Night-Class ENE 2 and Night-Class ENE 3 had even smaller ranges of $\mu_{\theta_{horiz}}^*$ (-1.1 K to 1.9 K and -1.2 to 1.0 K, respectively) and the domains showed even less differences

(Fig. 4.7 c and d). Nevertheless, the slightly higher $\mu_{\theta^*_{horiz}}$ in the second half of the Open Stand were found for Night-Class ENE 2 and 3 as well, but this warm patch was spatially smaller for both night-classes. Moreover, this patch only existed for heights 20 cm to 100 cm for Night-Class ENE 3. Both night-classes revealed the same patch with higher $\mu_{\theta^*_{horiz}}$ above the Lower Meadow as Night-Class ENE 1. Accordingly, also for Night-Class ENE 2 and 3 the warm patch of the Lake reached into the Lower Meadow. Besides, the Lake remained the warmest region with $\mu_{\theta^*_{horiz}} > 1.5$ K and > 1.0 K, respectively. The other regions had mainly $\mu_{\theta^*_{horiz}}$ from 0.0 K to -0.5 K and were homogeneous, i.e. revealed almost no temperature perturbation.

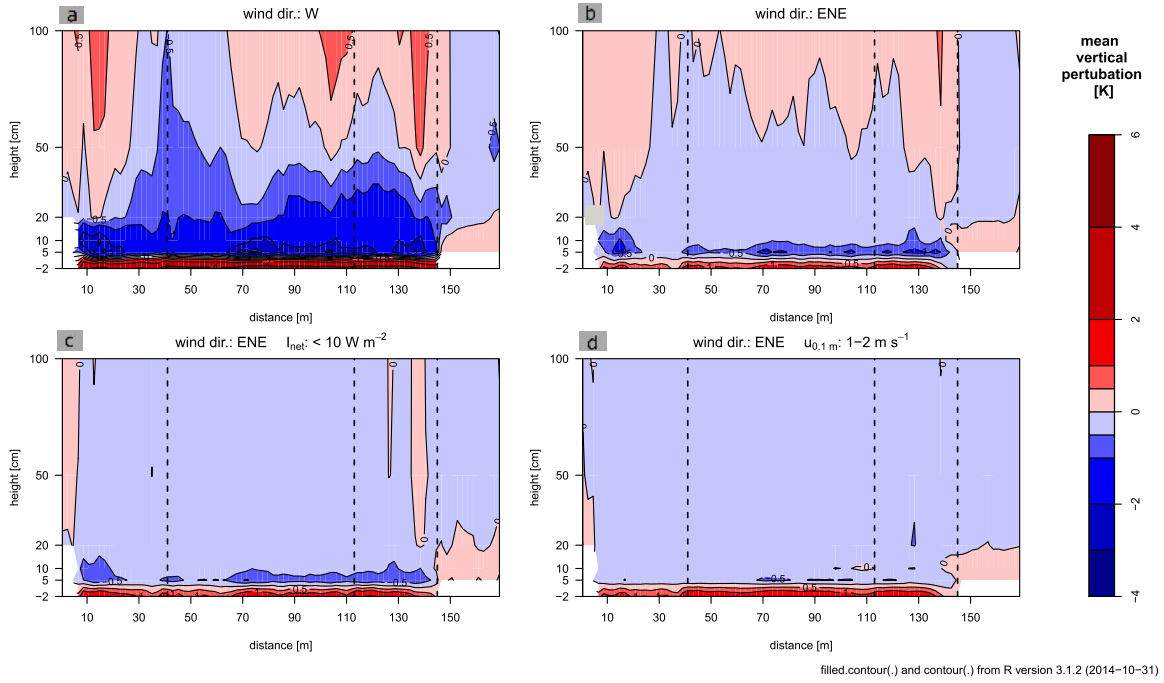


FIGURE 4.8: Mean vertical perturbation of temperature $\mu_{\theta^*_{verti}}$ of the fiber-optic array for all four night-classes. a: Night-Class W; b: Night-Class ENE 1; c: Night-Class ENE 2; d: Night-Class ENE 3; dashed vertical lines: border of domains

Night-Class W revealed the highest vertical perturbation along the transect, while the other night-classes had only quite small $\mu_{\theta^*_{verti}}$ (Fig. 4.8 a and b-d). Besides, $\mu_{\theta^*_{verti}}$ was horizontally homogeneously distributed all along the slope, but the values of $\mu_{\theta^*_{verti}}$ was different for each night-class. Only above the Lake all night-classes were comparable with a $\mu_{\theta^*_{verti}}$ from 0.5 K to 0.0 K for heights < 20 cm and a $\mu_{\theta^*_{verti}}$ from -0.5 K to 0.0 K for heights > 20 cm. Night-Class W had the highest range of $\mu_{\theta^*_{verti}}$ from -3.8 K to 5.5 K (Fig. 4.8 a). The distribution of $\mu_{\theta^*_{verti}}$ was horizontally homogeneous, because $\mu_{\theta^*_{verti}} < -1.0$ K for the lowest 20 cm for all domains. Besides, the lowest $\mu_{\theta^*_{verti}}$ were found in 5 cm at the lower end of the Upper Meadow and above the Lower Meadow (distance 65 m to 140 m) and in the first half of the Open Stand. In general, the lowest $\mu_{\theta^*_{verti}}$ were near the ground and got higher with increasing height with a temperature gradient above ground of ≈ 3 K m^{-1} for all domains with exception of the Lake and distance 28 m to 70 m. Above the Lake, $\mu_{\theta^*_{verti}}$ was slightly higher directly above the lake than for heights > 20 cm. Therefore, a temperature gradient of ≈ -1 K m^{-1} was found there. Besides, from distance 28 m to 70 m $\mu_{\theta^*_{verti}}$ above the

ground was mainly -0.5 K, in contrast to the other domains with $\mu_{\theta_{verti}^*} > 0.5$ K in 100 cm. Accordingly, the temperature gradient was only ≈ 1.5 Km⁻¹ in this region and $\mu_{\theta_{verti}^*}$ was more homogeneous than in the other regions. Besides, the maximum $\mu_{\theta_{verti}^*}$ (> 5.0 K) was found in -2 cm for all domains.

Night-Class ENE 1 had a smaller range of $\mu_{\theta_{verti}^*}$ (-1.3 K–1.8 K) and was horizontally almost homogeneously distributed (Fig. 4.8 b). Only a thin layer with $\mu_{\theta_{verti}^*} < -0.5$ K established in 5 cm height. Above this layer $\mu_{\theta_{verti}^*}$ was mainly between -0.5 K and 0.0 K for heights < 50 cm and between 0.0 K and 0.5 K for even higher heights. The thin cold-air layer only existed up to a distance of 140 m and then $\mu_{\theta_{verti}^*}$ increased with increasing distance. Above the Lake $\mu_{\theta_{verti}^*}$ was quite homogeneous, but inverted with $\mu_{\theta_{verti}^*}$ 0.0-0.5 K for heights < 20 cm and $\mu_{\theta_{verti}^*}$ -0.5-0.0 K for heights > 20 cm.

Night-Class ENE 2 also revealed this small cold-air layer, but $\mu_{\theta_{verti}^*}$ was even less intense (Fig. 4.8 c). So the air above this layer had homogeneously a $\mu_{\theta_{verti}^*}$ of -0.5–0.0 K with exception of the Lake, which was as described for Night-Class ENE 1 above.

Finally, Night-Class ENE 3 had the smallest range of $\mu_{\theta_{verti}^*}$ (-0.6 K to 1.9 K) and only $\mu_{\theta_{verti}^*}$ between -0.5 K and 0.0 K for almost all domains (Fig. 4.8 d). Accordingly, Night-Class ENE 3 showed no vertical temperature perturbation above the ground. Only the air in direct contact with the Lake revealed higher $\mu_{\theta_{verti}^*}$.

4.3.2 Determination of cold-air pools

The CPI and θ_{top}^* was mainly different between Night-Class W and all other night-classes with $\varphi_{0.1 m}$ ENE. Night-class W had a CPI of 1.2 K and a θ_{top}^* of 0.4 K. In contrast, Night-Class ENE 1-3 had a CPI and a θ_{top}^* of 0 K or even slightly negative.

4.3.3 Terrain classification for frost risk

The terrain-classification for frost risk is only presented for Night-Class W, because the Night-Class ENE 1-3 showed only $P_{frost\ risk} < 20\%$ for all domains. The terrain-classification of the most appearing Night-Class W with highest radiative cooling revealed that especially the Upper and Lower Meadow up to a height of 20 cm had a high frost risk ($P_{frost\ risk} > 50\%$). In contrast, the height -2 cm had about no frost risk ($P_{frost\ risk} < 10\%$) all along the slope. Also above the Lake were only low probabilities for frost risk ($P_{frost\ risk} < 30\%$). Another area with lower frost risk were the Open Stand with a more dense vegetation (distance 30 m to 40 m) with $P_{frost\ risk} < 40\%$ for all heights.

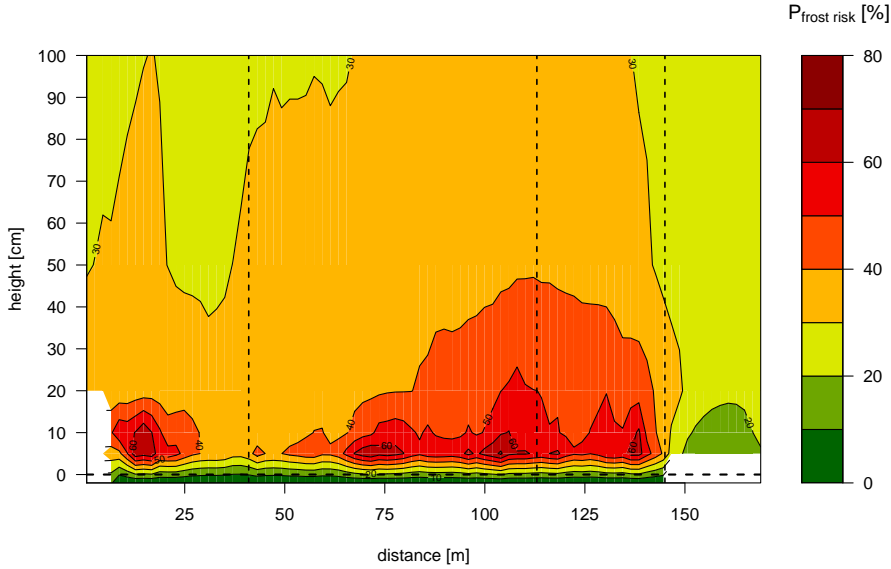


FIGURE 4.9: Terrain classification for frost risk for Night-Class W. Green: no frost risk; Red: strong probability for frost events.

4.4 Case studies

4.4.1 Physical description

Case Study 1 (Night-Class W) had the biggest temperature range from $-7\text{ }^{\circ}\text{C}$ to $+10\text{ }^{\circ}\text{C}$ and the temperatures within the domains was different (Fig. 4.10 a). Since 9 PM a temperature decrease from the top (distance 0 m) to the bottom of the slope (distance 135 m) was observed, i.e. from the Open Stand to the Lower Meadow. The temperature difference between the Open Stand and the Lower Meadow was $\approx 1\text{ K}$ and $\approx 3\text{ K}$ between the Lower Meadow and the Lake. The wind velocities $u_{0.1\text{ m}}$ and $u_{17\text{ m}}$ had the smallest range of all case studies from $0\text{-}0.3\text{ ms}^{-1}$ and $0\text{-}2.0\text{ ms}^{-1}$, respectively. Additionally, the course of both were independent from each other and the friction velocity $u_{0.1\text{ m}}^*$ with a median of 0.02 ms^{-1} was the smallest of all case studies (Fig. 4.10 b). The wind direction in 0.1 m $\varphi_{0.1\text{ m}}$ was constantly West all night, whereas the wind direction in 17 m was constantly between S and ESE at first at 09.30 PM (Fig. 4.10 c). At the same time the temperature difference between bottom and top of slope became slightly more intense. Besides, this Case Study had the highest positive longwave radiation balance I_{net} with a median of 63.4 Wm^{-2} . During the whole night the Lower Meadow was the coldest domain, but from distance 135 m to 150 m, i.e. in approach to the lake, the temperature became 1-2 K higher.

In contrast, the temperatures of Case Study 2 (Night-Class ENE 1) were coherent and isotherm along the slope. Only the domain Lake was $\approx 1\text{ K}$ warmer than the other domains and not until 01:30 AM the temperature got lower (Fig. 4.11 a). The full temperature range was small from $0\text{ }^{\circ}\text{C}$ to $7\text{ }^{\circ}\text{C}$ and the median of I_{net} (21.9 Wm^{-2}) was low. Besides, the ranges of wind velocities were higher and the course of $u_{17\text{ m}}$ and $u_{0.1\text{ m}}$ identical (Fig. 4.11 b). At 01:30 AM, simultaneously with the temperature decrease, the wind velocities decreased and

$u_{17\ m}$ and $u_{0.1\ m}$ kept mainly below $1.5\ \text{ms}^{-1}$ and $0.4\ \text{ms}^{-1}$, respectively. Additionally, the friction velocity $u^*_{0.1\ m}$ was higher with a median of $0.06\ \text{ms}^{-1}$. Besides, $\varphi_{17\ m}$ was constantly W or WSW, while $\varphi_{0.1\ m}$ was the opposite direction between E and ENE until 02:40 AM (Fig. 4.11 c). After 02:40 AM $\varphi_{0.1\ m}$ was more variant, simultaneously with lower temperatures and lower wind velocities. Further, from distance 140 m to 150 m, i.e. in approach to the lake, there was only a small temperature increase of less than 1 K all night long.

For Case Study 3 (Night-Class ENE 1-3) the temperatures did not differ between domains and cooling started already at about 10 PM (Fig. 4.12 a). The wind velocities were even higher ($u_{17\ m}$: $0\text{-}5.0\ \text{ms}^{-1}$ and $u_{0.1\ m}$: $0\text{-}1.2\ \text{ms}^{-1}$) as well as $u^*_{0.1\ m}$ with $0.09\ \text{ms}^{-1}$ (Fig. 4.12 b). A simultaneous decrease of temperatures and wind velocities could be studied as well. The wind directions were quite constant with $\varphi_{17\ m}$ mainly WSW and $\varphi_{0.1\ m}$ mainly ENE (Fig. 4.12 c). Besides, I_{net} was low with a median of $21.1\ \text{Wm}^{-2}$. Further, the same behavior of increasing temperatures near the lake could be observed.

Finally, Case Study 4 (Night-Class ENE 1 and Night-Class W (variantly)) was a mixture of Case Study 1 and 3. Again, a temperature decrease was ascertained simultaneously with a decrease in temperature (Fig. 4.13 a and b). I_{net} was higher with a median of $34.3\ \text{Wm}^{-2}$, but even only half of the median I_{net} of Case Study 1. If $\varphi_{0.1\ m}$ was mainly ENE, $\varphi_{17\ m}$ was mainly NNW at 08:40 PM–11:50 PM and around 02:00 AM (Fig. 4.13 c). During these periods the temperatures were isotherm along the transect, only with the Lake being about 1 K warmer. In contrast, if $\varphi_{0.1\ m}$ was mainly W (07:10 PM–07:50 PM, 11:50 PM–01:30 AM and 02:50 AM–03:20 AM), $\varphi_{17\ m}$ was inconsistent and a temperature distribution along the transect emerged. In this case the Lower Meadow was the coldest patch and, in comparison, the Lake was about 2 K warmer, but no difference between the temperatures of Open Stand and of the Upper Meadow could be evaluated.

4.4.2 MRD: Spatial coherence of temperature development

For all case studies, the two-point correlation coefficient R_{ij} of the MRD decreased with increasing separation distance. Only for the 64-min time scale no decreasing R_{ij} for all separation distances was detected. This decrease, i.e. decorrelation, was faster for smaller time scales. Accordingly, the temperature development was only for a time scale of 64 min spatially the same. Besides, the Open Stand revealed the same decorrelation of R_{ij} as the Upper and Lower Meadow of each case study and is therefore not described. Further, the added lines in Fig. 4.14 show the smoothed course of R_{ij} with increasing separation distance.

Case Study 1 (Night-Class W) had the fastest decreasing R_{ij} with increasing separation distance on all time scales smaller than 32 min (Fig. 4.14 a). Even for a time scale of 16 min the decorrelation was fast. Accordingly, the temperature courses were spatially highly different for these time scale. Besides, the decorrelation of time scales 8 min, 4 min and 2 min were the same above the Upper and especially the Lower Meadow. However, above the Lake the R_{ij} stopped decreasing or even increased for all time-scales. Further, R_{ij} of all time scales smaller 16 min were about the same above the Lake.

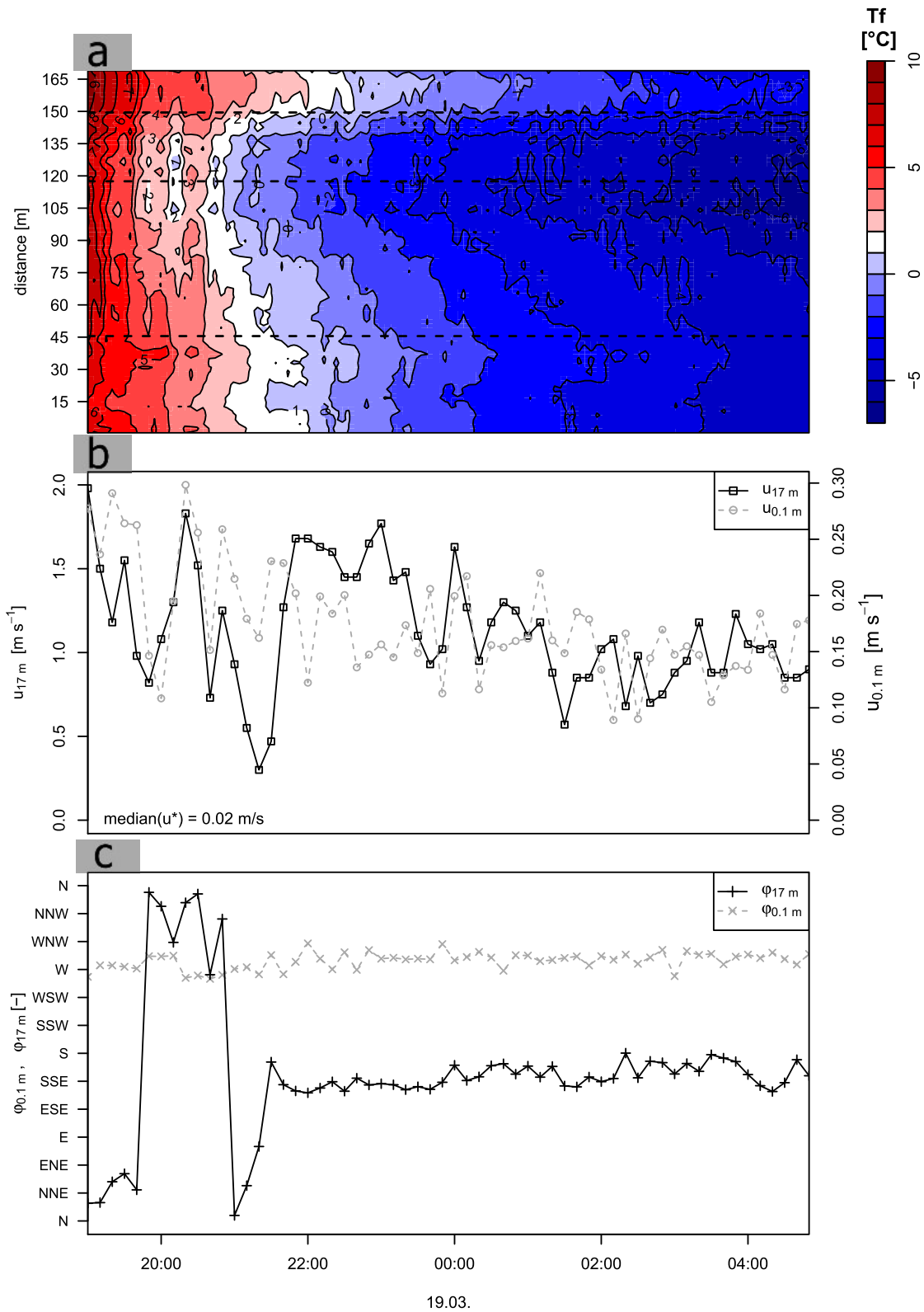


FIGURE 4.10: Physical description of Case Study 1. a: fiber temperature T_f in 20 cm along the slope dependent on distance to Point A with domains as dashed horizontal lines; b: wind velocities $u_{17\text{ m}}$ and $u_{0.1\text{ m}}$ and median of friction velocity for shown time period ' $\text{median}(u^*_{0.1\text{ m}})$ '; c: wind directions $\varphi_{17\text{ m}}$ and $\varphi_{0.1\text{ m}}$.

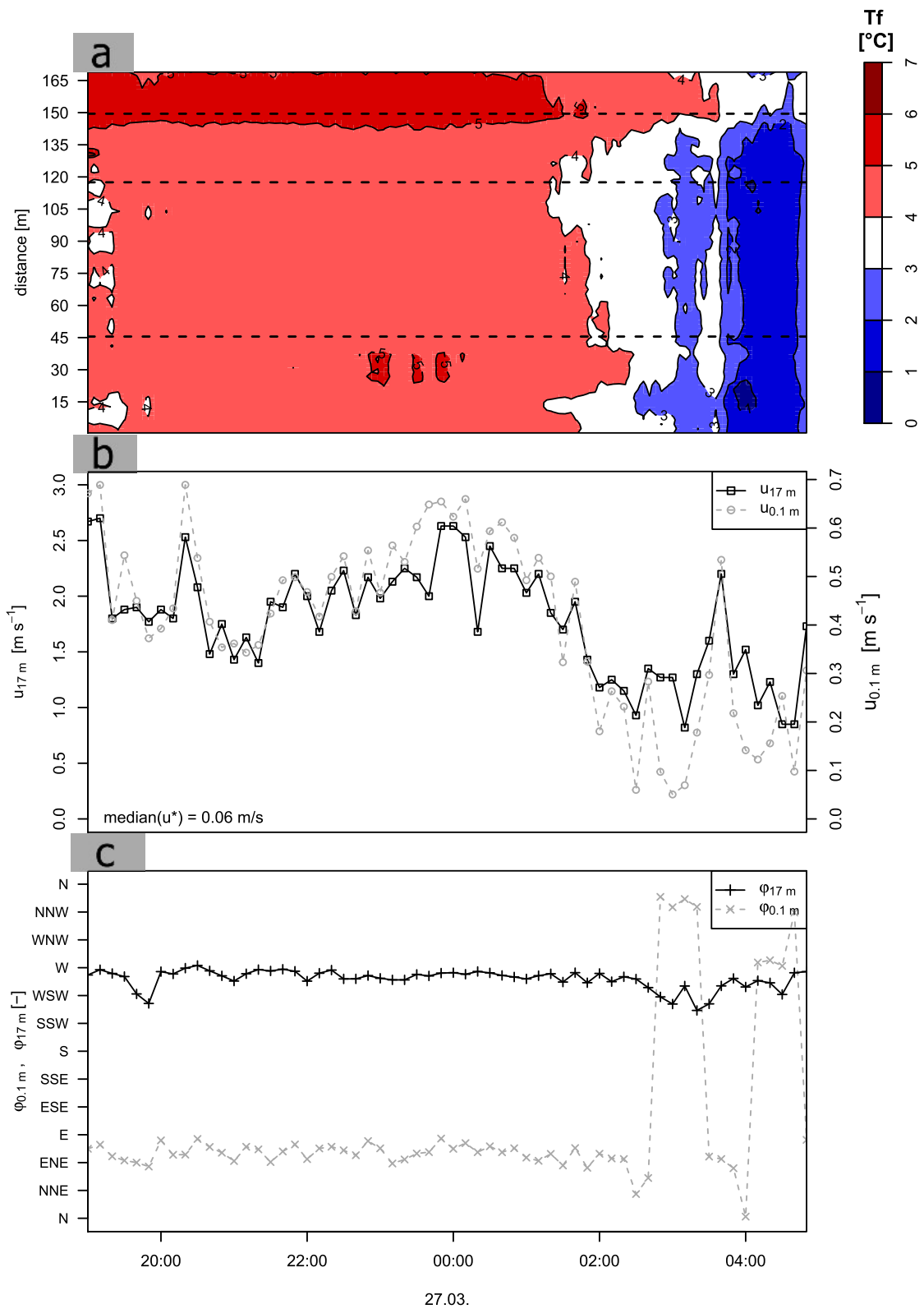


FIGURE 4.11: Physical description of Case Study 2. a: fiber temperature T_f in 20 cm along the slope dependent on distance to Point A with domains as dashed horizontal lines; b: wind velocities $u_{17\text{ m}}$ and $u_{0.1\text{ m}}$ and median of friction velocity for shown time period ' $\text{median}(u^*_{0.1\text{ m}})$ '; c: wind directions $\varphi_{17\text{ m}}$ and $\varphi_{0.1\text{ m}}$.

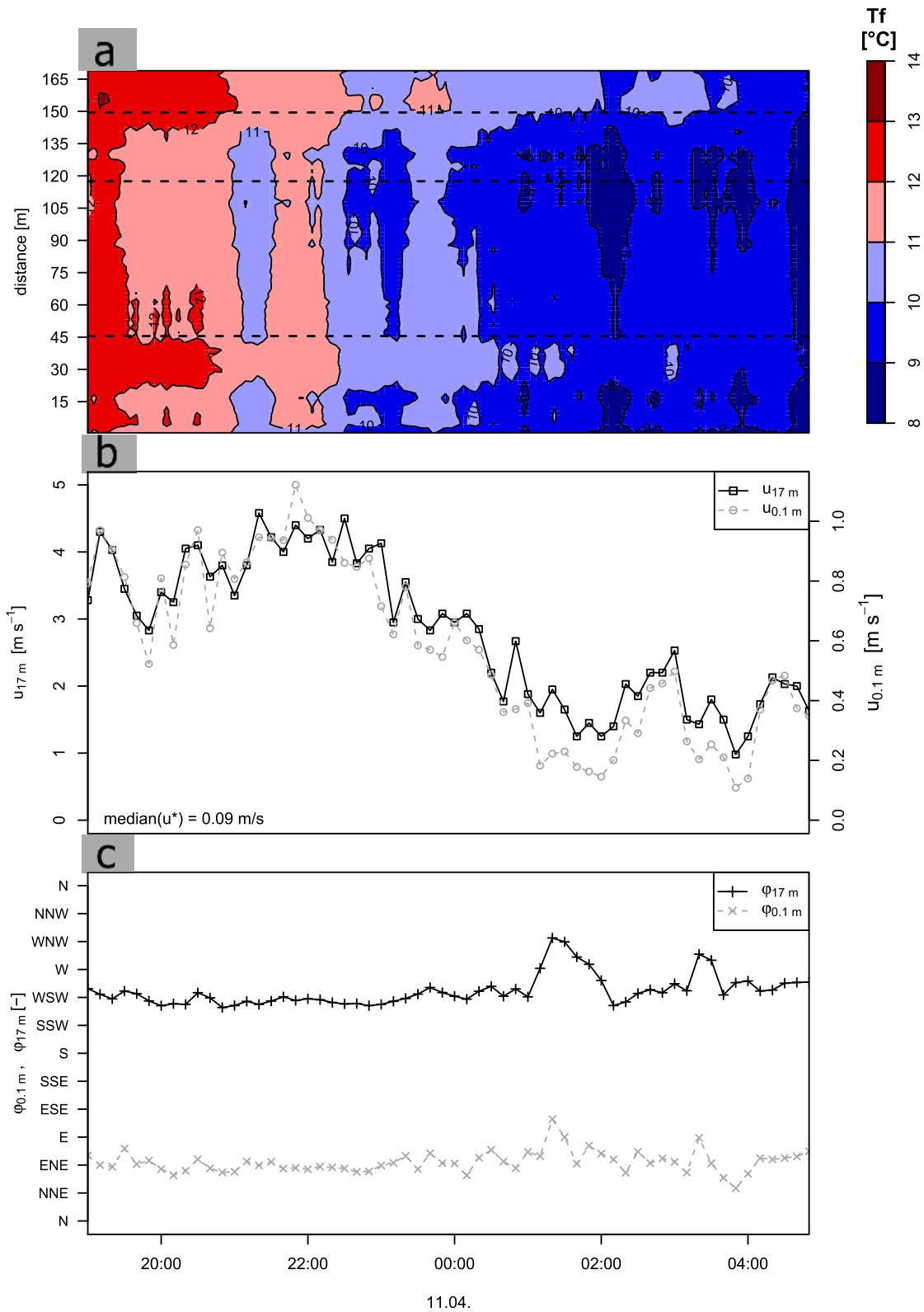


FIGURE 4.12: Physical description of Case Study 3. a: fiber temperature T_f in 20 cm along the slope dependent on distance to Point A with domains as dashed horizontal lines; b: wind velocities $u_{17\text{ m}}$ and $u_{0.1\text{ m}}$ and median of friction velocity for shown time period 'median($u^*_{0.1\text{ m}}$)'; c: wind directions $\varphi_{17\text{ m}}$ and $\varphi_{0.1\text{ m}}$.

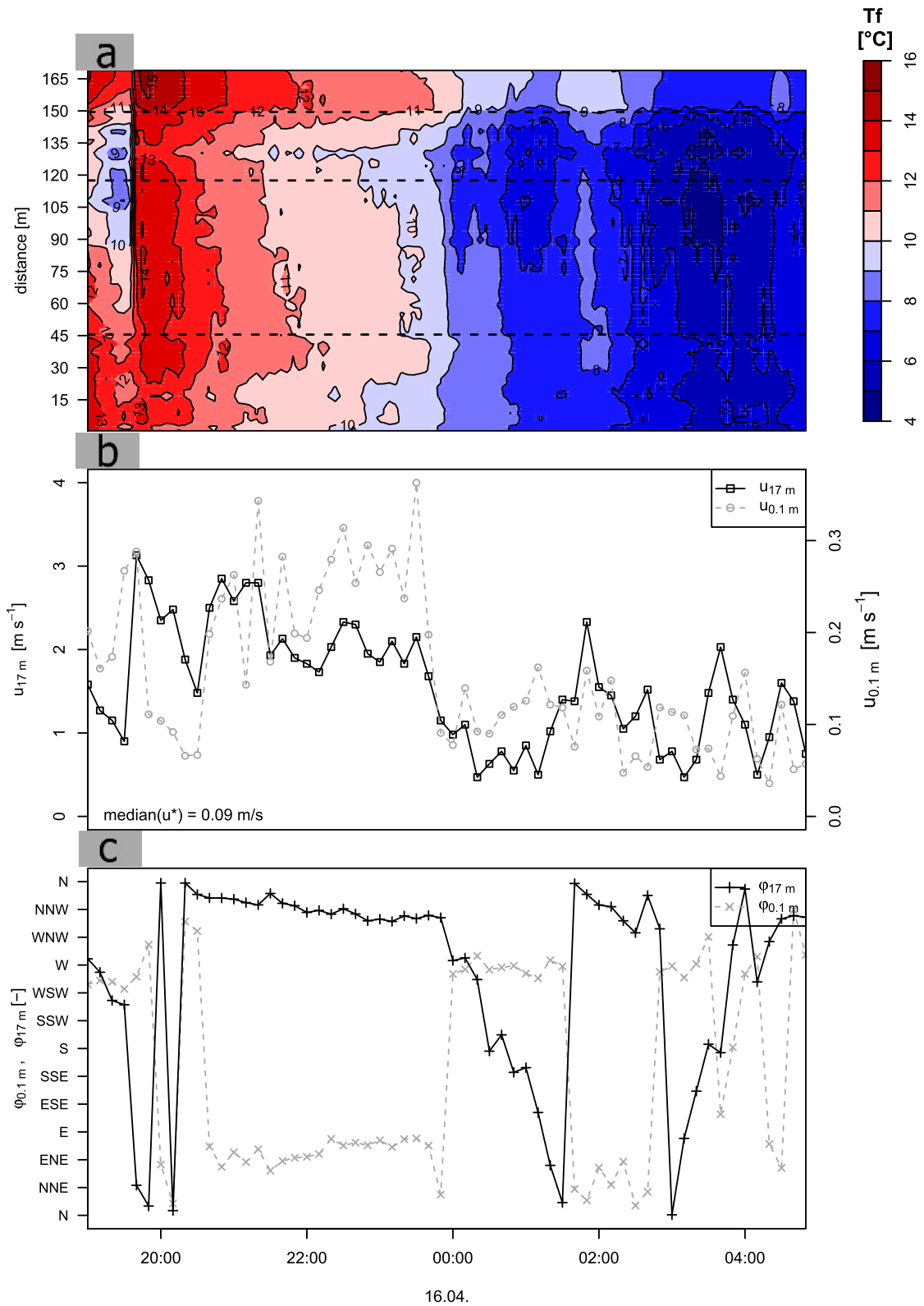


FIGURE 4.13: Physical description of Case Study 4. a: fiber temperature T_f in 20 cm along the slope dependent on distance to Point A with domains as dashed horizontal lines; b: wind velocities $u_{17\text{ m}}$ and $u_{0.1\text{ m}}$ and median of friction velocity for shown time period $\text{median}(u^*_{0.1\text{ m}})$; c: wind directions $\varphi_{17\text{ m}}$ and $\varphi_{0.1\text{ m}}$.

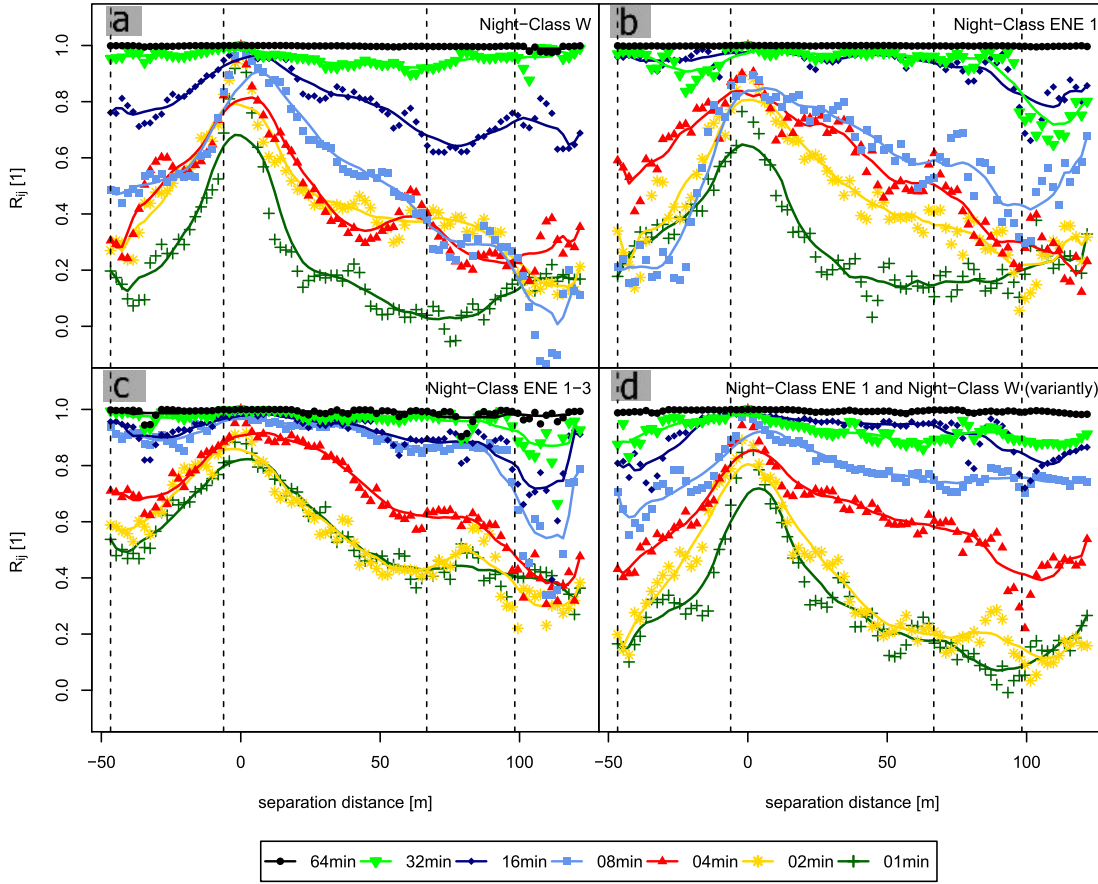


FIGURE 4.14: MRD: Spatial coherence of temperature development in 5 cm along the transect. Spatial coherence is displayed as two-point correlation coefficient (R_{ij}) for seven different time scales of the MRD for all four case studies. R_{ij} plotted against separation distance of Point i and Point j . a: Case Study 1 (Night-Class W); b: Case Study 2 (Night-Class ENE 1); c: Case Study 3 (Night-Class ENE 1-3); d: Case Study 4 (Night-Class ENE 1 and Night-Class W (variably)); vertical lines: domains.

For Case Study 2 (Night-Class ENE 1) the decrease of R_{ij} was smaller, with increasing separation distance (Fig. 4.14 b). Almost no decorrelation was observed for longer time scales (64 min, 32 min and 16 min) and for all separation distances with exception of those at the Lake. Further, R_{ij} decreased fast for all time scales smaller 16 min and this decorrelation was even faster for smaller time scales. Above the Lake and in approach to the Lake, the decrease of R_{ij} got bigger with increasing separation distance and the minimum R_{ij} of all time scales was found above the Lake.

Case Study 3 (Night-Class ENE 1-3) was comparable to Case Study 2, but had the slowest decorrelating R_{ij} on all time scales (Fig. 4.14 c). Even the smallest time scale did not drop below 0.4. Further, all time scales smaller 8 min had almost no decorrelation, whereas the 2-min and 1-min time scale could not be differentiated and had the fastest decorrelation. However, this was not the case above the Lake. Above the Lake and even in approach to the Lake the R_{ij} of all time scales, with exception of the two smallest, decreased very fast with increasing separation distance and all time scales revealed their minimum above the Lake.

Case Study 4 (Night-Class ENE 1 and Night-Class W (variantly)) was comparable to Case Study 3, but with faster decreasing R_{ij} and the high decrease of R_{ij} above the Lake was less obvious (Fig. 4.14 d).

4.4.3 Fog Experiment

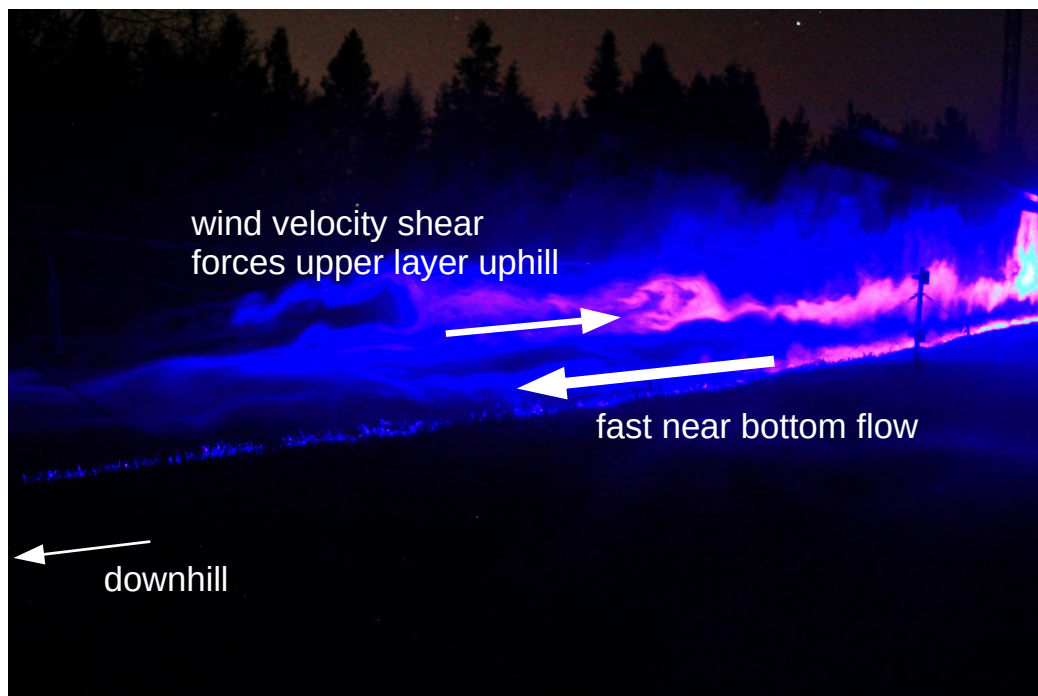


FIGURE 4.15: Event 1: Cold-air flow on top of an existing cold-air layer with direction shear. Airflow is fastest at the bottom and rather turns back at the top.

Three different events of the Fog Experiment were chosen for analysis of the processes. A photo series of 10 photos with a frequency of 1 Hz was taken for each event and is available on the Digital Medium (Appendix C).

Event 1 was a flow on top of an existing cold-air layer forced uphill through wind velocity shear (Fig. 4.15). The slope was directed downhill to the left-hand side of the figure. During this event two layers existed. A thin layer of cold-air near the ground and a deeper layer flowing over the thin layer. The thin layer was rather homogeneous and revealed no shear vertices, whereas the upper layer was more mixed and a shear vortex could be seen in the center of the layer. The wind velocity shear was induced, as the cold-air drainage of the thin layer was faster than the flow above. Therefore the flow of the upper layer was slowed down, became stagnant and finally turned uphill.

Event 2 was also parted into two layers, both with a flow directed uphill (Fig. 4.16). The layer near the ground was thin (≈ 10 cm deep), while the overlaying, much deeper layer (≈ 3 m deep) revealed some big shear vertices. In the picture series the near bottom flow also show small vertices at the visible left-hand end of this flow. Besides, the vertices of the deeper layer vanish and the whole layer slowly flow uphill.

Finally, Event 3 was the blockage of a cold-air flow and convection above the lake (Fig. 4.17).

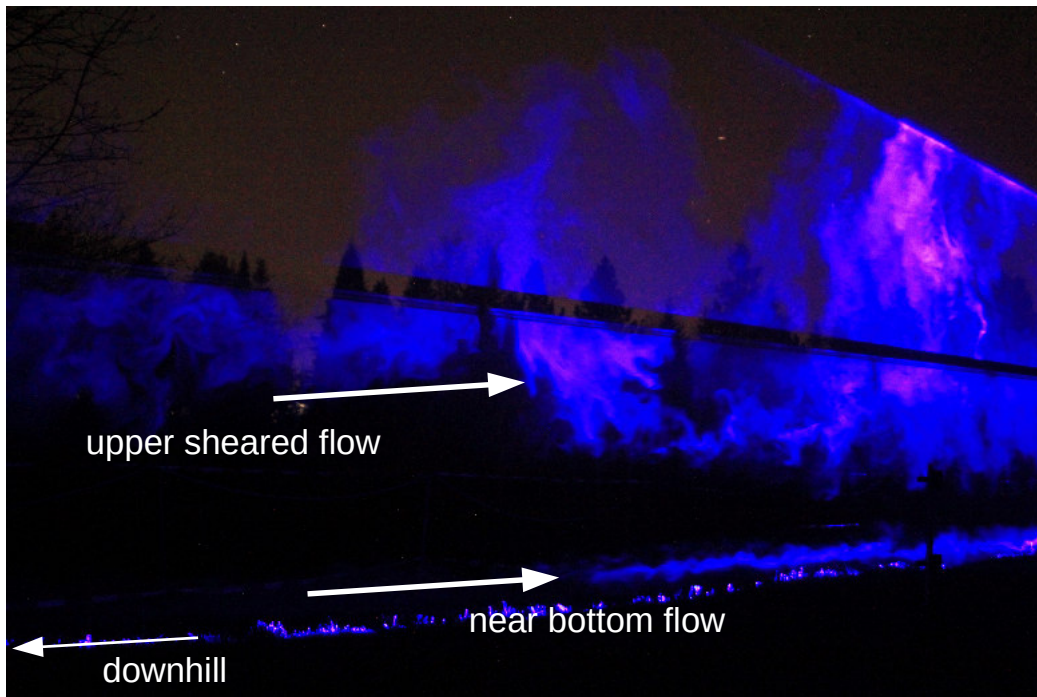


FIGURE 4.16: Event 2: Upslope flow near bottom and in several meter height without direction shear.

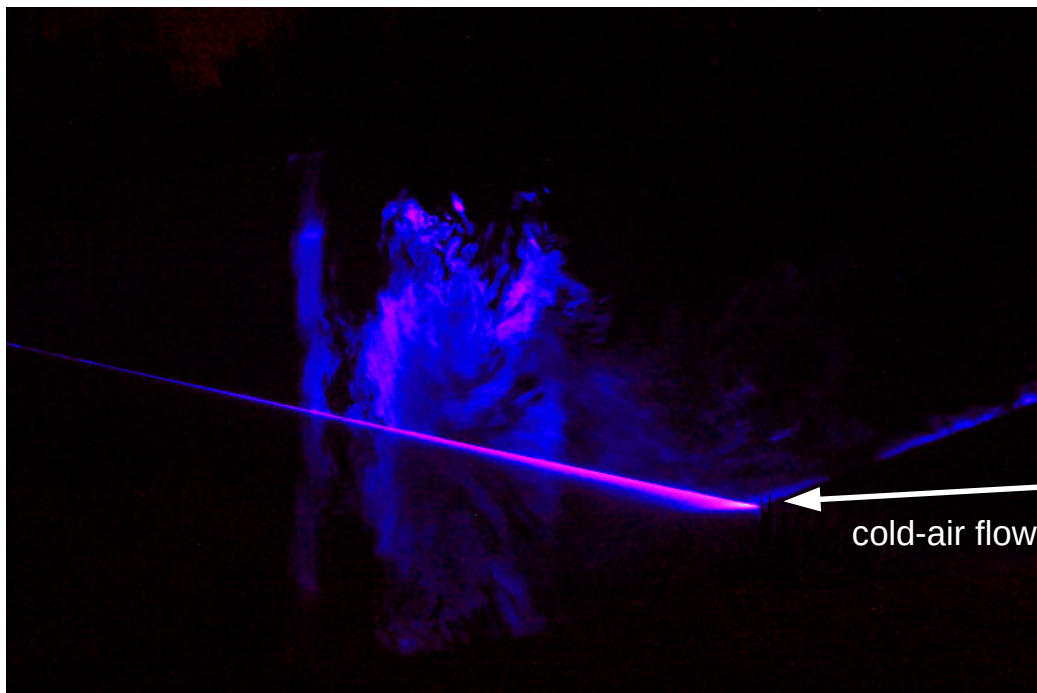


FIGURE 4.17: Event 3: Blockage of cold-air flow and convection above the lake

The lake surface is the bright pink line diagonal from right to the left of the figure. In this figure the white arrow is the direction of the cold-air flow and shows, where the lake surface started. The cold-air flow came from the right-hand side of the picture and drained upon the lake. There the flow immediately slowed down and was stopped after ≈ 4 m. Then the fog was forced upwards, away from the lake surface. But the cold-air drainage maintained and turned the rising fog backward into a dextrorotary vortex as seen in the middle of Fig. 4.17.

5. Discussion

5.1 Validation of DTS-measurements

The difference between T_{Pt100} and T_f was high during day and rather small during night (Fig. 4.1). This might have been due to three factors: the purpose and installation of Pt100, the measurement length of both devices and distance between the devices. The Pt100 was only mounted for determination of the minimum temperature of the day. Accordingly, the sensor was installed without radiation protection shelter and ventilation. Therefore, the Pt100 had a high radiation error due to absorption of shortwave radiation during day. In contrast, the glass fiber had a really small radiation error due to the small surface and the white coat with a high albedo. Consequently, T_{Pt100} and T_f should not be compared during day. Besides, the measurement length of the glass fiber (1 m) was much bigger than the one of the Pt100 (≈ 5 cm). Accordingly, the spatial resolution was different and the heat exchange was higher for the glass fiber. Therefore, the Pt100 was warmer than the glass fiber even during night, explaining the median temperature difference of 0.2 K. Finally, the distance between both measurement devices were about 3 m, which might be another reason for a temperature offset and therefore a temperature difference. Besides, the course of both devices was identical (Fig. 4.1). Therefore, the measurements by the glass fiber were correct and revealed no physical aberration.

Temperature difference between the DTS-measurements at the transect and at the columns were expected, due to the used reinforcement fabric at the columns. The reinforcement fabric could heat up or cool down more effectively than the glass fiber, because of a higher surface of the fabric. Additionally, a temporal offset of cooling and warming might occur, as the reinforcement fabric had a bigger volume than the glass fiber and therefore could store more thermal energy. This reasons led to the described temperature differences, which were in the median quite small (0.3 K column B and -0.1 K column D) and in the range of the modeled temperature difference as described in Sigmund (2015) (unpublished).

The standard deviation of T_f (σ_{T_f}) was high, especially during day (top, Fig. 4.2). Almost every day at least one σ_{T_f} was higher than 1 K, whereas the median of σ_{T_f} was 0.4 K at day and 0.3 K at night. The difference of $\sigma_{u_{0.1m}}$ between day and night was similar, but $\sigma_{u_{0.1m}}$ had a small range (center, Fig. 4.2). During day the median was only 0.27 m s^{-1} and especially low during night (0.07 m s^{-1}) and therefore negligible. Finally, the standard deviation of the wind direction had the highest range from 0.1° to 117.9° (bottom, Fig. 4.2). The median of $\sigma_{\Delta\varphi_{0.1m}}$ was 33.4° during day and 24.8° during night. Accordingly, an averaging period of 10 minutes was applicable for T_f -measurements during night as well as for $u_{0.1m}$, but for wind direction in common and for T_f -measurements during day a smaller averaging period should be chosen in other studies. However, this study was determined to a 10-min averaging period, due to the measurements of the meteorologic tower (station EBG) being stored as 10-min averages.

5.2 Investigation of vertical decoupling

5.2.1 Vertical correlation of wind velocities and directions

Night-Class ENE 1 had perfect conditions for cold-air formation in combination with a near bottom flow aligned with the local slope as defined by inductive analysis. Therefore, this night-class was expected to reveal vertical decoupling, as the studies of Mahrt et al. (2001) and Soler et al. (2002) showed, that cold-air drainage was detected even for strong synoptic flows and wind direction shear. In contrast, the other night-classes should differ in analysis, as they had either a near bottom flow, which was not aligned with the local slope, (Night-Class W) or adverse conditions for cold-air formation (Night-Class ENE 2) or too strong near-bottom flows, which can not originate from this small slope (Night-Class ENE 3).

Surprisingly, Night-Class W with a flow perpendicular to the slope was the most abundant night-class, whereas Night-Class ENE 1 with a flow aligned to the slope revealed only a fraction of the number of measurements of Night-Class W (Fig. 4.3 a and b). This already conflicted the first hypothesis, that cold-air drainage can be predicted by the local topography. The conditions for cold-air formation was given for both night-classes (e.g. Soler et al. 2002, Geiss and Mahrt 2015). Therefore, Night-Class ENE 1 with a topography following near bottom flow was expected to be the most abundant night-class, which instead was Night-Class W. Even the nearby topography and elevations, which can induce propagating modes (Mahrt et al., 2013), showed no reason for this perpendicular flow from West.

Further, Night-Class ENE 1 and 2 were almost identical. They revealed the same range of φ_{shear} and $u_{0.1 m}$, showed both the two patches and a moderate association between both parameters (Fig. 4.3 b and c). This contradicted the second hypothesis, that the inductive analysis was sufficient to identify a night-class with cold-air drainage and pooling. In contrast to Night-Class ENE 1, Night-Class ENE 2 had adverse conditions for cold-air formation and drainage, because of a smaller I_{net} ($< 10 \text{ Wm}^{-2}$) probably caused by clouds. Barr and Orgill (1989) reported dramatically smaller cold-air drainage in a valley during cloudy nights. Accordingly, Night-Class ENE 1 and 2 should differ in the relation between wind velocities and directions, which was at least not the case for $u_{0.1 m}$ and φ_{shear} . However, Night-Class W and Night-Class ENE 3 differed and the similarities between Night-Class ENE 1 and 2 may be just an incidence. Therefore, the relation between other parameters, e.g. $u_{0.1 m}$ and $u_{17 m}$, had to differ between Night-Class ENE 1 and 2, otherwise the second hypothesis had to be rejected.

For further evaluation of the first and second hypothesis and the related vertical decoupling of cold-air drainage, the relation between φ_{shear} and $u_{0.1 m}$ for all night-classes had to be considered and compared. Night-Class W revealed the smallest $u_{0.1 m}$ ($< 0.4 \text{ ms}^{-1}$) and φ_{shear} throughout the entire range and both parameters were not correlated (Fig. 4.3 a). Night-Class W showed here the first indication for vertical decoupling. In contrast, Night-Class ENE 1 and 2 revealed two patches and higher $u_{0.1 m}$ up to 1.0 ms^{-1} (Fig. 4.3 b and d). This two patches were the reason for a moderate correlation ($\tau_R \leq 0.52$) between both parameters, as high φ_{shear} were mainly encountered with $u_{0.1 m} > 0.4 \text{ ms}^{-1}$, whereas only smaller $u_{0.1 m}$ were found for low φ_{shear} ($< 110^\circ$). Further, the patch with low $u_{0.1 m}$ and

φ_{shear} comprised a distinct smaller amount of points, than the other patch. However, even small $u_{0.1\ m}$ throughout the entire range of φ_{shear} were observed. Therefore, high φ_{shear} might be related to vertical coupling for $u_{0.1\ m} > 0.4\ \text{ms}^{-1}$, whereas for smaller $u_{0.1\ m}$ both parameters were vertically decoupled. On the other hand, it was possible, that vertical coupling with low and high φ_{shear} existed (Section 3.2.1). Finally, Night-Class ENE 3 had only $\varphi_{shear} > 150^\circ$ and the highest $u_{0.1\ m}$ of 1.0-2.0 ms^{-1} with no correlation (Fig. 4.3 d). Therefore, Night-Class ENE 3 showed an indication for vertical coupling with high φ_{shear} , as the local slope was too small to accelerate near bottom flows to this high values of $u_{0.1\ m}$. This again conflicted the first hypothesis. Night-Class ENE 1 showed indications for vertical coupling, whereas Night-Class W revealed indications for vertical decoupling. Therefore, it is possible, that Night-Class ENE 1 showed no cold-air drainage, because of the indications for vertical coupling. Instead, Night-Class W showed the vertical decoupling. The first hypothesis could be rejected, as the topography suggested a (vertically decoupled) cold-air drainage down the slope, but instead a near bottom flow perpendicular to the slope was found during nights with high I_{net} . Nevertheless, for determination of vertical coupling the correlation between $u_{0.1\ m}$ and $u_{17\ m}$ was considered for all night-classes.

Besides, a transition from Night-Class ENE 1 to Night-Class ENE 3 was discernible, because the association of high φ_{shear} and high $u_{0.1\ m}$ was predominant for Night-Class ENE 1 and 2, whereas Night-Class ENE 3 only revealed this association. If this transition persisted in other analysis, the inductive analysis of night-classes was not sufficient and the second hypothesis could be rejected as well.

The Coplots set the correlation between the wind velocities $u_{0.1\ m}$ and $u_{17\ m}$ in relation to the quartiles of φ_{shear} . However, this was not computed for Night-Class ENE 3 as the range of φ_{shear} was too small.

Night-Class W revealed no correlation between $u_{0.1\ m}$ and $u_{17\ m}$ for all φ_{shear} -quartiles and $u_{17\ m}$ was mainly $< 2.0\ \text{ms}^{-1}$ (Fig. B.4). Accordingly, Night-Class W revealed vertical decoupling. In contrast, high correlations between $u_{0.1\ m}$ and $u_{17\ m}$ were found for $\varphi_{shear} > 110^\circ$ for Night-Class ENE 1-3 and this comprised at least three-quarter of all values of one night-class (Fig. 4.4, Fig. B.5 and Fig. B.6). Therefore, the indications for vertical coupling with high φ_{shear} were confirmed for all three night-classes. Accordingly, the Night-Class ENE 1-3 were almost identical and the inductive analysis not sufficient.

In summary, Night-Class ENE 1-3 revealed mainly vertical coupling with high φ_{shear} , had a near bottom flow aligned to the slope and high $u_{17\ m}$ -values. This contradicted our hypothesis about cold-air drainage. Mahrt et al. (2001) described shallow drainage flows in a gully during nights with clear skies, which originated independent of the ambient winds and even persisted for wind speeds $> 10\ \text{ms}^{-1}$. If our measured $u_{0.1\ m}$ with $\varphi_{0.1\ m}$ ENE (i.e. Night-Class ENE 1-3) was cold-air drainage, which originated from the local cold-air formation, the parameters $u_{0.1\ m}$, φ_{shear} and $u_{17\ m}$ would have been decoupled. Therefore, the aligned flow down the slope was no cold-air drainage for Night-Class ENE 3 as well as for Night-Class ENE 1 and 2 for $\varphi_{shear} > 110^\circ$.

Further, the study of Soler et al. (2002) reported an elimination of cold-air drainage within a

gully by turbulent entrainment for synoptic flows $\geq 2 \text{ ms}^{-1}$. Therefore, Night-Class ENE 1-3 showed no cold-air drainage as $u_{17 \text{ m}}$ was too high and even was coupled with $u_{0.1 \text{ m}}$ for high φ_{shear} . Therefore, $u_{17 \text{ m}}$ had enough synoptic forcing to eliminate cold-air drainage and establish the vertical coupling with a near bottom flow down the slope. In contrast, Night-Class W revealed only $u_{17 \text{ m}} < 2 \text{ ms}^{-1}$ and no correlation between all three parameters. Therefore, an establishing cold-air drainage or pooling was not eliminated by turbulent entrainment for this night-class.

Nevertheless, for Night-Class ENE 1 and 2 the smallest φ_{shear} -quartile revealed only small or even no correlation between $u_{0.1 \text{ m}}$ and $u_{17 \text{ m}}$. Therefore, Night-Class ENE 2 showed vertical decoupling for small φ_{shear} , whereas Night-Class ENE 1 had predominantly cases of vertical coupling with low φ_{shear} explaining the moderate τ_R of 0.30. However, for small φ_{shear} cold-air drainage might have been possible for Night-Class ENE 2 as no correlation of wind velocities was found. But this was not the case, because Night-Class ENE 2 had adverse conditions for cold-air formation, whereas Night-Class ENE 1 with perfect conditions showed mainly vertical coupling in this range of φ_{shear} . The vertical coupling with high and low φ_{shear} should be confirmed by a high correlation between $u_{0.1 \text{ m}}$, $u_{17 \text{ m}}$ and $u_{0.1 \text{ m}}^*$.

5.2.2 Correlation between wind velocities and momentum exchange

A measure of the momentum exchange and therefore turbulent entrainment is the friction velocity $u_{0.1 \text{ m}}^*$. The $u_{0.1 \text{ m}}-u_{17 \text{ m}}$ -plot and $u_{0.1 \text{ m}}-u_{0.1 \text{ m}}^*$ showed for Night-Class W, that no association between all three parameters existed (Fig. 4.5). Even for high $u_{17 \text{ m}}$ and $u_{0.1 \text{ m}}^*$ of Night-Class W, $u_{0.1 \text{ m}}$ kept $< 0.4 \text{ ms}^{-1}$. Further, no relation between all four parameters $u_{0.1 \text{ m}}$, $u_{17 \text{ m}}$, φ_{shear} and $u_{0.1 \text{ m}}^*$ were found. As a consequence, vertical decoupling was verified for Night-Class W and the ambient momentum exchange kept low.

In contrast, a high correlation between all three parameters was observed for Night-Class ENE 1-3, even though the range of $u_{0.1 \text{ m}}$ and $u_{17 \text{ m}}$ were much bigger for Night-Class ENE 3. Nevertheless, the relation between $u_{0.1 \text{ m}}$, $u_{17 \text{ m}}$ and $u_{0.1 \text{ m}}^*$ for Night-Class ENE 1-3 were mainly three: a linear dependency between all three parameters, a small amount of $u_{0.1 \text{ m}} < 0.4 \text{ ms}^{-1}$ in combination with high $u_{17 \text{ m}}$ and $u_{0.1 \text{ m}}^*$, and a linear dependency between $u_{0.1 \text{ m}}$ and $u_{17 \text{ m}}$ encountered with $u_{0.1 \text{ m}}^* < 0.1 \text{ ms}^{-1}$.

First, the linear dependency revealed the vertical coupling of all three night-classes. Higher $u_{0.1 \text{ m}}$ were induced by higher $u_{17 \text{ m}}$, which enhanced the momentum exchange and therefore $u_{0.1 \text{ m}}^*$. This is also likely related to elimination of cold-air drainage and pooling (e.g. Gustavsson et al. 1998, Mahrt et al. 2001, Sun et al. 2007 and Bodine et al. 2009). Further, the high correlation of $u_{0.1 \text{ m}}$ and $u_{17 \text{ m}}$ was also related to high φ_{shear} (i.e. $> 110^\circ$). This leads to the interpretation of strong winds in 17 m inducing vertical wind velocity and direction shear, enhancing $u_{0.1 \text{ m}}^*$ and consequently forcing a recirculation near the ground.

Second, some $u_{0.1 \text{ m}} < 0.4 \text{ ms}^{-1}$ were encountered with high $u_{17 \text{ m}}$ and $u_{0.1 \text{ m}}^*$. Especially this case was related to $\varphi_{shear} < 110^\circ$ and Night-Class ENE 1 and 2. Further, the wind velocities were vertically decoupled, as the correlation between $u_{0.1 \text{ m}}$ and $u_{17 \text{ m}}$ was small or not significant. Accordingly, this was probably a low level jet inducing high momentum exchange, but no vertical coupling occurred. Therefore, the near bottom flow was either the

maintaining recirculation or the hypothesized cold-air drainage. However, Night-Class ENE 1 and Night-Class ENE 2 showed this relation and Night-Class ENE 2 had adverse conditions for cold-air formation. Consequently, the near bottom flow was probably the maintaining recirculation.

Third, the relation of $u_{0.1\ m}^* < 0.1\ \text{ms}^{-1}$ in combination with a high correlation between $u_{0.1\ m}$ and $u_{17\ m}$. In analysis, no relation to φ_{shear} existed and for Night-Class ENE 3 this case was only found for three outliers. An interpretation is, that the upside-down installation was mounted too low for adequate measurements of $u_{0.1\ m}^*$. The measurement length of the ultrasonic anemometer was 12 cm, but the installation height only 10 cm. Accordingly, measurements were biased due to the installation and therefore lower $u_{0.1\ m}^*$ were measured. If the ultrasonic anemometer was mounted higher, $u_{0.1\ m}$ and $u_{0.1\ m}^*$ probably would be correlated. This should be considered for further studies of near surface measurements.

Hence, Night-Class W had an independent flow near the ground perpendicular to the slope. In contrast, Night-Class ENE 1-3 revealed a near bottom recirculation of strong winds in 17 m ($> 1\ \text{ms}^{-1}$) aligned with the slope, whereas Night-Class ENE 1 and 2 also showed some incidences of a low level jet without vertical coupling. Therefore, the hypothesis was rejected, that cold-air drainage can be predicted by local topography. No cold-air drainage could be found for Night-Class ENE 1, whereas a near bottom flow perpendicular to the slope was found for Night-Class W conflicting the prediction by topography. Further, the inductive analysis was not sufficient, as Night-Class ENE 1-3 revealed the same relations between momentum exchange, wind velocities and directions.

5.2.3 Prevailing wind directions in 17 m

Only two night-classes with $\varphi_{0.1\ m}\ W$ were found with $\varphi_{17\ m}$ throughout the entire range (Fig. B.7). Nevertheless, most data points were found for $\varphi_{17\ m}$ from 130° to 180° (i.e. SSE and S) and $u_{17\ m}$ was mainly $< 2.0\ \text{ms}^{-1}$. Accordingly, no turbulent entrainment should be expected (Soler et al., 2002). Further, Zängl (2009) showed through a numerical model in a alpine valley, that the lowest downvalley flow during night were found for high wind direction shear, if the valley is not sheltered from ambient winds. However, the results for Night-Class W revealed also high φ_{shear} , but no vertical coupling occurred. Further, our study site was much smaller and located at the southeast edge of the city, which itself lies in a shallow valley. Therefore, the study site might be sensitive to ambient winds, but the local slope was sheltered by dense and high vegetation in the South of the study site (Fig. B.15) and the ambient wind were low. Hence, all night-classes with $\varphi_{0.1\ m}\ W$ had a tendency to prevailing wind directions from SSE to S without vertical coupling.

In contrast, six different night-classes with $\varphi_{0.1\ m}\ ENE$ were found and most $\varphi_{17\ m}$ ranged from 220° to 270° , i.e. WSW and W (Fig. 4.6). Further, some smaller patches were observed with less amount of data for $\varphi_{17\ m}$ mainly N and for $\varphi_{17\ m}$ SSE. Besides, $u_{17\ m}$ was mainly $> 1\ \text{ms}^{-1}$ and maximum values of $8.3\ \text{ms}^{-1}$. Therefore, all night-classes with $\varphi_{0.1\ m}\ ENE$ showed prevailing wind directions from WSW to W and high $u_{17\ m}$. This is concordant with the high amount of $\varphi_{shear} > 110^\circ$ of Night-Class ENE 1-3. Further, the prevailing wind direction was not related to I_{net} or the range of $u_{0.1\ m}$ of the different night-classes.

This again verified, that the classification of all night-classes was not sufficient. Moreover, the values of $u_{17\ m}$ were higher for higher values of $u_{0.1\ m}$. In the context of analysis of Night-Class ENE 1-3, this means, that probably for all night-classes with $\varphi_{0.1\ m}$ ENE the wind velocities showed vertical coupling due to the high ambient winds from WSW and W. Therefore, a near bottom recirculation of the ambient winds in 17 m developed, if $\varphi_{17\ m}$ was WSW or W. Other values of $\varphi_{17\ m}$ were probably related to the low level jets with no vertical coupling.

5.3 Spatial temperature distribution

5.3.1 Horizontal and vertical perturbation of temperature

The horizontal and vertical perturbations of temperature above the Lake were the same in all night-classes. In contrast, the perturbations above the other domains was different between the night-classes. The discussion was sectioned into two parts. First, the domains Open Stand, Upper and Lower Meadow are discussed for each night-class. Afterwards, the perturbation above the Lake and the reason, why the perturbation was mainly the same for all night-classes, is revealed.

Night-Class W showed the highest range of $\mu_{\theta_{horiz}^*}$ and $\mu_{\theta_{verti}^*}$ (Fig. 4.7 a and 4.8 a). The Open Stand and the first half of the Upper Meadow had positive $\mu_{\theta_{horiz}^*}$, whereas the second half of the Upper Meadow and the Lower Meadow had only negative $\mu_{\theta_{horiz}^*}$. Therefore, the top of slope was warmer than the bottom. Similar spatial temperature distributions were found by Foken et al. (1999) on the same slope. Temperatures were measured with a glass minimum thermometer in 5 cm at four locations every 15 min. The same horizontal temperature differences were revealed, but the interpretation was, that cold-air drainage down the slope protected the upper two locations from cooling, whereas the lowest location near the Lake gained further cooling by this cold-air drainage. However, this contradicted the measured $\varphi_{0.1\ m}$ of West for our night-class.

Further, at the end of the Upper Meadow and above the Lower Meadow the $\mu_{\theta_{horiz}^*}$ maintained quite low even up to a height of 20 cm. This revealed a cold-air layer, which highest at the end of the Lower Meadow and not existent for the first half of the Upper Meadow. Besides, $\mu_{\theta_{horiz}^*}$ got less intense with increasing height, but the differences between the domains was still obvious. Besides, $\mu_{\theta_{verti}^*}$ was < -1.0 K for at least the lowest 20 cm of all domains, revealing a cold-air layer near the ground. But the lowest $\mu_{\theta_{verti}^*}$ were found from distance 65 m to 140 m in 5 cm height. The vertical temperature gradient was especially high in this region. In contrast, from distance 30 m to 70 m the vertical temperature gradients were noticeably lower. Accordingly, a cold-air layer existed up to a height of 20 cm all along the slope, but the gradients on top of the slope were smaller than at the bottom. Therefore, the combination of $\mu_{\theta_{horiz}^*}$ and $\mu_{\theta_{verti}^*}$ showed, that the upper half of the slope was warmer and had only small temperature gradients, whereas the lower half was much colder and had higher temperature gradients.

The interpretation of Night-Class W is therefore a cold-air pool, filling the area uphill. In

addition, Bodine et al. (2009) showed through Richardson numbers, that cold-air pool formation occurred under strongly stable conditions, for which vertical turbulent mixing near the ground were suppressed and the cold-air pool revealed only small movements. This is concordant for Night-Class W with the extremely low $\mu_{\theta_{verti}}^*$ and temperature gradients at the end of the slope, which revealed the static local stable stratification of the cold-air pool, and with $u_{0.1 m} < 0.4 \text{ ms}^{-1}$, what was measured at distance 70 m. Moreover, the smallest $u_{0.1 m}^*$ was found for this night-class. Vosper and Brown (2008) revealed wind sheltering due to topography and vegetation as an important factor. Our field site was locally wind sheltered especially from south due to a dense vegetation (Fig. B.15), explaining the low $u_{0.1 m}^*$. Accordingly, perfect conditions for cold-air pool formation for Night-Class W with a prevailing wind direction in 17 m from S and SSE. However, this cold-air pool could not originate from the small slope, which was too small for this high amount of cold air. Therefore, the cold-air pool originated from a higher local scale like the Botanical Garden itself and surrounding areas. Nevertheless, an thermal influence of even higher scale flows, e.g. originating from the valley of Bayreuth and surrounding areas, can not be excluded. The wind velocities and directions were vertically decoupled for Night-Class W, but this valley-scale flow or even cold-air drainage from S and SSE might have contributed cold-air, which gained further cooling above the ground and intensified the local cold-air pool above the slope. This would explain the huge difference of $\mu_{\theta_{verti}}^*$ between 5 cm and -2 cm.

Besides, the Open Stand revealed the described outlier from distance 10 m to 30 m with extremely low $\mu_{\theta_{horiz}}^*$ and $\mu_{\theta_{verti}}^*$. In this region, the glass fiber had contact with the ground and therefore gained further cooling. The evaluated temperature gradients had therefore an artifact and were excluded from interpretation.

Night-Class ENE 1-3 were different from Night-Class W and again a transition from Night-Class 1 to Night-Class 3 could be observed for both parameter (Fig. 4.7 b-d and 4.8 b-d). The transition from Night-Class ENE 1 to Night-Class ENE 3 was revealed by the further vanishing of temperature perturbations. Only very small horizontal and vertical temperature differences could be observed. Besides, $\mu_{\theta_{horiz}}^*$ was low and vertically as well as horizontally almost the same. Therefore, the air above the slope was almost isotherm. Only for Night-Class ENE 1 a patch with higher $\mu_{\theta_{horiz}}^*$ were found in the second half of the Open Stand for all heights. This patch was much smaller for the other two night-classes, and for Night-Class ENE 3 the patch only existed for heights from 20 cm to 100 cm. Besides, another small patch in the first half of the Open Stand with lower $\mu_{\theta_{horiz}}^*$ up to a height of 20 cm could be found for Night-Class ENE 1, but became less obvious or even disappeared for Night-Class ENE 2 and Night-Class ENE 3. The vertical perturbation $\mu_{\theta_{verti}}^*$ had similar results. Only small $\mu_{\theta_{verti}}^*$ were found and the domains were almost the same. Besides, Night-Class ENE 1 and Night-Class ENE 2 revealed a thin layer with small $\mu_{\theta_{verti}}^*$ above the Upper and the Lower Meadow in the lowest 10 cm. The transition with vanishing perturbations is concordant with the vertical coupling of these night-classes. The wind velocities and $u_{0.1 m}^*$ were mainly coupled (Fig. 4.5). An increase of $u_{0.1 m}^*$ is related to an enhanced momentum exchange and therefore more turbulence was induced (e.g. Barr and Orgill 1989, Geiss and Mahrt 2015). Therefore, temperature differences got less due to the vertical mixing of air.

Accordingly, no temperature perturbations existed for Night-Class ENE 3, as this night-class revealed the highest $u_{0.1\ m}^*$. In contrast, $u_{0.1\ m}^*$ was lower for Night-Class ENE 1 and Night-Class ENE 2. Consequently, for these two night-classes more temperature perturbations were observed. The difference in $\mu_{\theta_{horiz}^*}$ - and $\mu_{\theta_{verti}^*}$ -values between both night-classes was caused by the different I_{net} , which was much bigger for Night-Class ENE 1. Clouds are one possible reason for the small I_{net} of Night-Class ENE 2, which almost vanish temperature gradients near the ground (Geiger et al., 1995). Accordingly, stronger mixing was needed for Night-Class ENE 1 to vanish an evolving temperature gradient induced by radiative cooling. However, Night-Class ENE 2 also revealed a thin layer with lower temperatures. But this thin layer was probably just an artifact of other night-classes, because Night-Class ENE 2 was always a short period in between other night-classes (Fig. 3.2).

At least for Night-Class ENE 1 and 3 the conditions for cold-air drainage and pooling were given. Nevertheless, all three night-classes were superimposed by moderate to strong winds in 17 m enhancing momentum exchange and therefore vanishing temperature gradients. The moderate to strong winds were probably higher scale flows from WSW or W, e.g. valley-scale or even a regional scale, as these processes had enough synoptic forcing to cause the already discussed recirculation near the ground.

Besides, a small patch was found up to 20 cm height in the first half of the Open Stand for Night-Class ENE 1 and 2 with lower vertical and horizontal temperature perturbations. This is the same outlier as already discussed for Night-Class W. The vertical mixing of Night-Class ENE 3 was effective enough to vanish this outlier.

The values of $\mu_{\theta_{horiz}^*}$ and $\mu_{\theta_{verti}^*}$ above the Lake differed between the night-classes, but the results were the same. The highest values of $\mu_{\theta_{horiz}^*}$ were found above the lake and decreased with height. Night-Class W had higher $\mu_{\theta_{horiz}^*}$ values than the other three night-classes. Besides, $\mu_{\theta_{verti}^*}$ showed a temperature inversion with $\mu_{\theta_{verti}^*}$ (0-0.5 K) in the lowest 20 cm and negative $\mu_{\theta_{verti}^*}$ (-0.5-0 K) on top. Here, the values of $\mu_{\theta_{verti}^*}$ were in the same range for all night-classes. Therefore, the warmest region was directly above the lake up to 20 cm for all night-classes. The fact, that Night-Class W had higher values of $\mu_{\theta_{horiz}^*}$, was probably based on the temperature difference between the domains because of the cold-air pool, which was vanished for Night-Class ENE 1-3. Therefore, the range of $\mu_{\theta_{horiz}^*}$ above the Lake was much higher for Night-Class W than for Night-Class ENE 1-3. Further, Night-Class W and Night-Class ENE 1-3 revealed the same values of $\mu_{\theta_{verti}^*}$ above the Lake. Accordingly, all night-classes can be compared. The small range of $\mu_{\theta_{verti}^*}$ showed, that the temperature differences above the lake were rather small. Further, the warmest region was found above the lake, because the horizontal highest $\mu_{\theta_{horiz}^*}$ were found in this region as well. Accordingly, cold air reaching the Lake was heated through conduction and convection. Therefore, no cold-air pooling above the lake was possible, which rejected the third hypothesis. The lake was big enough to sufficiently heat the cold-air reaching the water surface.

Besides, the influence of the lake on the domain Lower Meadow was revealed for Night-Class ENE 1-3. The same values of $\mu_{\theta_{horiz}^*}$ could be found above the Lake and above the Lower Meadow. This warm patch above the Lake reached further into the Lower Meadow in 100 cm than in 5 cm. Even for Night-Class W some influence of the Lake was present as

the border between the domains was not clearly. These results showed the influence of lakes to the surrounding areas, which can even change the ambient meteorology (Minder et al., 2015). Although the lake of our study site was small compared to other studies, influences of the lake on ambient areas were confirmed. The range of this influence was rather small for Night-Class W (≈ 7 m inland), because the convection above the Lake was not strong enough to heat the cold-air pool at the bottom of the slope more efficiently. In contrast, the range of influence was high for Night-Class ENE 1-3 and reached up to 22 m inland in 100 cm. In this case, high $u_{17\text{ m}}$ induced vertical mixing through wind direction shear in combination with the prevailing wind direction in 17 m from W and WSW. Therefore, the wind velocity and direction shear forced and mixed the warmer air of the Lake above the Lower Meadow. Accordingly, the shear was highest in 100 cm and decreased to the bottom.

5.3.2 Determination of cold-air pools

The CPI mainly differed between Night-Class W and the other night-classes. Night-class W revealed a CPI of 1.2 K and a θ_{top}^* of 0.4 K. Both parameters were zero for the other three night-classes. Based on the definition of Mahrt and Heald (2015), Night-Class W would be a mature cold-air pool, while the flow of the other night-classes would be characterized as a stratified and terrain following flow (Fig. 3.4).

This is concordant with the preliminary findings of Night-Class W. This night-class had calm conditions and $u_{0.1\text{ m}}$ was $< 0.4\text{ ms}^{-1}$. Moreover, this night-class revealed high horizontal and vertical temperature perturbations and especially low values near the ground at the end of the slope. As already discussed above, Night-Class W was probably a cold-air pool as the conditions for the formation were given (Bodine et al. 2009 and Vosper and Brown 2008). This was supported by the high CPI combined with a high θ_{top}^* . For the presumption of higher-scale flows coupled thermally with the cold-air pool, the multiresolution decomposition had to be considered.

In contrast, Night-Class ENE 1-3 had only small horizontal and vertical temperature perturbations caused by the induced mixing of the vertical wind direction and velocity shear. Therefore, this night-classes showed not a stratified, terrain following flow, which would have been revealed by the vertical perturbation. Further, the ambient wind in 17 m was too high (Bodine et al., 2009) and vertically coupled. Accordingly, for this night-classes the already discussed near bottom recirculation of a spatial higher scale flow in 17 m was observed.

5.3.3 Terrain classification for frost risk

The terrain-classification of Night-Class ENE 1-3 was computed, but all showed only $P_{\text{frost risk}} < 20\%$, as cold-air drainage and pooling was not possible for these night-classes. The terrain-classification of Night-Class W revealed, that the highest frost risk existed above the Upper and Lower Meadow (Fig. 4.9). The study of Foken et al. (1999) classified the same locations as exposed to frost. Even in 20 cm the $P_{\text{frost risk}}$ was $>50\%$, whereas in -2 cm and above the lake only small frost risk was found. One possible reason is, that the energy loss of

the ground by radiative cooling is compensated by cooling the air in direct contact with the ground. Accordingly, the temperatures in the ground do not decrease, whereas the air above the ground gains cooling. In contrast, the air above the lake was heated by conduction and convection, which also had influences inland. Therefore, even the air near the lake gained some heating and alleviated the risk for frost. Besides, the part of the Open Stand with more dense vegetation (distance 30 m to 40 m) revealed lower frost risk than the other domains of the slope. One reason for that was, that the dense vegetation emitted longwave radiation in all directions. Accordingly, about half of the emitted longwave radiation was directed to the ground and therefore alleviated radiative cooling. Hence, dense vegetation was able to alleviate frost risk, but low frost risk can only be provided near the lake and below the ground.

5.4 Case studies

5.4.1 Physical description

Case Study 1 (Night-Class W) showed a small range of both wind velocities and the highest temperature range (Fig. 4.10). The high temperature range was probably related to the high I_{net} , causing high radiative cooling of the air near the ground. Further, neither $u_{0.1}$ and $u_{17\ m}$ were correlated nor $\varphi_{0.1\ m}$ and $\varphi_{17\ m}$ were coupled and the median of $u^*_{0.1\ m}$ was the smallest. The same results were shown by the correlation of these parameters for Night-Class W. Besides, the lowest temperatures were found at the lower end of the Upper Meadow and above the Lower Meadow, and the temperatures decreased with increasing distance, what is concordant with the horizontal perturbation above the slope of Night-Class W. The highest temperatures were found above the Lake. Further, the temperatures from distance 135 m to 147 m above the domain Lower Meadow, i.e. in approach to the Lake, were higher than the prevailing temperatures of this domain. This is related to the already stated influence of the lake. Moreover, this influence was constantly obvious during night. The temperature difference between the Lake and the Lower Meadow was up to 3.0 K. Besides, $\varphi_{0.1\ m}$ was constantly W, whereas $\varphi_{17\ m}$ was varying until 09.30 PM and remained constantly SSE to ESE. This had no influence on $\varphi_{0.1\ m}$, but the temperature difference between bottom and top of slope became slightly more intense. The interpretation is, that the valley-scale flow became constant at 09.30 PM and therefore it is possible, that a valley-scale cold-air drainage form SSE started at that time, contributing cold air above the slope, which could gain further cooling. This would explain the increasing temperature difference. No influence on $\varphi_{0.1\ m}$ could be revealed even after 09.30 PM. Hence, the flow near the bottom was only thermally coupled with the valley-scale flow.

The temperatures of Case Study 2 (Night-Class ENE 1) were isotherm above the slope, but warmer above the Lake (Fig. 4.11). The wind velocities correlated well and $\varphi_{17\ m}$ was constantly between W and WSW. Simultaneously, the temperatures above the slope were isotherm, because of the near bottom recirculation of the strong flow in 17 m inducing high momentum exchange and therefore vertical mixing. The flow in 17 m was slightly higher than

2 ms^{-1} . Besides, the processes at 01.30 AM and 02.40 AM were remarkably. At 01.30 AM $u_{17 \text{ m}}$ and $u_{0.1 \text{ m}}$ decreased and remained low. Simultaneously, the temperatures lowered. At 02.40 AM $\varphi_{0.1 \text{ m}}$ became more variant, whereas $\varphi_{17 \text{ m}}$ remained constant. Accordingly, before 01.30 AM the wind velocities were too high ($u_{17 \text{ m}} > 2 \text{ ms}^{-1}$) and therefore temperatures did not change. Another study with investigations of cold-air drainage in a shallow gully showed similar results (Soler et al., 2002). In this study, the cold-air drainage was disturbed or eliminated by turbulence entrainment for wind velocities $\geq 2 \text{ ms}^{-1}$ in 7.4 m. Accordingly, as $u_{17 \text{ m}}$ decreased below 2 ms^{-1} , the radiative cooling was strong enough to lower the temperatures. Nevertheless, the recirculation near the ground maintained until 02.40 AM, as $\varphi_{0.1 \text{ m}}$ did not change and the temperature above the slope still were isotherm. But as $u_{17 \text{ m}}$ remained low the recirculation stopped and $\varphi_{0.1 \text{ m}}$ changed. So, maybe a threshold value of 1.5 ms^{-1} for $u_{17 \text{ m}}$ is needed to initiate the near bottom circulation for this small local slope. Further, the study site was less sheltered by dense vegetation from W (Fig. B.15) and therefore more sensitive to ambient winds from this direction (Vosper and Brown, 2008). After 02.40 AM the temperatures decreased further, probably due to radiative cooling.

Case Study 3 (Night-Class ENE 1-3) was a perfect example for the results of Night-Class ENE 1-3 (Fig. 4.12). The wind directions were mainly constant and directed in the opposite direction of each other. Further, the wind velocities were coupled and the median of $u^*_{0.1 \text{ m}}$ was high. Consequently, the temperature along the slope were isotherm with exception of the warmer lake. A decrease of temperatures was coupled with a decrease in wind velocities. The reason is, that a decrease in the wind velocities is related to a decrease in $u^*_{0.1 \text{ m}}$ due to less vertical wind velocity shear. This explains the relation between wind velocities and temperatures, as the strength of temperature differences (or perturbations) were related to $u^*_{0.1 \text{ m}}$ due to enhanced vertical mixing for increasing $u^*_{0.1 \text{ m}}$. Therefore, the radiative cooling was more effective and the temperature near the ground decreased, as the turbulence entrainment was less for lower $u^*_{0.1 \text{ m}}$. This case study also showed, that Night-Class ENE 1-3 did not differ and were forced by the same process.

Finally, Case Study 4 (Night-Class ENE 1 and Night-Class W) was a mixture of both night-classes (Fig. 4.13). From 08:40 PM until 11:50 PM and around 02:00 AM $\varphi_{0.1 \text{ m}}$ was mainly ENE and $\varphi_{17 \text{ m}}$ was mainly NNW, accordingly φ_{shear} was small. Further, the wind velocities did not correlate and $u_{0.1 \text{ m}}$ was remarkably low. The temperature above the slope were nevertheless isotherm and only the Lake slightly warmer. Whereas for $\varphi_{0.1 \text{ m}}$ W the temperatures lowered and even a temperature difference between the domains could be observed. In this case, $u_{17 \text{ m}}$ was $< 2 \text{ ms}^{-1}$ and $\varphi_{17 \text{ m}}$ was inconsistent. At about 02.00 AM Night-Class W was interrupted by Night-Class ENE, what could also be seen in temperatures, which became higher and more homogeneous above the slope. Moreover, $u_{17 \text{ m}}$ was bigger than the critical value of 1.5 ms^{-1} and therefore broke up the cold-air pool. This shows how easily the cold-air pool of Night-Class W can be interrupted by the strong mixing of Night-Class ENE.

In summary, all case studies were according to the prevailing night-classes. Further, the influence of the lake could be seen in an temperature increase above the Lower Meadow for at least 7 m inland.

5.4.2 MRD: Spatial coherence of temperature development

For all case studies, R_{ij} of the 64 min time scale did not decorrelate for all separation distances (Fig. 4.14). The study of Thomas (2011) revealed the same results with a sensor network of ten station including temperature measurements in 1 m height every 2 min. The maximum separation distance between two stations was 230 m and therefore comparable with our study. The interpretation of this high correlation of the 64-min time scale was, that temperatures follow the diurnal cycle of heating during day and radiative cooling at night. Accordingly, all station were participating this diurnal oscillation, while systematic station-specific decoupling, e.g. through the presence of cold-air pools, were negligible or absent at the study site. Our field study showed the same. Moreover, even during the cold-pool event of Night-Class W no decorrelation could be observed. Besides, both studies showed, that decorrelation of R_{ij} got slower with increasing time scale. Therefore, our study verified a horizontal scale of coherence increasing systematically with time-scale (Thomas, 2011). However, the decorrelation of other time scales was quite different between the case studies.

Case Study 1 (Night-Class W) had the fastest decreasing R_{ij} with increasing separation distance on all time scales (Fig. 4.14 a). Further, even the 16-min time scale decorrelated fast and therefore the temperature courses were spatially highly different for time scales smaller 32 min. Besides, the decorrelation of time scales 8 min, 4 min and 2 min were the same above the Upper and especially above the Lower Meadow. But the decrease of R_{ij} stopped or R_{ij} even increased above the Lake for time scales smaller 32 min. So there was a systematic difference between the Lake and the other two domains. Besides, the decorrelation in the Open Stand was the same as above the Upper and Lower Meadow. For a local process above the slope, the temperature developments would correlate more and the decorrelation of R_{ij} would be much slower with increasing separation distance. Consequently, the processes were influenced by at least a non-local process. Additionally, Night-Class W was the predominating night-class with a high horizontal and vertical temperature perturbation and high CPI, what was also confirmed by the physical description of this case study. Accordingly, the EBG was filled with a non-local cold-air pool. In this case, the temperature decrease was fastest at the bottom of the slope and less intense at the top. Further, the temperature decrease was even less intense above the Lake due to conduction and convection causing the systematic decoupling of this domain. Accordingly, the Lake with a less intense temperature decrease was rather comparable to the Upper Meadow than the Lower Meadow. Therefore, R_{ij} stopped decreasing or even increased. The decrease of R_{ij} within the Open Stand was probably due to the sheltering of the vegetation, which alleviated radiative cooling by emitting about the half of longwave radiation back to the ground and therefore the temperature decrease was less intense as also described by Thomas (2011).

For Case Study 2 (Night-Class ENE 1) the decorrelation of R_{ij} was slower and even almost no decorrelation found for the three highest time scales with exception of the Lake (Fig. 4.14 b). Accordingly, the processes above the Upper and Lower Meadow were spatially more homogeneous, but different above the Lake. At the Lake and in approach to the lake, the decrease of R_{ij} got bigger with increasing separation distance and the minimum R_{ij} of all time scales

was found above the Lake. Therefore, the processes above the lake were different from those above the Upper and Lower Meadow. These results were more obvious for Case Study 3 (Night-Class ENE 1-3) with the slowest decorrelating R_{ij} on all time scales and even the 1-min time scale did not drop below 0.4 (Fig. 4.14 c). Above the Lake and also in approach to the Lake, R_{ij} decreased very fast with increasing separation distance and all time scales revealed their minimum above the Lake. The decorrelation within the domain Open Stand was quite low as well. Accordingly, the decorrelation was quite slow with exception of the Lake with fast decreasing R_{ij} . Therefore, the processes above the Upper and Lower Meadow as well as within the Open Stand were spatially the same. Consequently, the processes seemed to originate from a local scale. But the vertical coupling with high φ_{shear} and an increased momentum exchange showed, that for the Night-Classes ENE 1-3 a near bottom recirculation of a valley-scale flow developed. Further, there was almost no horizontal and vertical temperature perturbation (Fig. 4.7 and 4.8), what was confirmed by the homogeneous temperature distribution of both case studies (Fig. 4.11 and 4.12). Accordingly, due to the enhanced momentum exchange and vertical mixing, the temperature differences above the slope were vanished and the temperature development in these domains spatially simultaneously, explaining the slow decorrelating R_{ij} . In contrast, the temperature development above the Lake was different due to conduction and convection. The temperatures were higher and due to the enhanced momentum exchange in combination with the prevailing wind direction from WSW and W, the warmer air above the lake was also mixed above the Lower Meadow. Therefore, the R_{ij} already decreased in approach to the Lake. The difference between Case Study 2 and 3 was probably, that the wind direction in 0.1 m changed in the second half of Case Study 2 (4.12). Accordingly, for Case Study 3 the processes were coherent during night, while Case Study 2 revealed a change with influence on temperature development. Therefore, the decorrelation of R_{ij} was faster in Case Study 2.

Case Study 4 was a combination of Night-Class W and Night-Class ENE 1 and was comparable to Case Study 2 and 3 (Fig. 4.14 d), even though Night-Class W was predominant, especially for the second half of the night. Nevertheless, the results showed, that the temperature development of a cold-air pool of Night-Class W can easily be vanished due to the enhanced momentum exchange of Night-Class ENE 1-3 (Fig. 4.13). Therefore, Case Study 4 was rather identical to Case Study 2 and 3 than to Case Study 1.

5.4.3 Fog Experiment

Event 1 revealed a flow on top of an existing cold-air layer, which was forced uphill through wind velocity shear (Fig. 4.15). The fast near bottom flow within a thin cold-air layer developed a wind velocity shear with the slower moving layer above. Even though, both were directed downhill, the wind velocity shear slowed the upper layer down and even made this layer turn uphill. The induced shear could also be seen by small shear vortexes in the middle of Fig. 4.15. One possible reason for this is the prevailing Night-Class W. A cold-air pool laid above this region of the transect. Therefore, the lowest temperature were found near the ground. Within this 10 s of the picture series, a flow downhill was observed. Nevertheless, during this time period $u_{0.1 m}$ was $< 0.4 \text{ ms}^{-1}$ and $\varphi_{0.1 m}$ W. This discrepancy of

observed and measured flows is a matter of the time-scale. The 10-s picture series visualized turbulence, whereas the measurements of the evaluated submeso motions were represented on a time scale of 10 min. Accordingly, the seen process probably happened as described, but within an averaging period of 10 min this levels out to a very slow flow from W.

Event 2 was also parted in a thin layer near the ground and an deeper layer above, both directed uphill (Fig. 4.16). The upper layer revealed one big shear vortex and even the layer near the bottom showed small vortexes in the picture series. Besides, the vortexes of the deeper layer vanish and the whole layer slowly flow uphill. One possible reason for the big shear vortex was the bouyancy of the relatively warm fog getting mixed with the prevailing flow in this layer. Further, the shear vortex vanished fast and a flow uphill was visible. Accordingly, the fog lost energy through the bouyancy, was mixed with the relatively cold air, got colder and followed the flow within this layer. Besides, the direction uphill is relative, as a 2-dimensional picture was cut out of a 3-dimensional process. The flow possibly was not directed directly uphill, than rather from W diagonal directed uphill. But this can not be evaluated from the picture. Nevertheless, the mean flow within 10 min came from W. Besides, it can not be stated, if two layer existed or if the fog was parted due to incoherent temperature distribution within the fog.

Mahrt and Thomas (2015) revealed, that the relationship of the turbulence to the stratification is less systematic than expected partly due to enhancement of the turbulence by submeso motions. The shear vortexes and therefore turbulence was visualized by the fog experiment of these two events. The predominating Night-Class W showed highly stable stratification, nevertheless shear vortexes and turbulence could be observed on a 10-s time scale. Further, these processes showed not the 10-min mean flow as would be expected for this very calm, stably stratified nights. But this was not a objective of our study and furthermore could not be resolved temporally with the used DTS-unit.

Finally, Event 3 was the blockage of a cold-air flow and convection above the lake (Fig. 4.17). This showed how effective the conduction and convection above the lake was. Only within 4 m the cold-air flow was stopped and convection forced the fog upwards, resulting in the dextrorotary vortex. This process showed, that cold-air pooling above the lake was not possible, as the cold-air reaching the lake was effectively heated up and no cold-air layer could remain above the lake. Accordingly, the lake was big enough to offset cold-air pooling above the lake, even during Night-Class W with the lowest temperatures.

5.5 Summary

All hypothesis assumptions about cold-air drainage and pooling were rejected. No cold-air drainage above the slope could develop, even if the conditions for cold-air formation were given. All processes near the ground were superimposed by non-local processes. Further, the inductive analysis was not sufficient to identify one night-class with cold-air drainage or separate the four night-classes. Instead, there were probably two different flow modes for Night-Class W (Flow Mode 1) and Night-Class ENE 1-3 (Flow Mode 2). Flow Mode 1 revealed a cold-air pool laying on top of the slope with only small movements. However, the

cold-air pool did not originate from local processes, as the temperature differences were too high to originate from the local slope and the multiresolution composition revealed that the temperature development was influenced by non-local processes. Further, a tendency to a prevailing wind direction from S and SSE in 17 m was found and the processes were vertically decoupled with high φ_{shear} . Accordingly, Flow Mode 1 was a rather stagnant non-local cold-air pool filling the depression of EBG with at least a momentum in 0.1 m from West. This non-local cold-air pool was probably modulated by a valley-scale cold-air drainage from SSE or S and gained further cooling from this flow (Fig. 5.1 a and c). The valley-scale cold-air drainage was probably accelerated by the Sophienberg (blue dashed circle, Fig. 5.1 c) and was modulated in direction by the topography of the valley.

In contrast, Flow Mode 2 showed vertical coupling with enhanced momentum exchange and high wind direction shear. The horizontal and vertical temperature perturbations were rather small for all heights and the multiresolution revealed that temperature development above the slope was spatially the same. Accordingly, the second flow mode was a valley-scale flow with sufficient synoptic forcing to establish a near bottom recirculation (Fig. 5.1 b and c). The momentum exchange was enhanced, because of the wind velocity and direction shear, which vanished the temperature differences along the slope and made the temperatures and also the temperature development more homogeneous above the slope. This explained the small temperature perturbations and the slowly decorrelating R_{ij} of the MRD.

Besides, the measurement setup of this study met the requirements to resolve the dynamics of cold air in the given spatial and temporal resolution. It provided even more information by the temperature measurements of Column B and D with a high spatial resolution (Fig. 2.4) as well as by Station D (Fig. 2.5), which were not assessed. Nevertheless, a smaller temporal resolution of Station EBG would probably be more precise, as the standard deviation of wind directions in 0.1 m were quite high within an averaging period of 10 min. Besides, Station B should be mounted at least in 12 cm to avoid signal loss. Further, another ultrasonic anemometer at Point B in 2 m would have provided even more information about the wind profile, momentum exchange and the vertical coupling.

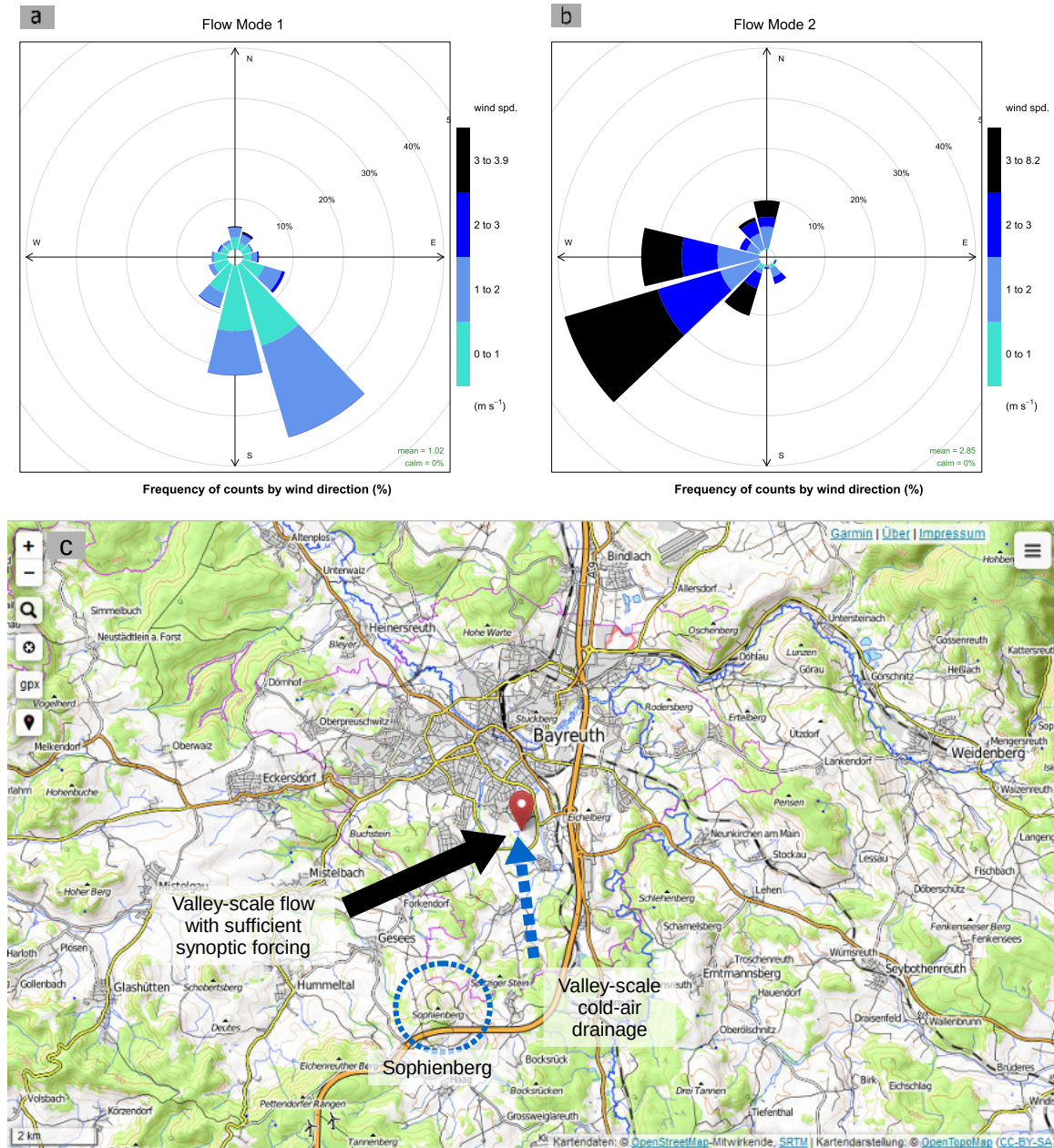


FIGURE 5.1: Summary of wind velocities and directions for both valley-scale flow modes (a and b) and regional topographic overview of Bayreuth (c). a and b: Wind roses with wind velocity classes in 17 m of Flow Mode 1 and 2; c: regional overview with Flow Mode 1 and its source area (dashed blue arrow and circle) and Flow Mode 2 (black arrow)

6. Conclusion

Cold-air drainage and pooling was commonly predicted by the local topography. In contrast, our measurement setup and inductive analysis revealed, that none of the four most abundant classes followed classical textbook knowledge of locally produced cold-air drainage following the topography.

Night-Class W with a flow perpendicular to the local slope revealed the lowest $u_{0.1\ m}$ and $u_{17\ m}$, both parameters were not correlated, no vertical coupling occurred and momentum exchange was very low. Further, a tendency to a prevailing wind direction from SSE to S was found. The horizontal and vertical temperature perturbation were the highest and CPI was high as well. Moreover, the MRD in combination with R_{ij} revealed, that the processes involved in temperature development did not originate from the local slope and were caused by a spatial higher processes. In contrast, Night-Class ENE 1-3 were almost identical. These night-classes showed the highest $u_{0.1\ m}$ and $u_{17\ m}$, both parameters were correlated, especially for high φ_{shear} . Therefore, $u_{0.1\ m}$ and $u_{17\ m}$ were vertically coupled and simultaneously the momentum exchange was high. Especially due to the enhanced momentum exchange, the horizontal and vertical temperature perturbation almost vanished. A prevailing wind direction in 17 m from WSW and W was found with high $u_{17\ m}$. The CPI was zero and the MRD in combination with R_{ij} showed, that the temperature development was spatially the same. Further, cold-air pooling above the Lake was not possible for all night-classes due to conduction and convection, which heated the air above the lake. Moreover, the heated air was also mixed above the Lower Meadow and alleviated radiative cooling.

In summary, all hypotheses had to be rejected. We could not predict cold-air drainage and pooling from the local topography. Further, the inductive analysis was not sufficient to separate different processes during night. Instead, we evaluated two possibly competing non-local flow modes. One for Night-Class W and the second for Night-Class ENE 1-3. Besides, the lake was big enough to eliminate cold-air pooling.

Nevertheless, we interpreted the first flow mode as a close to stationary cold-air pool, originating from a higher scale and filling the depression of the EBG. Here, the deeper non-local cold-air drainage only caused small local movements at the surface, resulting in a small flow from West. This cold-air pool was also modulated by a relatively weak non-local valley-scale cold-air drainage from the Sophienberg. Nevertheless, both layers were largely decoupled. The second flow mode was possibly caused by a recirculation of a stronger valley-scale flow with sufficient synoptic forcing. This also explained the vertical coupling of wind velocities as well as the low temperature perturbations.

In conclusion, the small, gentle slope of our study site was superimposed by higher-scale dynamics. Our findings challenge the common practice to predict cold-air dynamics solely based on micro-topographic analysis.

Acknowledgements

I want to thank all, who have contributed to this thesis. Especially, Prof. Dr. Christoph Thomas for the opportunity to write this thesis, induction in the methods and valuable discussions. PD Dr. Gregor Aas for provision and access of the study site. Armin Sigmund for the good collaboration during deployment and measurement maintenance. Furthermore, Johannes Olesch and Dr. Wolfgang Babel for support during experimental setup.

Bibliography

- Anstey TH, Weiss GM, Watt AW, Wilcox JC, Sprout PN (1959) Relation of soil, temperature and topography to fruit growing in Summerland, British Columbia. *Can J Plant Sci* 39:297–315
- Banta RM, Darby LS, Fast JD, Pinto JO, Whiteman CD, Shaw WJ, Orr BW (2004) Nocturnal low-level jet in a mountain basin complex. Part I: Evolution and effects on local flows. *J Appl Meteorol* 43:1348–1365
- Barr S, Orgill MM (1989) Influence of external meteorology on nocturnal valley drainage winds. *J Appl Meteorol* 28:497–517
- Blennow K, Lindkvist L (2000) Models of low temperature and high irradiance and their application to explaining the risk of seedling mortality. *For Ecol Manage* 135:289–301
- Bodine D, Klein PM, Arms SC, Shapiro A (2009) Variability of surface air temperature over gently sloped terrain. *J Appl Meteorol Climatol* 48:1117–1141
- Burns P, Chemel C (2015) Interactions between downslope flows and a developing cold-air pool. *Boundary-Layer Meteorol* 154:57–80
- Carlsaw DC, Ropkins K (2012) Openair — An R package for air quality data analysis. *Environ Model Softw* 27-28:52–61
- Chung U, Seo HH, Hwang KH, Hwang BS, Choi J, Lee JT, Yun JI (2006) Minimum temperature mapping over complex terrain by estimating cold air accumulation potential. *Agric For Meteorol* 137:15–24
- Clements CB, Whiteman CD, Horel JD (2003) Cold-air-pool structure and evolution in a mountain basin : Peter Sinks , Utah. *J Appl Meteorol* 42:752–768
- Darby LS, Allwine KJ, Banta RM (2006) Nocturnal low-level jet in a mountain basin complex. Part II: Transport and diffusion of tracer under stable conditions. *J Appl Meteorol Climatol* 45:740–753
- Foken T (2008) *Micrometeorology*. Springer, 2 edn.
- Foken T, Beyer S, Bruckmeier C, Nehls T, Radke M, Schmid T, Stadel R (1999) Nachfrosthgefährdung im Ökologisch-Botanischen Garten. Tech. Rep. Nr. 03
- François C, Bosseno R, Vacher JJ, Seguin B (1999) Frost risk mapping derived from satellite and surface data over the Bolivian Altiplano. *Agric For Meteorol* 95:113–137
- Geiger R, Aron RH, Todhunter P (1995) *The climate near the ground*. Wiesbaden: Friedr. Viewg & Sohn Verlagsgesellschaft mbH, Braunschweig, 5 edn.

- Geiss A, Mahrt L (2015) Decomposition of spatial structure of nocturnal flow over gentle terrain. *Boundary-Layer Meteorol* 156:337–347
- Goulden ML, Miller SD, da Rocha HR (2006) Nocturnal cold air drainage and pooling in a tropical forest. *J Geophys Res Atmos* 111:1–14
- Gross G (1987) Some effects of deforestation on nocturnal drainage flow and local climate - A numerical study. *Boundary-Layer Meteorol* 38:315–337
- Gustavsson T, Karlsson M, Bogren J, Lindqvist S (1998) Development of temperature patterns during clear nights. *J Appl Meteorol* 37:559–571
- Haiden T, Whiteman CD (2005) Katabatic flow mechanisms on a low-angle slope. *J Appl Meteorol* 44:113–126
- Howell J, Mahrt L (1997) Multiresolution flux decomposition. *Boundary-Layer Meteorol* 83:117–137
- Keller CA, Huwald H, Vollmer MK, Wenger A, Hill M, Parlange MB, Reimann S (2011) Fiber optic distributed temperature sensing for the determination of the nocturnal atmospheric boundary layer height. *Atmos Meas Tech* 4:1–7
- Kuttler W, Barlag AB, Roßmann F (1996) Study of the thermal structure of a town in a narrow valley. *Atmos Environ* 30:365–378
- Lareau NP, Crosman E, Whiteman CD, Horel JD, Hoch SW, Brown WOJ, Horst TW (2013) The persistent cold-air pool study. *Bull Am Meteorol Soc* 94:51–63
- Liu Z, Bromwich DH (1997) Dynamics of the katabatic wind confluence zone near Siple Coast, West Antarctica. *J Appl Meteorol* 36:97–118
- Mahrt L (2008) Mesoscale wind direction shifts in the stable boundary-layer. *Tellus A* 60:700–705
- Mahrt L, Heald R (2015) Common marginal cold pools. *J Appl Meteorol Climatol* 54:339–351
- Mahrt L, Richardson S, Stauffer D, Seaman N (2014a) Nocturnal wind-directional shear in complex terrain. *Q J R Meteorol Soc* 140:2393–2400
- Mahrt L, Sun J, Oncley SP, Horst TW (2014b) Transient cold air drainage down a shallow valley. *J Atmos Sci* 71:2534–2544
- Mahrt L, Thomas C, Richardson S, Seaman N, Stauffer D, Zeeman M (2013) Non-stationary generation of weak turbulence for very stable and weak-wind conditions. *Boundary-Layer Meteorol* 147:179–199
- Mahrt L, Thomas CK (2015) Surface stress with non-stationary weak winds and stable stratification. *Boundary-Layer Meteorol* :1–19
- Mahrt L, Thomas CK, Prueger JH (2009) Space – time structure of mesoscale motions in the stable boundary layer. *Q J R Meteorol Soc* 135:67–75

- Mahrt L, Vickers D, Nakamura R, Soler MR, Sun J, Burns S, Lenschow DH (2001) Shallow drainage flows. *Boundary-Layer Meteorol* 101:243–260
- McLeod AI (2011) Kendall rank correlation and Mann-Kendall trend test
- Meybeck M, Green P, Vörösmarty C (2001) A new typology for mountains and other relief classes. *Mt Res Dev* 21:34–45
- Minder JR, Letcher TW, Campbell LS, Veals PG, Steenburgh WJ (2015) The evolution of lake-effect convection during landfall and orographic uplift as observed by profiling radars. *Mon Weather Rev* 143:4422–4442
- Müller MD, Masbou M, Bott A (2010) Three-dimensional fog forecasting in complex terrain. *Q J R Meteorol Soc* 136:2189–2202
- Nkemdirim LC (1980) Cold air drainage and temperature fields in an urban environment: A case study of topographical influence on climate. *Atmos Environ* 14:375–381
- Pfister L, Sigmund A, Thomas C (2015) CADEX: Cold air drainage experiment 2015 in the Ecological Botanical Gardens of the University of Bayreuth - Field report. Tech. Rep. 63, University of Bayreuth
- R Core Team (2014) R: A language and environment for statistical computing. R Foundation for Statistical Computing, Vienna, Austria
- Rakovec J, Skok G, Zabkar R, Zagar N (2015) The influence of the depth of a very shallow cool-pool lake on nocturnal cooling. *Agric For Meteorol* 203:17–29
- Schertzer WM, Rouse WR, Blanken PD, Walker AE (2003) Over-lake meteorology and estimated bulk heat exchange of Great Slave Lake in 1998 and 1999. *J Hydrometeorol* 4:649–659
- Selker JS, Thévenaz L, Huwald H, Mallet A, Luxemburg W, van de Giesen N, Stejskal M, Zeman J, Westhoff M, Parlange MB (2006) Distributed fiber-optic temperature sensing for hydrologic systems. *Water Resour Res* 42
- Sigmund A (2015) Untersuchung der bodennahen Temperaturgradienten bei Kaltluftentstehung an einem schwach geneigten Hang mithilfe der Distributed Temperature Sensing - Methode. Bachelor thesis, University of Bayreuth
- Silcox GD, Kelly KE, Crosman ET, Whiteman CD, Allen BL (2012) Wintertime PM_{2.5} concentrations during persistent, multi-day cold-air pools in a mountain valley. *Atmos Environ* 46:17–24
- Soler M, Infante C, Buenestado P, Mahrt L (2002) Observations of nocturnal drainage flow in a shallow gully. *Boundary-Layer Meteorol* 105:253–273
- Sun J, Burns SP, Delany AC, Oncley SP, Turnipseed Aa, Stephens BB, Lenschow DH, LeMone Ma, Monson RK, Anderson DE (2007) CO₂ transport over complex terrain. *Agric For Meteorol* 145:1–21

- Thomas CK (2011) Variability of sub-canopy flow, temperature, and horizontal advection in moderately complex terrain. *Boundary-Layer Meteorol* 139:61–81
- Thomas CK, Kennedy AM, Selker JS, Moretti A, Schroth MH, Smoot AR, Tuffiaro NB, Zeeman MJ (2012) High-resolution fibre-optic temperature sensing: A new tool to study the two-dimensional structure of atmospheric surface-layer flow. *Boundary-Layer Meteorol* 142:177–192
- Thomas CK, Law BE, Irvine J, Martin JG, Pettijohn JC, Davis KJ (2009) Seasonal hydrology explains interannual and seasonal variation in carbon and water exchange in a semiarid mature ponderosa pine forest in central Oregon. *J Geophys Res Biogeosciences* 114:1–22
- Vickers D, Mahrt L (1997) Quality control and flux sampling problems for tower and aircraft data. *J Atmos Ocean Technol* 14:512–526
- Vosper SB, Brown aR (2008) Numerical simulations of sheltering in Valleys: The formation of nighttime cold-air pools. *Boundary-Layer Meteorol* 127:429–448
- Whiteman CD (2000) *Mountain meteorology - Fundamentals and applications*. Oxford University Press
- Zängl G (2009) The impact of weak synoptic forcing on the valley-wind circulation in the Alpine Inn Valley. *Meteorol Atmos Phys* 105:37–53
- Zeeman MJ, Selker JS, Thomas CK (2015) Near-surface motion in the nocturnal, stable boundary layer observed with fibre-optic Distributed Temperature Sensing. *Boundary-Layer Meteorol* 154:189–205
- Zhong S, Bian X, Whiteman CD (2003) Time scale for cold-air pool breakup by turbulent erosion. *Meteorol Zeitschrift* 12:229–233

A. Additional Tables

TABLE A.1: Transfer matrix of CADEX dependent on the LAF of channel 1

Position	Height	LAF [m]	Comment
transect	- 2 cm	273	start at point A
		410	end at point C
	5 cm	458	start at point D
		627	end at point A
	10 cm	183	start of first half at point B
		263	end of first half at point A
		1491	start second half at point D
		1578	end second half at point B
	20 cm	645	start at point A
		815	end at point D
	50 cm	824	start at point D
		995	end at point A
100 cm	1012	start at point A	
	1183	end at point D	
column at the transect	-	1227	start at point B
	-	1446	end at point B
	-	1300	transition from 1 cm to 5 cm winding
column at the lake	-	1613	start at point D
	-	1753	end at point D
	-	1654	transition from 1 cm to 5 cm winding

TABLE A.2: Quantity of categories (N) and percentage of them for the full data set with temporal averaging of ten minutes based on the four factors day and night indicator (DNT), balance between up and down welling longwave radiation (I_{net}), wind direction in 0.1 m height ($\varphi_{0.1m}$) and wind velocity in 0.1 m height ($u_{0.1m}$). Only categories are displayed, which were actually measured.

DNT	$\varphi_{0.1m}$ [-]	I_{net} [W m^{-2}]	$u_{0.1m}$ [m s^{-1}]	N [-]	P [%]
Night	W	10-80	0-1	1198	36.2
Day	ENE	10-80	0-1	394	11.9
Day	ENE	>80	0-1	325	9.8
Night	ENE	10-80	0-1	250	7.6
Day	W	10-80	0-1	225	6.8
Day	SSW	>80	0-1	196	5.9
Night	ENE	<10	0-1	103	3.1
Day	SSW	10-80	0-1	91	2.7
Day	ENE	10-80	1-2	84	2.5
Day	ENE	<10	1-2	78	2.4
Night	ENE	10-80	1-2	74	2.2
Day	ENE	<10	0-1	42	1.3
Night	ENE	<10	1-2	39	1.2
Transition	W	10-80	0-1	38	1.1
Night	W	<10	0-1	34	1
Day	W	>80	0-1	27	0.8
Day	ENE	10-80	2-3	25	0.8
Night	SSW	10-80	0-1	22	0.7
Day	ENE	>80	1-2	21	0.6
Day	ENE	<10	2-3	13	0.4
Day	W	<10	0-1	5	0.2
Night	SSW	<10	0-1	5	0.2
Transition	ENE	10-80	0-1	5	0.2
Transition	ENE	<10	0-1	3	0.1
Transition	ENE	<10	1-2	3	0.1
Transition	ENE	10-80	1-2	3	0.1
Day	SSW	<10	0-1	2	0.1
Night	ENE	<10	2-3	2	0.1
Night	ENE	10-80	2-3	1	0
Transition	W	<10	0-1	1	0
Transition	SSW	10-80	0-1	1	0

TABLE A.3: Output of BmmFlux-software as described in (Thomas et al., 2009) with explanation of all used variables

Nr.	Column label	Unit	Explanation
1	Datetime_start	[1]	Start time of averaging interval, center, formatted datetime string
2	Datetime_end	[1]	End time of averaging interval, center, formatted datetime string

to be continued on next page

Nr.	Column label	Unit	Explanation
10	zenith	[°]	Zenith angle of the sun
12	DayNightIndicator	[1]	Day and night indicator: 0 = night, 0.5 = transition (sunrise/sunset), 1 = day
17	u_mean_unrot	[m s ⁻¹]	Wind component x, sonic, unrotated, mean
18	u_std_unrot	[m s ⁻¹]	Wind component x, sonic, unrotated, standard deviation
19	u_skew_unrot	[(m s ⁻¹) ³]	Wind component x, sonic, unrotated, skewness
20	u_kurt_unrot	[(m s ⁻¹) ⁴]	Wind component x, sonic, unrotated, kurtosis
21	v_mean_unrot	[m s ⁻¹]	Wind component y, sonic, unrotated, mean
22	v_std_unrot	[m s ⁻¹]	Wind component y, sonic, unrotated, standard deviation
23	v_skew_unrot	[(m s ⁻¹) ³]	Wind component y, sonic, unrotated, skewness
24	v_kurt_unrot	[(m s ⁻¹) ⁴]	Wind component y, sonic, unrotated, kurtosis
25	w_mean_unrot	[m s ⁻¹]	Wind component z (vertical), sonic, unrotated, mean
26	w_std_unrot	[m s ⁻¹]	Wind component z (vertical), sonic, unrotated, standard deviation
27	w_skew_unrot	[(m s ⁻¹) ³]	Wind component z (Vertical), sonic, unrotated, skewness
28	w_kurt_unrot	[(m s ⁻¹) ⁴]	Wind component z (Vertical), sonic, unrotated, kurtosis
29	phi	[deg]	Wind direction
32	u_mean_rot	[m s ⁻¹]	Wind component, along-wind, rotated, mean
33	frc_fact_uu	[1]	Spectral frequency correction factor applied to standard deviation
34	u_std_rot	[m s ⁻¹]	Wind component, along-wind, rotated, standard deviation
35	u_skew_rot	[(m s ⁻¹) ³]	Wind component, along-wind, rotated, skewness
36	u_kurt_rot	[(m s ⁻¹) ⁴]	Wind component, along-wind, rotated, kurtosis
37	v_mean_rot	[m s ⁻¹]	Wind component, cross-wind, rotated, mean
39	v_std_rot	[m s ⁻¹]	Wind component, cross-wind, rotated, standard deviation
40	v_skew_rot	[(m s ⁻¹) ³]	Wind component, cross-wind, rotated, skewness

to be continued on next page

Nr.	Column label	Unit	Explanation
41	v_kurt_rot	$[(\text{m s}^{-1})^4]$	Wind component, cross-wind, rotated, kurtosis
42	w_mean_rot	$[\text{m s}^{-1}]$	Wind component, vertical, rotated, mean
44	w_std_rot	$[\text{m s}^{-1}]$	Wind component, vertical, rotated, standard deviation
45	w_skew_rot	$[(\text{m s}^{-1})^3]$	Wind component, vertical, rotated, skewness
46	w_kurt_rot	$[(\text{m s}^{-1})^4]$	Wind component, vertical, rotated, kurtosis
52	co2_mean_analyz1	$[\text{mmol m}^{-3}]$	CO ₂ concentration, mean
54	co2_std_analyz1	$[\text{mmol m}^{-3}]$	CO ₂ concentration, standard deviation
55	co2_skew_analyz1	$[\text{mmol}^3 \text{m}^{-9}]$	CO ₂ concentration, skewness
56	co2_kurt_analyz1	$[\text{mmol}^4 \text{m}^{-12}]$	CO ₂ concentration, kurtosis
57	h2o_mean_analyz1	$[\text{mmol m}^{-3}]$	Water vapor concentration, mean
59	h2o_std_analyz1	$[\text{mmol m}^{-3}]$	Water vapor concentration, standard deviation
60	h2o_skew_analyz1	$[\text{mmol}^3 \text{m}^{-9}]$	Water vapor concentration, skewness
61	h2o_kurt_analyz1	$[\text{mmol}^4 \text{m}^{-12}]$	Water vapor concentration, kurtosis
73	u*	$[\text{m s}^{-1}]$	Friction velocity = $\sqrt{u'w'^2 + v'w'^2}$

TABLE A.4: Quantity of spikes (N) and percentage of full data set (P) in per mill for each day for measurements at the transect in six different heights (Transect), at the column at the lake (Column lake) and at the column at the transect (Column transect). Last row is the summary for the full measurement period.

Date	Transect		Column lake		Column tower	
	N [-]	P [‰]	N [-]	P [‰]	N [-]	P [‰]
13.03.	4	0.0	0	0.0	1	0.0
14.03.	38	0.0	0	0.0	0	0.0
15.03.	204	0.1	6	0.0	27	0.1
16.03.	452	0.2	231	0.4	188	0.5
17.03.	51	0.0	0	0.0	1	0.0
18.03.	16	0.0	0	0.0	0	0.0
19.03.	128	0.1	0	0.0	0	0.0
20.03.	125	0.0	0	0.0	0	0.0
21.03.	126	0.1	1	0.0	1	0.0
22.03.	3	0.0	0	0.0	0	0.0
23.03.	0	0.0	0	0.0	0	0.0
24.03.	13	0.0	0	0.0	0	0.0
25.03.	49	0.0	1	0.0	55	0.1
26.03.	1	0.0	0	0.0	0	0.0
27.03.	28	0.0	0	0.0	0	0.0

to be continued on next page

Date	Transect		Column lake		Column tower	
	N [-]	P [‰]	N [-]	P [‰]	N [-]	P [‰]
28.03.	106	0.0	139	0.2	0	0.0
29.03.	2667	1.0	1191	1.9	929	2.3
30.03.	139	0.1	111	0.2	47	0.1
31.03.	0	0.0	0	0.0	0	0.0
01.04.	0	0.0	0	0.0	0	0.0
02.04.	30	0.0	54	0.1	85	0.2
03.04.	196	0.1	0	0.0	30	0.1
04.04.	11	0.0	0	0.0	0	0.0
05.04.	560	0.2	43	0.1	6	0.0
06.04.	27	0.0	0	0.0	0	0.0
07.04.	26	0.0	0	0.0	0	0.0
08.04.	1	0.0	0	0.0	0	0.0
09.04.	19	0.0	0	0.0	0	0.0
10.04.	38	0.0	0	0.0	0	0.0
11.04.	92	0.0	2	0.0	3	0.0
12.04.	24	0.0	18	0.0	0	0.0
13.04.	20	0.0	0	0.0	0	0.0
14.04.	120	0.0	0	0.0	0	0.0
15.04.	11	0.0	0	0.0	0	0.0
16.04.	9	0.0	0	0.0	0	0.0
17.04.	18	0.0	0	0.0	0	0.0
18.04.	2	0.0	0	0.0	0	0.0
19.04.	4	0.0	0	0.0	0	0.0
20.04.	0	0.0	0	0.0	0	0.0
21.04.	0	0.0	19	0.0	0	0.0
22.04.	521	0.2	14	0.0	8	0.0
23.04.	0	0.0	0	0.0	0	0.0
24.04.	180	0.1	4	0.0	22	0.1
25.04.	112	0.0	23	0.0	0	0.0
26.04.	0	0.0	0	0.0	0	0.0
27.04.	616	0.2	92	0.2	0	0.0
28.04.	116	0.1	24	0.0	5	0.0
Σ	6903	0.1	1973	0.1	1408	0.1

TABLE A.5: Quantity of dropouts (N) and percentage of full data set (P) in per mill for each day for measurements at the transect for the heights 5 cm above ground ($h = 5$ cm) and 10 cm above ground ($h = 10$ cm). Last row is the summary for the full measurement period.

Datum	h = 5 cm		h = 10cm	
	N [-]	P [‰]	N [-]	P [‰]
13.03.	7152	15.7	0	0.0
14.03.	3075	6.4	1502	3.2
15.03.	204	0.4	0	0.0
16.03.	31	0.1	319	0.7
17.03.	11859	24.5	263	0.6
18.03.	4477	9.3	0	0.0
19.03.	5385	11.1	323	0.7
20.03.	13148	27.2	448	1.0
21.03.	47	0.1	0	0.0
22.03.	593	1.2	879	1.9
23.03.	183	0.4	194	0.4
24.03.	93	0.2	203	0.4
25.03.	0	0.0	50	0.1
26.03.	31	0.1	45	0.1
27.03.	313	0.6	29	0.1
28.03.	39	0.1	263	0.6
29.03.	11524	23.8	0	0.0
30.03.	17693	36.6	149	0.3
31.03.	26741	55.3	0	0.0
01.04.	29926	61.9	0	0.0
02.04.	32081	66.3	154	0.3
03.04.	7874	16.3	287	0.6
04.04.	884	1.8	809	1.7
05.04.	11743	24.3	336	0.7
06.04.	1182	2.4	309	0.7
07.04.	2108	4.4	433	0.9
08.04.	1164	2.4	813	1.7
09.04.	1575	3.3	808	1.7
10.04.	576	1.2	629	1.3
11.04.	2439	5.0	0	0.0
12.04.	15096	31.2	154	0.3
13.04.	618	1.3	63	0.1
14.04.	579	1.2	222	0.5
15.04.	587	1.2	100	0.2
16.04.	417	0.9	2	0.0

to be continued on next page

Datum	h = 5 cm		h = 10cm	
	N [-]	P [‰]	N [-]	P [‰]
17.04.	538	1.1	325	0.7
18.04.	1452	3.0	754	1.6
19.04.	1857	3.8	1012	2.2
20.04.	1319	2.7	927	2.0
21.04.	1146	2.4	706	1.5
22.04.	1499	3.1	671	1.4
23.04.	1607	3.3	783	1.7
24.04.	730	1.5	473	1.0
25.04.	321	0.7	0	0.0
26.04.	1177	2.4	462	1.0
27.04.	7984	16.5	47	0.1
28.04.	26627	59.8	326	0.8
Σ	257694	11.4	16272	0.7

B. Additional Figures

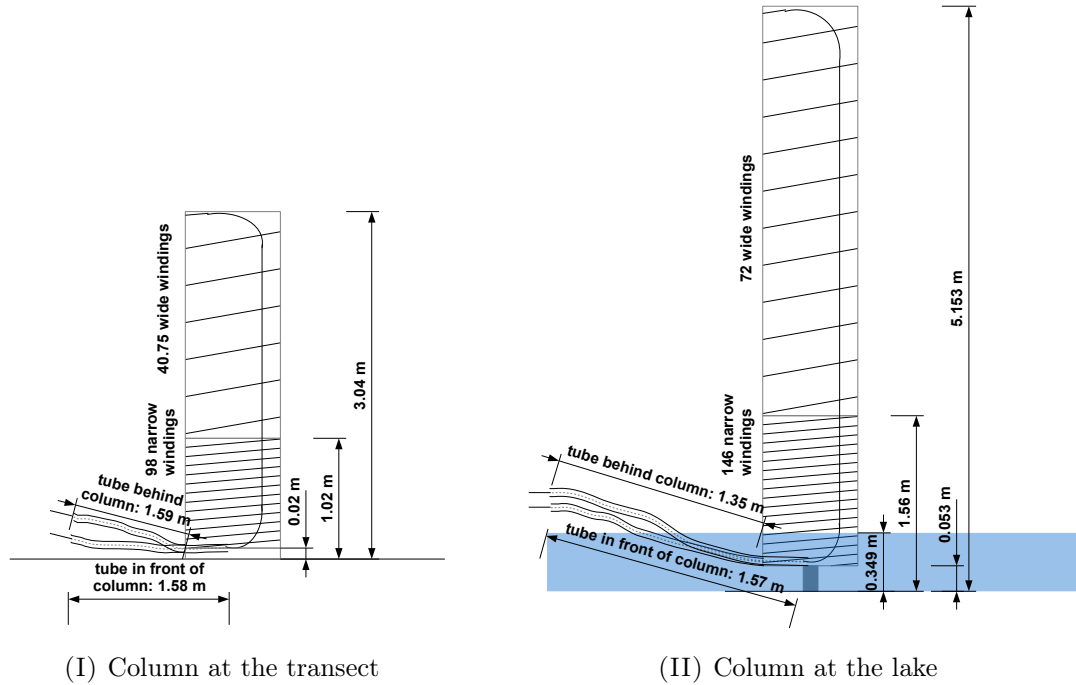


FIGURE B.1: Proportions of the columns. "In front of/behind column" refers to the direction of channel 1.

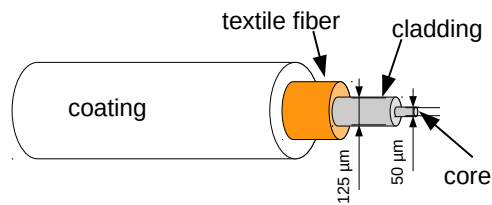


FIGURE B.2: Composition of the glass fiber

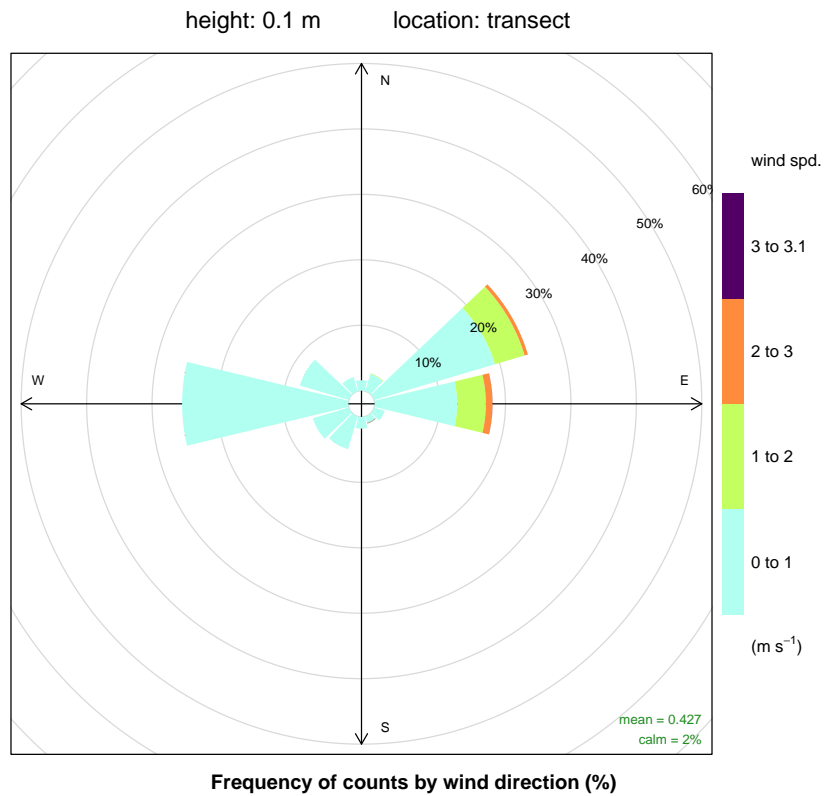


FIGURE B.3: Wind rose of the ultrasonic at the transect in 0.1 m height. Colors dependent on wind velocity.

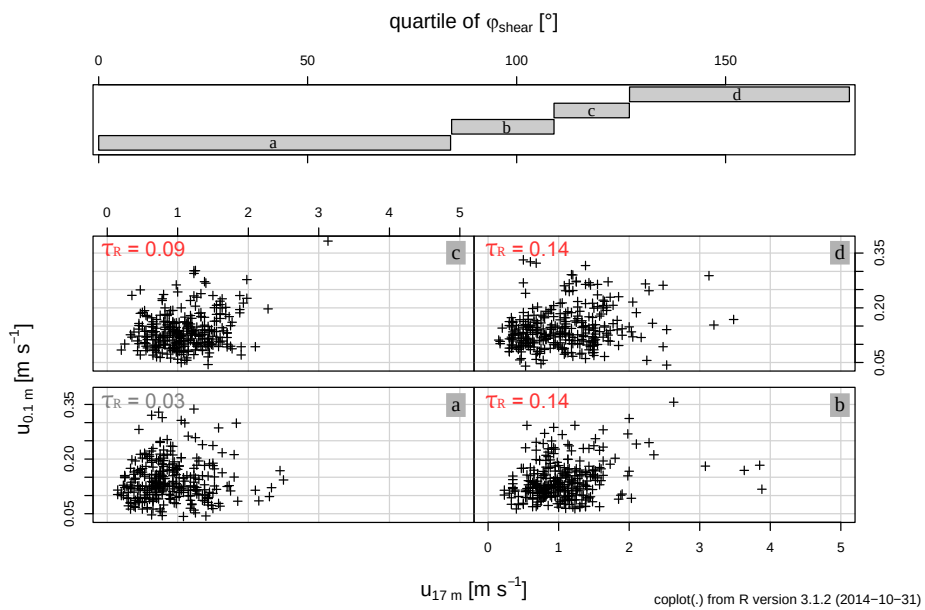


FIGURE B.4: Coplot of Night-Class W dependent on quartile of wind direction shear φ_{shear} . ' τ ' (red): correlation coefficient; ' τ_R ' (gray): no significant association found between the wind velocities.

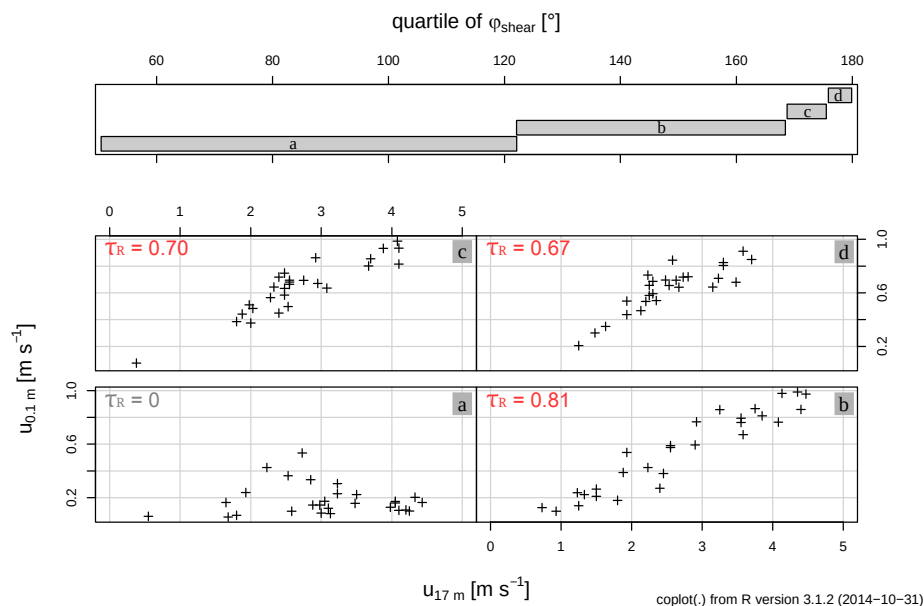


FIGURE B.5: Coplot of Night-Class ENE 2 dependent on quartile of wind direction shear φ_{shear} . τ_R (red): correlation coefficient; τ_R (gray): no significant association found between the wind velocities.

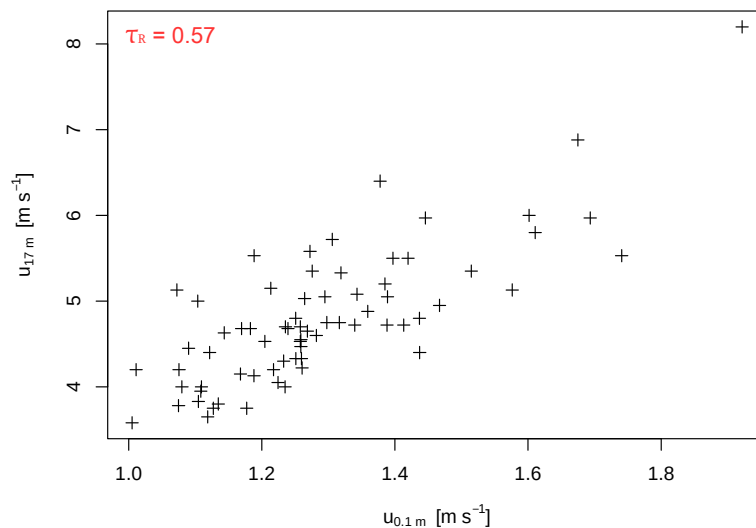


FIGURE B.6: correlation between wind velocities in 17 m and 0.1 m height ($u_{17\text{ m}}$ and $u_{0.1\text{ m}}$) for Night-Class ENE 3. τ_R (red): correlation coefficient

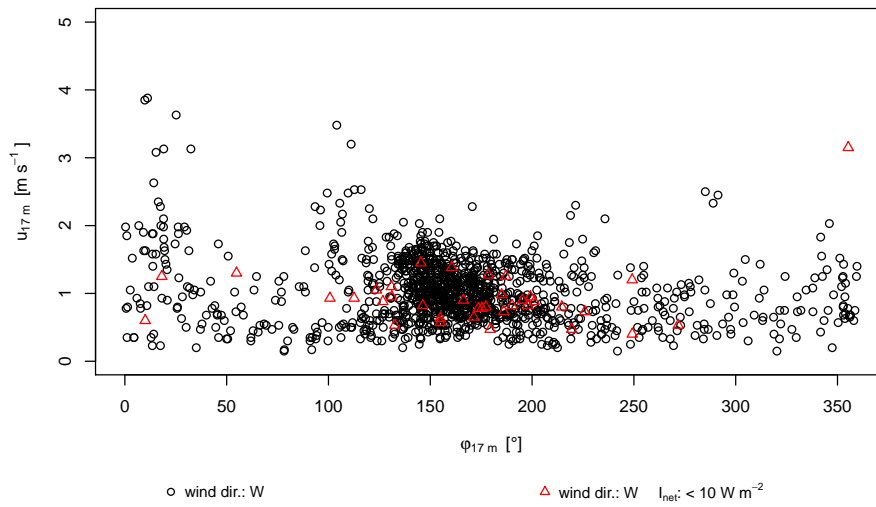


FIGURE B.7: Wind direction and velocity in 17 m height ($\varphi_{17\text{ m}}$ and $u_{17\text{ m}}$) for each Night-Class with wind direction W in 0.1 m height.

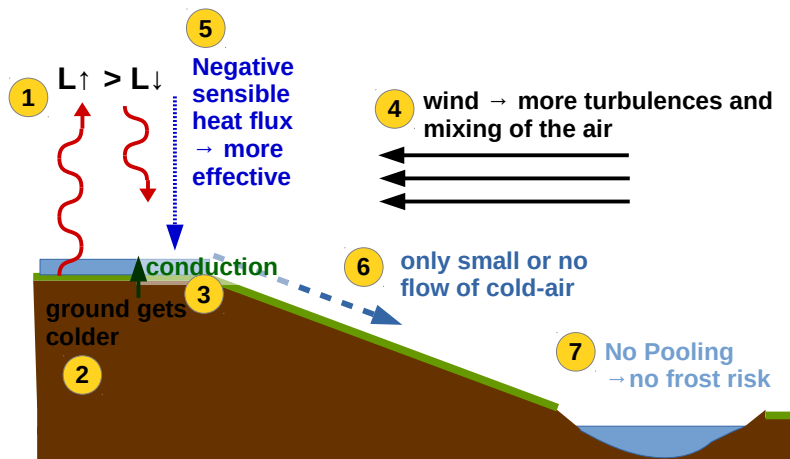


FIGURE B.8: Draft cold-air formation and drainage on the local slope during cloudy windy nights



(I) Inserting the fiber into the plow



(II) Plow inserted into the ground

FIGURE B.9: Self-designed plow for inserting the fiber into the ground



(I) Self-designed block with plastic tube



(II) Self-designed block without plastic tube, close-up view

FIGURE B.10: Self-designed blocks to hold the fiber along the transect in the wanted height above ground and to facilitate strengthening of the fiber. The plastic tube additionally retains the fiber in the wanted position. The three grooves can be used to have three different fibers in one height without touching each other.



(I) self-designed poles with attached blocks and anchoring cables



(II) Earth nail to attach the anchoring cables

FIGURE B.11: Self-designed poles with attached blocks and anchoring cables

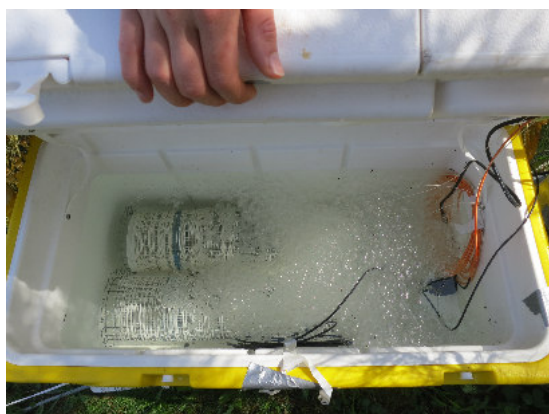


(I) Pulley-holder attached to the small tower at point A of the transect



(II) Pulley-holder of 5 cm and 20 cm height at point A of the transect, close-up view

FIGURE B.12: Self-designed pulley-holder at the small tower at the start of the transect

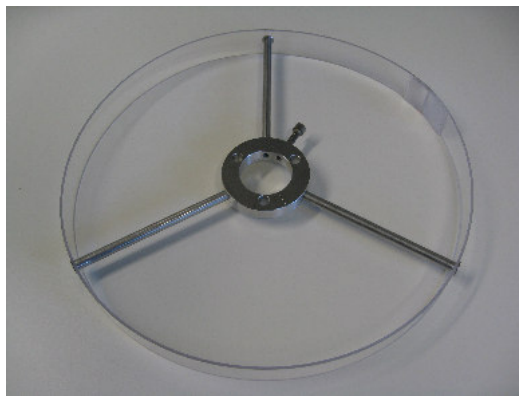


(I) Icebath for 'zero'-calibration

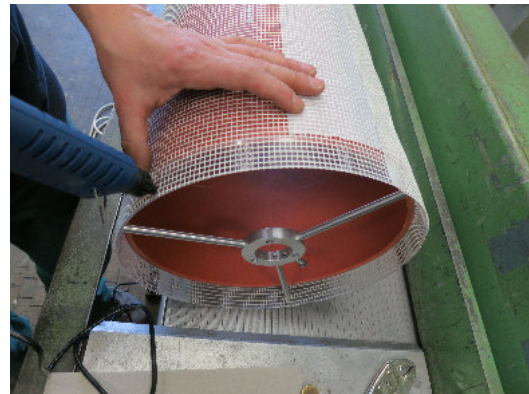


(II) Warmwaterbath with heater on the right side of the bath for 'span'-calibration

FIGURE B.13: Calibration baths at the transect



(I) Transparent ring



(II) Gluing reinforcement fabric



(III) Gluing fiber optic winding



(IV) Melted PVC-coating at a glue dot

FIGURE B.14: Construction of the columns

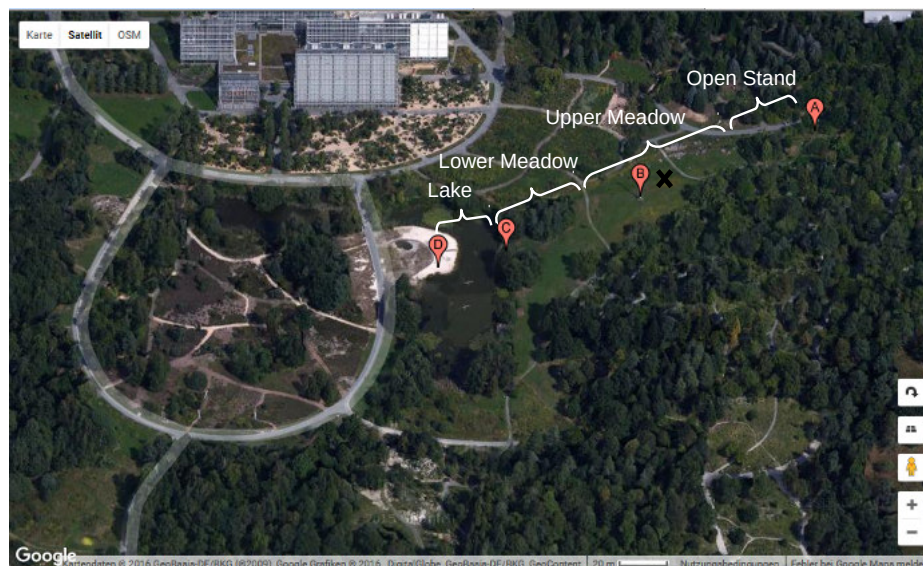


FIGURE B.15: Aerial image of the field site with domains. Point A: Start point of transect; Point B: Meteorological Measurement Station; Point C and D: Borders of the lake in the depression; black cross: Station B (wind measurements in 0.1 m)

C. Digital Medium

The attached CD contains all necessary R-Scripts to compute and depict all results, figures and tables. Moreover, all figures of this Master thesis and picture series of the fog experiment are included. The raw data of all measuring devices are available on the server of Micrometeorology Group of the University of Bayreuth:

```
btgmm6.geo.uni-bayreuth.de/volumes/mmraid/mm_archive/Data_2015...  
.../OeBG/CADEX/
```


Declaration of Authorship

I, Lena PFISTER, declare that this thesis titled, “Novel insights into the dynamics of cold-air drainage and pooling on a gentle slope from fiber-optic distributed temperature sensing” and the work presented in it are my own. I confirm that:

- This work was done wholly or mainly while in candidature for a research degree at this University.
- Where any part of this thesis has previously been submitted for a degree or any other qualification at this University or any other institution, this has been clearly stated.
- Where I have consulted the published work of others, this is always clearly attributed.
- Where I have quoted from the work of others, the source is always given. With the exception of such quotations, this thesis is entirely my own work.

Signed:

Date:
